Development of a single photon detector using wavelength-shifting and light-guiding technology

Dissertation
zur Erlangung des akademischen Grades

doctor rerum naturalium
(Dr. rer. nat.)

im Fach Physik
eingereicht an der
Mathematisch-Naturwissenschaftlichen Fakultät der
Humboldt-Universität zu Berlin

von
Herrn M.Sc. Dustin Hebecker

Präsidentin der Humboldt-Universität zu Berlin
Prof. Dr.-Ing. Dr. Sabine Kunst

Dekan der Mathematisch-Naturwissenschaftlichen Fakultät
Prof. Dr. Elmar Kulke

1. Gutachter:	Prof. Dr. Marek Kowalski
2. Gutachter:	Prof. Dr. Sebastian Böser
3. Gutachterin:	PD Dr. Ira Jung-Richardt

Tag der mündlichen Prüfung: 10.08.2021

Zusammenfassung

Das IceCube Neutrino-Observatorium ist ein am geographischen Südpol im Eis installierter Neutrinodetektor. In IceCube werden Neutrinos mit Tscherenkow-Strahlung von Sekundärteilchen aus Neutrino Interaktionen detektiert. Für den Nachfolgedetektor IceCube-Gen2, werden neue und verbesserte Lichtdetektoren gesucht.

Die vorliegende Arbeit beschreibt die Entwicklung von einem dieser Lichtdetektoren. Dieser basiert auf Wellenlängen schiebenden und Licht leitenden Technologien. Der Detektor mit dem Namen "Wavelength-shifting Optical Module" (WOM) verwendet eine transparente Röhre, mit wellenlängenschiebender Farbe, als passiver Photonendetektor. Das in der Wellenlänge verschobene Licht wird durch Totalreflexion, zu kleinen aktiven Lichtsensoren an beiden Enden geleitet. Die Auswahl dieses Designs reduziert die Kosten und verbessert das Signal-Rausch-Verhältnis wesentlich, möglicherweise können mit dieser Lösung extragalaktische Supernova in zukünftigen Detektoren beobachtet werden.

Als eine Kernkomponente wird die wellenlängenschiebende Röhre ausführlich untersucht. Verschiedene Messaufbauten und Auswertungsmethoden werden entwickelt, um diese im Anschluss zu untersuchen und zu bewerten. Iterative Verbesserungen der Materialien und des Farbauftrageverfahren als auch Messmethoden, resultieren in einer kombinierten Einfang-, Wellenlängenschiebe- und Transporteffizienz von 28.1 ± 5.4 % der Röhre. Diese Ergebnisse stehen im Kontrast zum theoretischen Maximum von 74.5 %. Ein Model zur Beschreibung des Lichtverhaltens in der Röhre wird entwickelt um die Diskrepanz zwischen Theorie und Messung zu untersuchen. Die Kombination zwischen Messung und Model, bestätigt die Aussagekraft des Models und zeigt, dass ein Großteil der Verluste beim Lichttransport zustande kommen.

Darüber hinaus werden die physikalischen Eigenschaften des WOM in die IceCube Simulationsumgebung eingebaut. Für verschiedene IceCube-Gen2 Geometrien, werden mit einem verbesserten optischen Modul aus IceCube (pDOM) und dem WOM Ereignisse zwischen 3 TeV und 1 PeV simuliert. Der Vergleich zwischen beiden Modulen zeigt, dass der WOM das pDOM um einen Faktor 1.05 ± 0.07 in der Anzahl der detektierten Photonen übertrifft. Wo anwendbar, werden Vorschläge und Ausblicke für zukünftige Verbesserungen der Leistungsfähigkeit des WOMs gegeben.

Abstract

The IceCube Neutrino Observatory is an in ice neutrino detector located at the geographic South Pole. In IceCube neutrinos are detected via Cherenkov light produced by secondary particles in neutrino interactions. For the upgraded detector IceCube-Gen2, new and improved light detectors are sought-after.

This work describes the development of one of those light detectors based on a novel combination of wavelength-shifting and light-guiding technology. The detector named the Wavelength-shifting Optical Module (WOM) utilizes a large transparent tube, coated with wavelength-shifting paint as a passive photon detector. The wavelength-shifted light is guided via total internal reflection towards small active light detectors, at each end of the tube. This design reduces costs and improves the signal to noise ratio significantly, thereby potentially enabling extragalactic supernova detections in future detectors.

As a core component, the wavelength-shifting tube is extensively investigated. Different measurement setups and evaluation techniques are developed and investigated. Iterative improvement of materials and coating techniques as well as measurement methods currently result in a combined photon capture, shift and transport efficiency of 28.1 ± 5.4 % for the tube. Those results contrast the theoretical maximum of 74.5 %. A model is developed to describe the light propagation and loss processes in the tube and to understand the discrepancies between theory and measurement. The combination of the measurements with the model, validate the descriptive qualities of the model and show that most of the light is lost during the light propagation in the tube.

Additionally, the physical properties of the WOM are included in the IceCube simulation framework. For various IceCube-Gen2 geometries, events between 3 TeV and 1 PeV are simulated with an improved version of the optical module used in IceCube (pDOM) as well as the WOM. The comparison between both modules showed that the WOM outperforms the pDOM by a factor of 1.05 ± 0.07 in photon detection numbers. Where applicable, suggestions and outlooks are given to enhance the performance of the WOM.

Contents

Preamble

One of my favourite science fiction characters once said "I aspire [...] to be better than I am"[1]. For me, science is a continuous effort to become better than we are as a species. Part of this is fundamental research, that is essential in improving our capabilities and understanding. In a particular case though the result is more of a gamble. You never know where it may lead you. For instance, where this thesis leads is left to the interested reader to find out.

Astroparticle physics, a very young field in physics, promises great potential for the understanding of the universe. Here the smallest[2] and largest[3] known spacial expansions are used to investigate one another. Outer space provides a range of extreme environments that can produce and accelerate many particle species to a fraction of the speed of light. These particles offer a probe of particle physics and cosmology at energy scales far beyond what can be achieved on Earth.

A particle of special interest to this thesis is the neutrino. Neutrinos are neutrally charged particles with very low masses and thus travel with almost the speed of light. Unlike light, they pass nearly unhindered through large amounts of matter. This makes them extremely interesting in the context of multi-messenger physics, an area of astrophysics that uses multiple messengers such as cosmic rays, neutrinos, photons and gravitational waves to learn about their sources and the cosmos in general. To detect neutrinos given their elusive nature, large detection volumes are required, such as the cubic kilometre of instrumented glacial ice used by the IceCube experiment located at the Geographic South Pole.

IceCube operates based on the detection of Cherenkov photons that are produced by secondary particles from neutrino interactions in the ice. The photons travel until absorbed or detected by optical sensors deployed in the ice. After a series of initial successes, such as the first detection of extragalactic neutrinos and some promising neutrino source candidates, a next-generation experiment called IceCube-Gen2 has been proposed. With this new instrument, the detection energy range will be expanded at both ends through different instrumented volumes and sensor densities. Moreover, improved optical sensors are being developed, that will outperform those that are currently deployed in the ice.

One such module, the Wavelength-shifting Optical Module or WOM, focusses on an improved signal-to-noise ratio, higher photon counts and lower costs. These properties would result in better energy resolution, a larger instrumented volume and thus a larger number of neutrino detections, as well as the detection of extragalactic supernova facilitated by the expected low signal-to-noise ratio. To achieve an improved signal-to-noise ratio, the WOM incorporates a passive wavelength-shifting and light-guiding component, which is used to collect the light on a large area and concentrate it on two

[1] Commander Data in Star Trek Nemesis.
[2] Particles
[3] Outer space.

small light sensors. The passive element is made from a transparent tube with adiabatic light guides at each end. The tube is coated with wavelength-shifting paint. While the other module components like a pressure-vessel, electronics and light sensors are proven technologies, the facilitation of wavelength-shifter and light-guiding in this combination is novel and requires the most attention. In a previous master thesis, the wavelength-shifting paint for the WOM has been developed and analysed on a basic level.

The three main tasks presented in this thesis are improved measurements for the optical components of the WOM, modelling the properties of the optical components and the performance comparison with a baseline optical module in an IceCube-Gen2 based full detector simulation. The measurement techniques used to analyse the WOM and specifically the wavelength-shifting and light-guiding components, with respect to the photon detection efficiency, are evaluated and iteratively improved. Leading to a better understanding, improved reproducibility and reduced systematics of those measurements. A model for the optical behaviour of the wavelength-shifting and light-guiding components was derived from fundamental physical laws. Open parameters of the model were determined based on the data obtained with the improved measurements techniques and compared to literature values. Leading to a precise characterisation of the photon detection efficiency based on the photon impact position. The new and more accurate measurements were also used to simulate the expected performance of the WOM in an IceCube-Gen2 environment. The same simulations were also performed for a baseline IceCube-Gen2 configuration without the WOM to obtain a comparison for the performance of the WOM.

To guide the reader into the topic, the first chapter introduces neutrinos with their known properties and various detection techniques. Chapter two introduces the IceCube experiment and and its components. To underline the importance of this thesis, IceCube-Gen2 is described in the third chapter, including the basics on the WOM and its competitors. Following the introduction into the basics, the fourth chapter expands on the details of the WOM and the research that has already been done previously. Chapter five describes the laboratory setup and measurement campaign used to characterize the WOM-performance. In the sixth chapter, the physical behaviour of light in the wavelength-shifting and light-guiding tube is modelled and compared to the results from the fifth chapter to obtain information on the physical properties of the tube. Chapter seven incorporates the results from the measurement campaign to simulate a WOM-based IceCube-Gen2 detector and evaluate its performance in comparison to other modules. This is followed by the conclusions, summarising the results and giving an outlook on possible next steps.

CHAPTER 1

Neutrinos

1.1 Properties

Neutrinos are part of the Standard Model of elementary particle physics as illustrated in fig. 1.1. To the best of our knowledge, they are elementary particles of neutral charge. The neutrino was proposed by Wolfgang Pauli to solve energy, momentum and angular momentum conservation for the beta decay in 1930 [1]. It was first directly detected by Cowan and Reines in 1956 via inverse beta-decay [2].

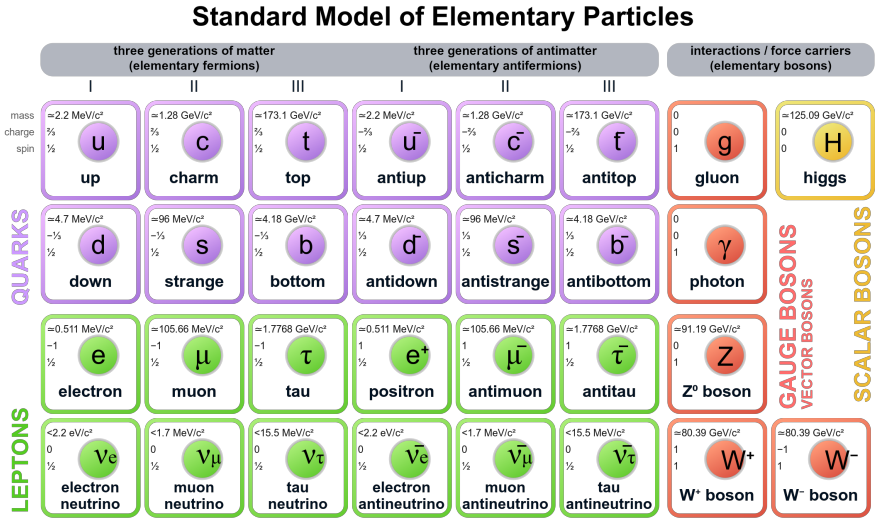

Figure 1.1: Standard Model of elementary particle physics. Graphic taken from [3].

Today three different neutrino flavours, electron (ν_e), muon (ν_μ) and tau (ν_τ), are known. These flavours correspond to the charged leptons with the flavour. Neutrinos propagate in mass states but interact in flavour states, and the flavour states are a linear superposition of mass states that can be described by the Pontecorvo–Maki–Nakagawa–Sakata (PMNS) matrix [4], whose values are determined by experimental measurements [5]. For each flavour, there is a corresponding superposition of the three mass eigenstates. The neutrino masses are currently not known but constrained to $\sum m_\nu < 0.17\,\mathrm{eV}$ [6]. The determination of the mass is difficult because it is very low relative to the measurable neutrino energies. But efforts are currently underway to determine the masses or at least set tighter constraints

[7][8][9]. Other experiments try to determine the mass ordering [10][11] of the three flavours. This effort is complicated by the fact that neutrinos only interact via the gravitational and the weak forces. Due to the low mass, gravitational effects are not detectable, and the cross-section for weak interaction is very small. To overcome the small cross-section, most neutrino experiments use large detection volumes [12][13][14].

1.2 Sources

Neutrinos are omnipresent and come from a range of natural and artificial sources. Examples of such sources, sorted by their distance to the earth's surface, include

- **Natural radioactive decays** - Neutrinos produced by $\beta^{\pm}$ decays of radioactive isotopes have energies of O(MeV). They are produced all around us by trace amounts of radioactive materials.
- **Reactors** - Reactor neutrinos are produced by neutron-rich daughter nuclides of the fission products that undergo one or more β^- decays ($n \rightarrow p + e^- + \overline{\nu_e}$) until reaching a stable configuration. They carry approximately 4.5 % of the energy released in nuclear reactors. The flux of reactor neutrinos can be used for oscillation measurements and for the supervision of nuclear treaties [15].
- **Accelerators** - Long-baseline experiments often use targeted neutrino beams [16]. To produce a neutrino beam protons are accelerated at a fixed target to produce pions and kaons that decay to neutrinos and other particles. Accelerators have the advantage over reactor neutrinos that the energy and the direction of the beam can be adjusted and thus can reach higher rates over long distances.
- **The Earth's atmosphere** - Neutrinos produced by cosmic rays interacting with the atmosphere. Similar to the interaction of accelerator neutrinos, the interaction of cosmic rays in the upper atmosphere produces pions and kaons that decay producing neutrinos among other particles.
- **Sun** - The fusion of two protons to a deuterium core ($p + p \rightarrow d + e^+ + \nu_e$) in the sun produces a positron and electron neutrino with about 400 keV. This process accounts for about 86 % of the neutrinos produced in the sun. More neutrinos are produced in later stages of the fusion chain. When Beryllium-7 is formed from a Helium-3 and a Helium-4, it can then either capture an electron or a proton. Most often (99.86 %) an electron is captured and Lithium-7 and an electron neutrino are produced. 0.14 % of the time, Beryllium-7 combines with a proton producing Boron-8 and a photon. Boron-8 will then do a β+ decay thus producing an electron neutrino too. The complete standard solar model with these reactions is shown in fig. 1.2, where reactions that produce neutrinos are shown with a grey background.
- **Core collapse supernova** - In stars, the radiation from the fusion reaction creates outwards pressure. In massive stars elements up to iron can be fused to release energy. Heavier elements do not release energy during the fusion process. When all lighter elements in the core are fused the star dies and no outward pressure is produced any more. In core-collapse supernova or Type II supernova, the gravitational pressure of a dying star is strong enough that it cannot be counteracted by the electron degeneracy pressure. This forces electrons and protons in the core to undergo inverse β-decay, producing large amounts of neutrinos. So far only one supernova of

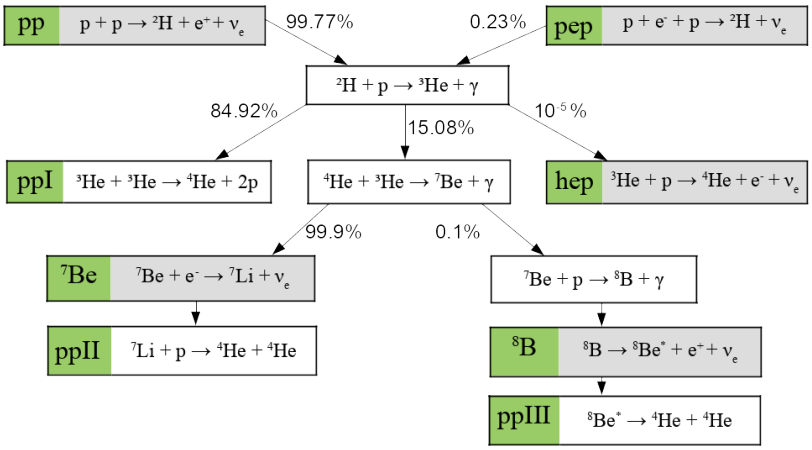

Figure 1.2: The standard solar model with neutrino producing reactions marked with a grey background. Graphic design and content based on [17].

this type (SN1987A) has been observed in neutrinos. It was recorded by three detectors around the world, being the first astronomical source of neutrinos detected on Earth besides the Sun [18].

- **High energy cosmic rays** - Since the first detection of extragalactic neutrinos [19], the focus of attention has been the detection of their sources. It is believed that the sources of neutrinos and cosmic rays are strongly related. A recent coincidence detection between gamma-rays and neutrinos gives strong evidence [20] that blazars[1] are at least contributing to the extragalactic neutrino flux. Still, extragalactic neutrinos and their sources are the least understood and will be an interesting research field in the future.

- **Relic neutrinos** - By numbers the largest proposed source of neutrinos, also called the Cosmic Neutrino Background (CNB) [21], was emitted two seconds after the Big Bang. It is analogue to the Cosmic Microwave Background (CMB) [22]. While there is indirect evidence of its existence from CMB measurements [23], it has not been experimentally detected. This is due to the low energy of those neutrinos, estimated between μeV and meV.

An overview of the listed sources and their energies is shown in fig. 1.3. The extraterrestrial sources listed are especially interesting, since they do not just allow the studies of the neutrino and its properties, but also of their sources, that cannot be easily obtained by other means. Since neutrinos can pass through matter almost unhindered, it is possible to study the inner processes of the Sun or cosmic events behind obstacles, as well as the obstacles themselves, when using neutrinos to generate tomographic images [25]. Most notable, though, is the combination with other messenger particles in so-called multi-messenger astronomy [18][20]. In multi-messenger astronomy, information from different observatories and types of particles are combined to study galactic and extragalactic sources. This allows for a better understanding of the sources and the determination of tighter constraints on physical parameters.

[1] An active galactic nuclei (AGN): galaxy with a supermassive black hole, with a relativistic jet that is ionized particles with high energies, directed at earth.

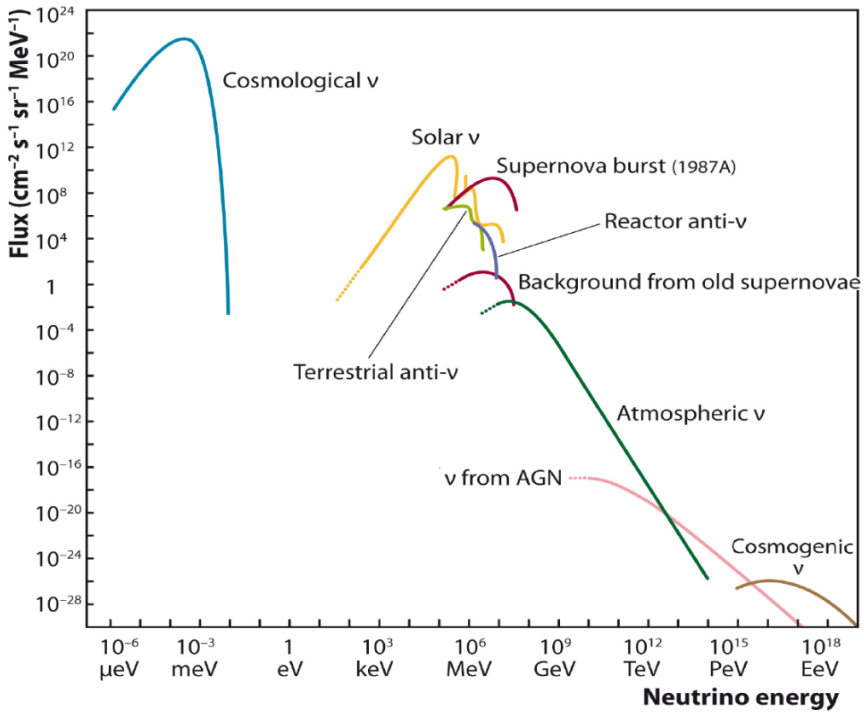

Figure 1.3: Comparison of different neutrino sources, measured and expected, in energy and flux. Taken from [24]

1.3 Detection Principles

With current technology, neutrinos can only be detected by weak interactions. All current detection methods require a minimum threshold energy of the neutrinos. The weak force allows for two types of neutrino interactions, namely charged current (CC) and neutral current (NC). In the CC case, a $W^{\pm}$ boson is exchanged and in the NC case a Z^0 boson. Examples of CC and NC interactions at high energies with nucleons are given in fig. 1.4. The relative large masses of about 80 GeV of the two bosons are the reason for the small cross-section and thus the elusive nature of neutrinos. In the following, the basic principles of different detection methods will be explained with a strong focus on methods relevant in the context of this thesis.

Cherenkov Light

A detection method used in many neutrino detectors such as IceCube is based on Cherenkov light. Cherenkov light, also known as the Vavilov–Cherenkov radiation (VCR)[2], is produced when a high energetic charged particle exceeds the speed of light in a dielectric medium.[3] Due to special relativity, no information and thus matter can travel faster than the speed of light in vacuum $c = 299,792,458\,\frac{\mathrm{m}}{\mathrm{s}}$. The speed of light is the propagation velocity of all massless particles, such as photons, in a vacuum. In a medium, the velocity of photons scales with the inverse of the refractive index n. This means matter can travel faster than the speed of light in medium $\frac{c}{n}$ but must be slower than the speed of light in vacuum c. If a charged particle P travels through a dielectric medium with refractive index n and

[2] named after Sergey Vavilov and Pavel Cherenkov
[3] exceptions apply [26]

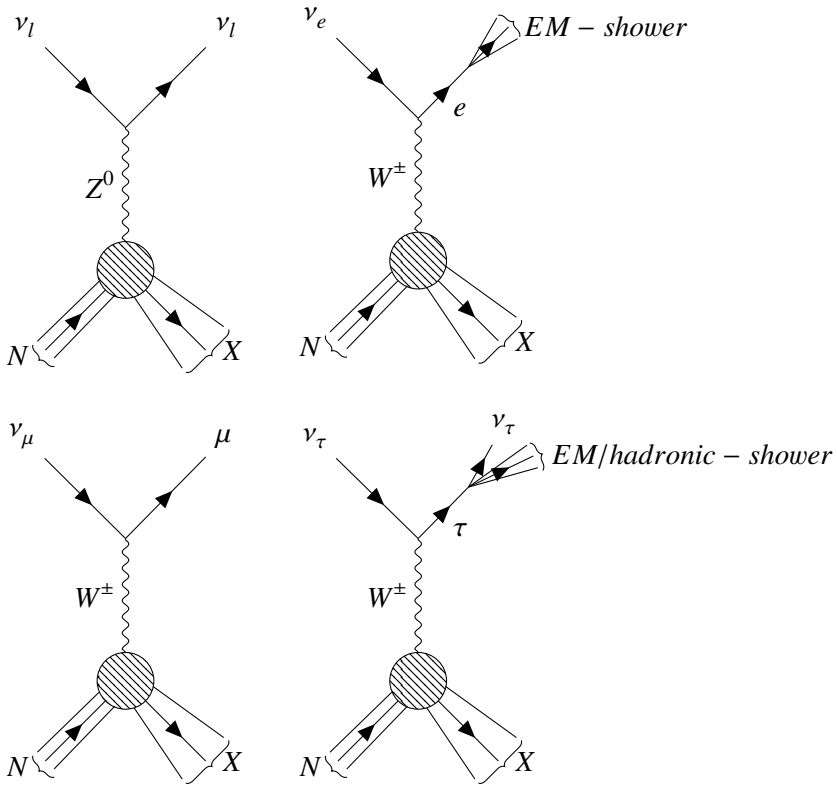

Figure 1.4: Feynman diagrams for deep inelastic scattering of neutrinos with nucleons. The same diagrams hold valid for anti-neutrinos when arrow directions are reversed. (top left) NC interaction for all neutrino flavours $l \in \{e, \mu, \tau\}$. (top right) CC interaction for electron neutrinos. (bottom left) CC interaction for muon neutrinos. (bottom right) CC interaction for tau neutrinos including the tau decay.

a velocity v_P such that $\frac{c}{n} < v_P < c$, Cherenkov light is produced. For subluminal velocities $v_P < \frac{c}{n}$ of charged particles, a traversed dielectric medium becomes momentarily polarized by the electric field created by the charged particle. For velocities larger than $\frac{c}{n}$, the response time of the medium is too slow and no polarisation occurs, the emitted energy is directly emitted as a coherent shockwave analogue to a sonic boom. This shockwave is only emitted in one direction[4], creating a cone-shaped light beam as the particle traverses the medium. The angle (Θ) depends only on the refractive index and the velocity of the particle, as described by eq. 1.1.

$$\cos(\theta) = \frac{c}{n v_P} \tag{1.1}$$

An illustration of this is shown in fig. 1.5. More important in the context of this thesis is the spectral behaviour of the Cherenkov light. The energy emitted by the Cherenkov effect per unit length and frequency is determined by the Frank-Tamm formula (eq. 1.2).

$$\frac{d^2E}{dx\,d\nu} = \frac{4\pi^2 Z^2 e^2 \nu}{c^2}\left(1 - \frac{c^2}{v_P^2 n^2(\nu)}\right) \tag{1.2}$$

Here Z denotes the number of electron charges e of the traversing particle, ν its frequency, E its

[4] exceptions apply [27]

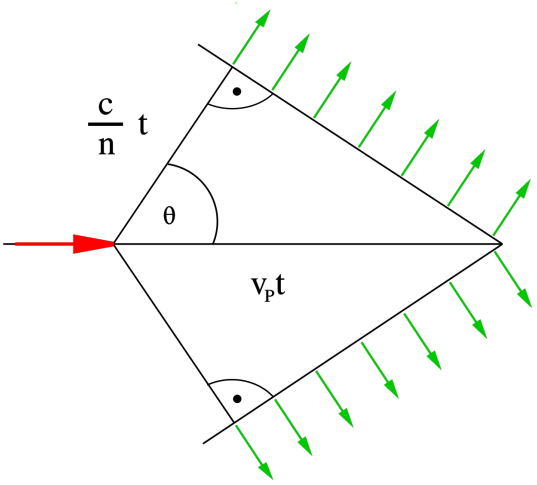

Figure 1.5: Illustration of the geometrical relations in a Cherenkov light cone.

energy and x the distance it travelled. To look at this in terms of wavelength λ and number of photons N, the substitutions $\nu = \frac{c}{\lambda}$ and $E = N \cdot \frac{hc}{\lambda}$ are done respectively. The result is given in eq. 1.3. Further simplifications using eq. 1.1, with n = const. and the fine-structure constant $\alpha = \frac{2\pi e^2}{hc}$ yield eq. 1.4.

$$\frac{d^2N}{dxd\lambda} = \frac{4\pi Z^2 e^2}{hc\lambda^2}\left(1 - \frac{c^2}{n^2(\lambda)v_P^2}\right) \tag{1.3}$$

$$= \frac{2\pi Z^2 \alpha}{\lambda^2}\sin^2\theta \tag{1.4}$$

It becomes apparent, that the number of photons is linear with charge and distance travelled. As a function of wavelength though, the number of photons increases quadratically with the inverse of the wavelength. That means there are many more photons in the UV than in the blue region of the electromagnetic-spectrum. Due to its UV sensitivity, the sensor developed in this thesis greatly profits from this in comparison to similar devices. Towards very short wavelengths, however, the spectrum is cut off by the refractive index $n(\lambda)$ approaching unity.

1.3.1 Processes and Methods for Neutrino Detection

The most prominent detection processes for neutrinos are inverse beta-decay [28] and deep inelastic scattering with other particles. In the latter case, most often Cherenkov light produced by secondary particles is used for detection.

- **Induced beta-decay** - To detect extremely low energy neutrinos in the sub-eV range the use of induced beta-decay is being considered [29]. These sub-eV neutrinos, such as from the CNB, are extremely difficult to detect and thus have not been directly detected yet. For inverse beta-decay, the necessary energy threshold to convert a neutron to a proton or vice versa in a given element has to be overcome. With induced beta-decay, the threshold is removed by using already unstable elements. This creates a large background of spontaneous decays. Therefore a very accurate energy measurement of the produced electrons(positrons) is necessary to differentiate between

them. Depending on the type of decay both electron and anti-electron neutrinos can be detected with this method. An experiment that tries to implement this method with tritium to detect electron neutrinos is the PTOLEMY experiment[5] [30].

- **Radiochemical** - Methods based on radiochemical neutrino-detection are only used to count neutrinos since energy and directional information are lost. A large volume of a specific radio pure element is set up. Then, neutrinos convert a few atoms to different elements isotopes via inverse beta-decay. These few isotopes can then be filtered out and counted. Exemplary elements are Chlorine-37 that is converted to Argon-37 as used in the Homestake experiment [31] or Gallium-71 that converts to Germanium-71 as in the SAGE experiment [32]. For the former experiment, the threshold energy is 0.814 MeV and for the later 0.233 MeV. This method is mainly used for the detection of solar neutrinos since they dominate in numbers, as it can be seen in fig. 1.3. Also, the energy thresholds for non-electron neutrinos is much higher and thus all non-solar electron-neutrinos can be considered as background.

- **Scintillators** - A scintillator is a crystals or doped material like plastic or oil that emit visible and/or UV-light when excited by ionizing radiation. They are used for neutrino detection with a variety of reactions. The Cowan–Reines neutrino experiment [33], for instance, used a solution of cadmium chloride in water as a target. Neutrino induced beta-decay took place, producing positrons and neutrons. The former underwent a positron-electron annihilation that produced two 511 keV photons. These were detected with scintillators next to the target. Another experiment using scintillators is Borexino [34]. The target and (liquid) scintillator are the same material. It uses neutrino-electron scattering to detect neutrino energies below one MeV. While the focus lies on all types of solar neutrinos, anti-neutrinos from radioactive decays and nuclear power plants can be detected as well. The experiment is potentially also able to detect neutrinos from a galactic supernova. Scintillator neutrino experiments usually do not obtain directional information but in return allow the detection of low energy neutrinos with a very good energy resolution.

- **Cherenkov** - Cherenkov detectors observe secondary charged particles from neutrino interactions by measuring their Cherenkov light emission. The production of the secondary particles is possible via various channels. CC and NC interactions of all flavours with nuclei or electrons can be detected. The energy threshold varies depending on the interaction type and the experimental setup but it can be as low as a few MeV. Due to the directional properties of Cherenkov light and the strong directional correlation between neutrino and secondary particles, a good directional resolution can be achieved with this type of detectors. Examples are the Super-Kaminkande experiment [13] with a 40×10^3 m^3 volume and 11,200 Photomultiplier Tubes (PMTs) for photon detection or IceCube [14] with a 1 km^3 volume and 5160 PMTs. This type of detector can also be combined with a scintillator such as in MiniBooNE [35] to lower the energy threshold. The energy resolution is limited by the detector geometry, material and the photon detection efficiency. Flavours can be determined in CC interactions based on the event topology. A section on event topologies in large volume neutrino detectors follows after this one (section 1.3.2). The energy of the detectable neutrino sources can span from MeV to PeV depending on the individual detector.

- **Radio** - Also radio emissions can be used to detect neutrinos, when the detection volumes become too large to reasonably deploy enough sensors to detect events via Cherenkov light. This is usually the case for neutrino energies beyond the PeV range, where events are very rare. The detected radio emission in these experiments either comes from the tail of the Cherenkov distribution or

[5] Princeton Tritium Observatory for Light, Early-Universe, Massive-Neutrino Yield

the Askaryan effect. The Askaryan effect describes the production of radio waves by a charge asymmetry in high energy particle cascades, as they are produced from secondary particles. All types of neutrinos can be detected with this method, though the flavour discrimination capabilities depend on the individual experiment and its constraints. Usually, good energy and directional resolution can be achieved. Examples are ARA [36] for radio detection in ice or ANITA [37] for radio detection in ice from a balloon. An observation of neutrinos interacting in the Moon's surface with the Square Kilometre Array is also planned [38].

1.3.2 Event Topologies in Large Volume Neutrino Detectors

In ice as well as in water both the NC and CC interactions take place. To detect these interactions in a large volume neutrino telescope such as KM3NeT [12], Baikal-GVD [39] or IceCube, the primary neutrinos need sufficiently high ($\approx 10 - 100\,\mathrm{GeV}$) energies. Only at those energies enough Cherenkov light is produced by the secondary particles for it to be detected in several of the optical sensors (or modules). The modules have spacings between several meters and several tens of meters. These high energy interactions are dominated by deep inelastic scattering, which can take place in six different types of interactions: one NC interaction per neutrino flavour and one for CC interaction per neutrino flavour. The interactions can be described by eq. 1.5 and 1.6, where $\overset{(-)}{\nu}$ denotes an (anti-)neutrino, l any of the three lepton flavours (e, μ, τ), N any nucleon and X one or multiple hadronic particles including a hadronic cascade.

$$\overset{(-)}{\nu}_l + N \rightarrow l^{\pm} + X \quad \text{(CC)} \tag{1.5}$$

$$\overset{(-)}{\nu}_l + N \rightarrow \nu_l + X \quad \text{(NC)} \tag{1.6}$$

The corresponding Feynman diagrams are depicted in fig. 1.4. The corresponding detector signatures can be classified into three groups.

- **Showers** signatures are expressed in a spherical to elliptical distribution of light. An example event in IceCube[6] is shown in fig. 1.6. Most of the photons are produced by charged secondary particles near the interaction point and scattered many times before being detected. The resulting near spherical-structure only allows for a very low directional resolution. In most cases, the whole shower is completely contained in the detection volume, allowing a good energy reconstruction. Four different interactions can create this signature. All three NC interactions result in a hadronic shower that produces this signature. The CC interaction with the electron (anti-)neutrino additionally produces an electromagnetic shower, that is indistinguishable from the hadronic shower (with the resolution of most large volume neutrino detectors).

- **Tracks** signatures are expressed as a long line through the detector. An example is shown in fig. 1.7. Tracks are produced by high energetic muons crossing the detector. They produce Cherenkov light while passing through ice or water. They can come from cosmic radiation or from a CC interaction of a muon neutrino ν_μ. If the muon is produced from a muon neutrino within the detector it is called a starting event. This usually involves a shower, in form of a hadronic cascade, at the start of the track. The muon does not produce electromagnetic showers in the way the electron does, thus it produces a track. Along the track, the muon may undergo stochastic energy losses and produce smaller showers along the way. Since the muon does not deposit all of its

[6] A detailed description can be found in the next chapter (section 2.1).

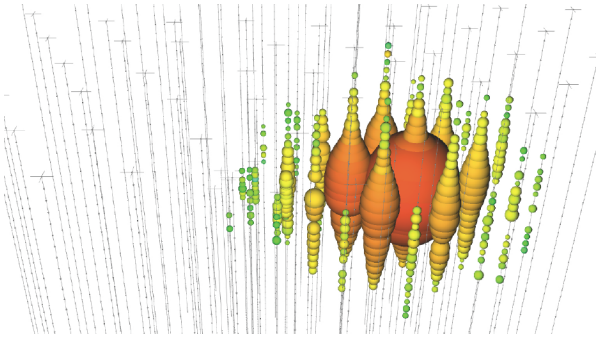

Figure 1.6: A neutrino event in IceCube with a shower signature. Each sphere is a DOM. The size of the sphere indicates the numbers of photons detected. The colour reflects the arrival time of the first photon at that module from red (early) to blue (late). Image taken from [40]

.

energy at once, it is often not contained in the instrumented volume and only lower limits on the particle energy can be derived. However, due to the long track, the direction can be very well reconstructed. Furthermore, due to the high energy, the direction of the primary and secondary particle almost perfectly align in the observer frame. This makes these interactions the primary tool in the search for high energy neutrino and possibly cosmic ray sources.

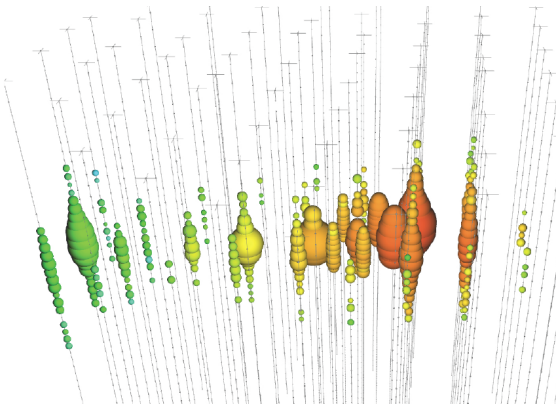

Figure 1.7: A muon, produced from a muon neutrino CC interaction, passing through the IceCube detector (left to right). Image taken from [40]

- **Double Bangs** signatures express themselves through two showers connected by a track of comparatively low light emission. An example is shown in fig. 1.8. This event signature is produced by tau neutrinos undergoing CC interactions in the detector. They initially produce a tau and a hadronic cascade. The tau traverses the detector like a muon. Due to its short lifetime, the tau decays very close to its origin. In 65 % of the cases, another hadronic cascade is produced. In all other cases, a leptonic decay occurs. In the leptonic decay channel, about half of the events produce an electron and thus another, electromagnetic, cascade. The other half produces a muon, leading to a track-like signature. However, very high energies (> 100 TeV [41] deposited energy) are needed to resolve individual showers/cascades. So far only two candidate events have been observed [41]. This analysis searched for a smaller separation of the two cascades that cannot be resolved by eye. Instead, a complex numeric reconstruction based on Monte Carlo simulations is applied [42]. These events have to be evaluated with a lot of care since other types of events can

potentially mimic this signature. For instance, a muon with two pronounced stochastic energy losses can have a similar signature.

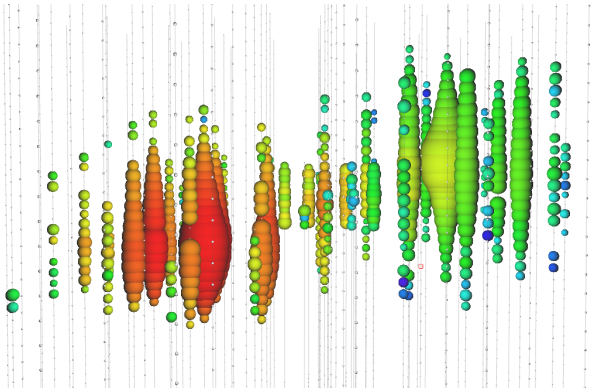

Figure 1.8: A simulated double bang event, with a primary tau neutrino interacting and producing a tau that travels through the detector and then decays. Image taken from [40].

CHAPTER 2

IceCube

In this chapter, the physics and design of the IceCube Neutrino Observatory will be described [43]. The main IceCube detector is comprised of a cubic kilometer instrumented volume of natural ice at the South Pole. The main focus of the detector is set on cosmic neutrino detection, yet it is a multi-purpose detector offering the possibility to study other domains such as cosmic rays, earth tomography and beyond the standard model (BSM) physics [44].

2.1 Detector Design

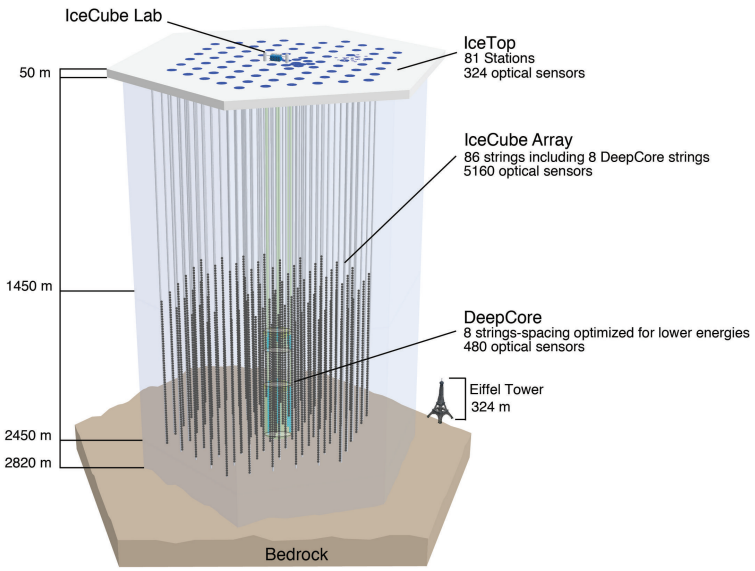

Figure 2.1: Schematic view of the IceCube detector. The IceCube Array is the main detector. IceTop is the surface detector for vetoing and cosmic ray detection. DeepCore is a densely instrumented volume within the IceCube Array for lower energy detections mainly used for particle physics. Figure taken from [45].

The IceCube detector (fig. 2.1) is located a few hundred meters away from the geographic South Pole. The IceCube array consists of about a cubic kilometer of instrumented glacial ice. It is located between 1450 and 2450 m below the surface and has a hexagonal footprint. The 86 cables for power and data

with instrumentation, also called strings, have been deployed using a hot-water drill. The strings hold a total of 5160 digital optical modules (DOMs), that is 60 DOMs each. DOMs are the light sensors of the detector which produce a digital signal when they detect one or more photons. Apart from DeepCore, the average distance between strings is 125 m and the spacing between DOMs in the vertical is 17 m. DeepCore is an eight-string subdetector in the center of IceCube, that is more densely instrumented. The dense instrumentation facilitates lower energy measurements, such as oscillation studies. DeepCore's energy threshold is about 10 GeV, in contrast, IceCube's energy threshold is 100 GeV. Additionally, a veto and cosmic ray detector called IceTop is installed on the surface. It consists of 81 Stations, each having two ice tanks with two DOMs each. All detectors send their data to the IceCube Lab (ICL) which is a central data processing and storing facility on the surface and in the center of IceCube. The ice is used as an interaction volume for neutrinos. The ice is very clear and it is therefore, well suited for the Cherenkov light (produced by secondary particles in neutrino interactions). The Cherenkov photons can then be detected by the DOMs.

2.2 Digital Optical Module (DOM)

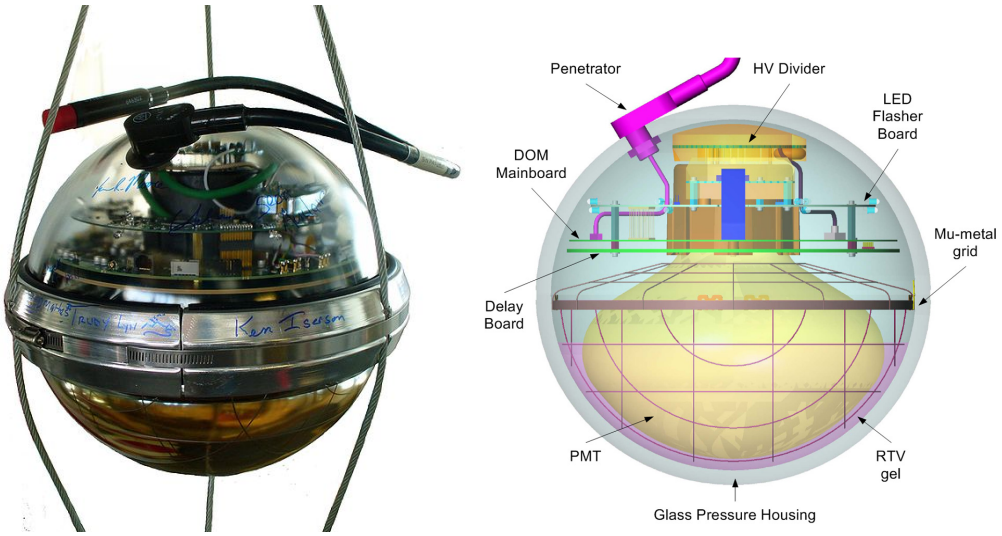

Figure 2.2: (left) Photograph of an IceCube DOM. (right) Schematic view of an IceCube DOM. Electrical components for power supply, data exchange and processing as well as calibration light sources are situated in the upper half. The lower half contains the PMT for photon detection. Figure taken from [45].

The DOM is the sensor used for photon detection within IceCube. A photograph and a schematic can be seen in fig. 2.2. It consists of a spherical borosilicate pressure-vessel. The lower half is mostly occupied by the 10 inch photomultiplier tube[1] (PMT). To shield the PMT from Earth's magnetic field it is encompassed in a mu-metal cage. To reduce the number of photons lost by total reflection inside the pressure-vessel, the gap between the pressure-vessel and the PMT is filled up with optical gel[2]. The upper half houses the electronics of the module. It consists of four different electronics boards and a penetrator. Through the penetrator, the DOM is connected to the main cable, supplied with the required power for operation and communicates with the ICL. The uppermost board is the high voltage

[1] Hamamatsu R7081-02 [46]
[2] WACKER SilGel 612

baseboard, which distributes the high voltage over the different dynodes of the PMT. The high voltage is generated with a high voltage generator on the flasher board. The flasher board hosts 12 LEDs for calibration purposes, half of which face sideways and half face 45° upwards. Below the flasher board is the main board, containing an FPGA, an ARM CPU, a digitizer, a low voltage DC-DC converter and further support electronics. The last board below the mainboard is the delay board. It is used to delay the signal after the detection before the decision for digitization is made. The complete module has a noise rate below $500\,\mathrm{s}^{-1}$ [46] for typical temperatures in the ice (-40 to $-20\,\mathrm{C}^{\circ}$ [47]). During the design of IceCube, it was assumed that it would be difficult to differentiate down going neutrinos from cosmic rays. Therefore the angular sensitivity is concentrated downwards since neutrinos coming through the earth should have less background from cosmic rays and thus the better signal to noise ratio. The wavelength acceptance is primarily defined by the PMT sensitivity. Both angular sensitivity for photons and wavelength acceptance of the DOM are shown in fig. 2.3. In fig. 2.4, heat maps of the position dependence of the light pulse response are shown for three different PMT and an average of the PMTs. The visible inhomogeneities are caused by the orientation of the dynodes.

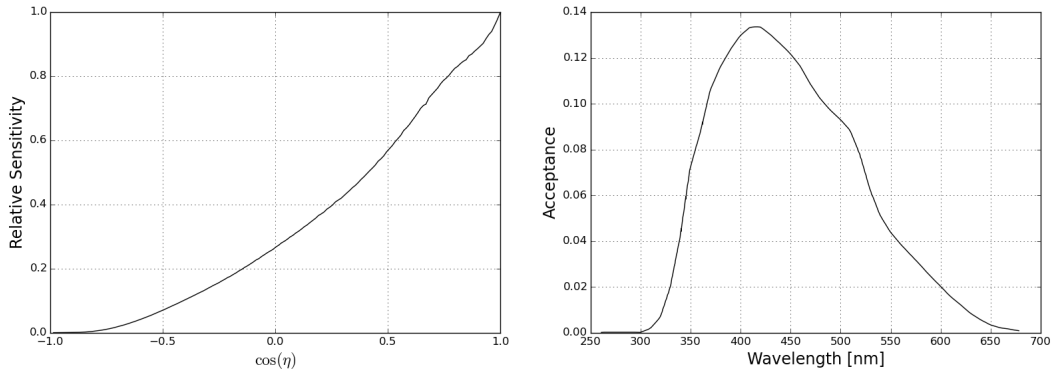

Figure 2.3: (left) Angular sensitivity for an IceCube DOM where η is the photon arrival angle with respect to the PMT symmetry axis. The distribution is normalized to 1 at $\cos(\eta) = 1$. (right) Wavelength dependent acceptance of the IceCube DOM for a parallel light beam from below ($\cos(\eta) = 1$) over the whole cross-section of the DOM. This includes the PMT, the glass of the pressure-vessel, the mu-metal cage and gel. The information used for these plots is extracted from internal IceCube software.

2.3 Properties of the Antarctic Ice at the South Pole

The glacial ice at the South Pole is one of the cleanest and most transparent ice on our planet [48]. The ice was deposited over millennia. Each subsequent layer compresses the underlying layers further until very homogeneous ice is created. Under the constantly added weight, the entire glacier moves at about 10 m per year [49]. Due to the age of the ice and its source being atmospheric vapour, the optical background from radioactive decays is very low. The extreme cold excludes bio-luminescence as it appears in ocean-based experiments and reduces background from the intrinsic dark noise of PMTs. In comparison to water-based experiments, the ice also allows for larger absorption lengths in return for shorter scattering lengths. Thus the signal to noise ratio (SNR) in ice is better than in ocean-based experiments.

A comparison of absorption coefficients between the South Pole ice and laboratory ice can be seen

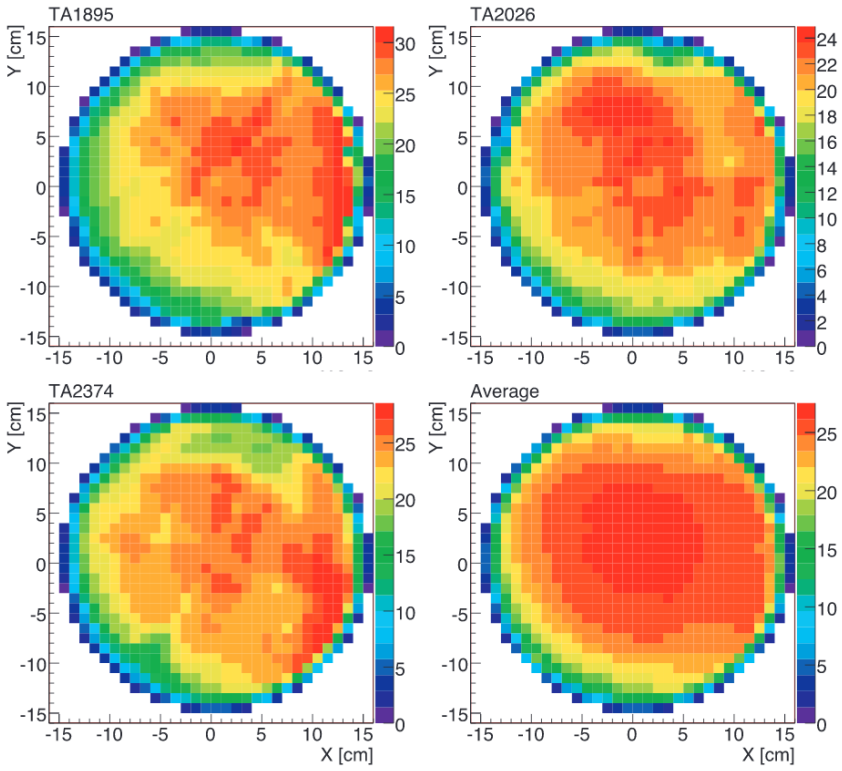

Figure 2.4: Position dependence of the IceCube PMT sensitivity. Three individual PMTs and 135 PMTs averaged (lower right). The X-Y coordinates measure the distance from the center of the photocathode along the curved PMT area. The colour indicates the output pulse charge in units of the single photoelectron (SPE) charge, averaged over many pulses. Taken from [46]

in fig. 2.5. The fit used here is separated into three ranges. The absorption coefficient of the ice is modelled by an exponential law in the IR. In the VIS to UV, it is described as a power law λ^{-2} scaled with a dust factor. At even shorter wavelength there is a cut off in the UV, the so-called Urbach tail. The Urbach tail is a exponential decrease in absorptivity that corresponds to an electronic band-gap in the ice with an experimentally determined pre-factor [48]. The reason for the much better performance of the South Pole ice in comparison to the lab ice is due to the air bubbles being converted to non-scattering air hydrates under the high pressures. More details can be found in [50] and [48]. Specifically, in the framework of this doctoral thesis, where a sensor for single-photon detection with a focus on UV-light has been developed, the high transparency for UV light has to be noted. This UV-light transparency is not present in water, therefore the detector developed in this thesis is especially useful for Cherenkov light detection in ice. It also shows that the ice properties change with depths. This is caused by the different deposited ice layers. They differ due to changes in climate and dust composition in the atmosphere during deposition. This layering can be seen even better in fig. 2.6. The absorption and the scattering coefficients are shown for different wavelengths and depths. The peaks correspond to stadials during the last glacial period [51]. However, the peak at about 2100 m depth is associated with volcanic activity. This so-called dust layer can be well seen in the highest energy neutrino event detected with IceCube so far as shown in fig. 2.7. More details on dust can be found in [48].

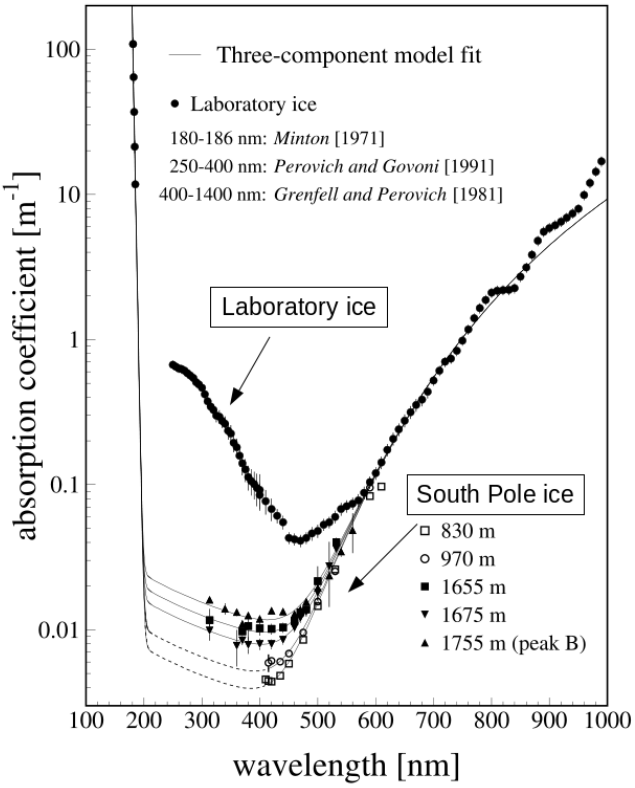

Figure 2.5: Wavelength dependent absorption for South Pole ice and laboratory-grown ice from ≈ 200 to 1000 nm. Figure taken from [48].

Measurements have shown that the optical properties in the ice have an azimuthal anisotropy. The direction of the anisotropy coincides with the moving direction of the ice. The effect is observed in the distribution of detected light. The underlying microscopic reason for this effect is likely a birefringence behaviour of the ice. The alternative explanation of Mie-scattering was recently excluded [52].

The last effect that changes absorption and scattering behaviour is caused by the deployment of the sensor. Due to the melting of ice columns impurities have been brought into those holes as well as existing ones have been redistributed. Furthermore, there are indications for a bubble column in the center of these holes, caused by the refreezing of the ice [53].

2.4 Prospects

Looking back at the field of large volume neutrino detectors, there has been a variety of precursor experiments such as the DUMAND Project[3] [54], BDUNT[4] [55], AMANDA[5] [54] and ANTARES[6] [56]. The first true gigaton[7] neutrino detector is IceCube [14] and will be followed soon by the

[3] Deep Underwater Muon And Neutrino Detector Project
[4] Baikal Deep Underwater Neutrino Telescope
[5] Antarctic Muon And Neutrino Detector Array
[6] Astronomy with a Neutrino Telescope and Abyss environmental RESearch project
[7] Mass of the detection volume.

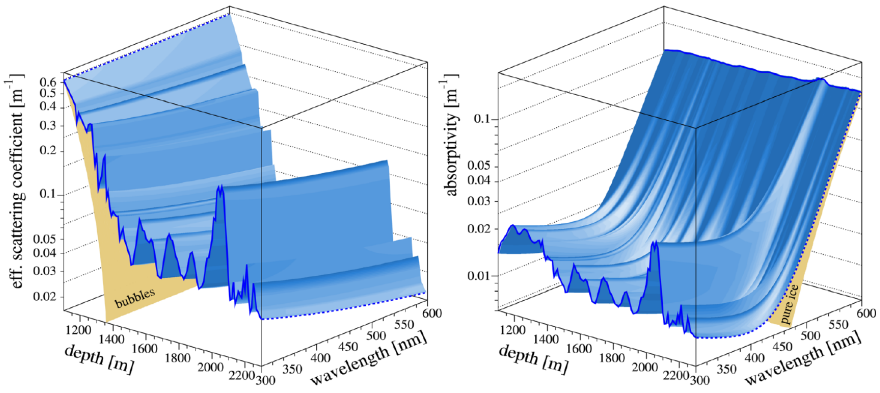

Figure 2.6: (left) Measured scattering coefficient as a contour function of wavelength and depth. Below in light brown, the values expected from the air bubbles that are still present in shallower depths due to lower pressure. (right) Measured absorptivity as contour function of wavelength and depth. Below in light brown the expected values for pure ice. Images are taken from [48].

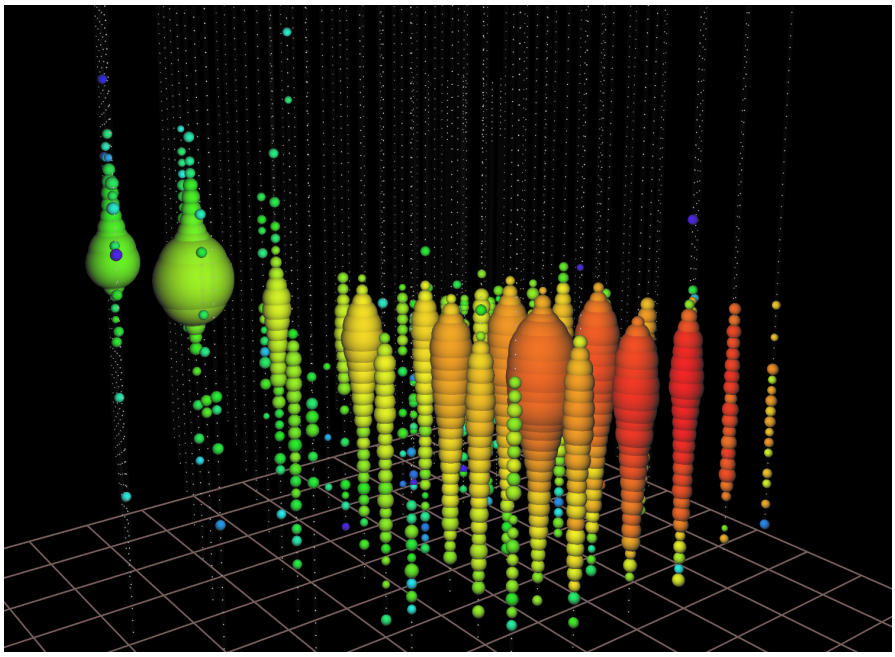

Figure 2.7: Event display of a 2.6 PeV event in IceCube, illustrating photon absorption in the dust layer. This is a contrast to an isotropic distribution, that would be expected without dust. Figure taken from [45].

GVD [39] and KM3NeT [12] experiments. IceCube has had the first major scientific discoveries and breakthroughs in this field. The most important discovery so far is the detection of extragalactic neutrinos [19]. This is accompanied by the highest-energy neutrino detected so far. The latest success is the pinpointing of the blazar TXS 0506+056 as a likely neutrino source [20]. There are many other results and limits obtained by IceCube in many areas, such as cosmic ray physics [57], oscillation parameters [58], dark matter [59] and magnetic monopole search [60]. However, it took many years to obtain a single point source candidate. To improve time and number performance in many of these areas, several extensions for the IceCube detector are planned that will be discussed in the next section.

CHAPTER 3

IceCube-Gen2

3.1 Current Plans and Science Prospects

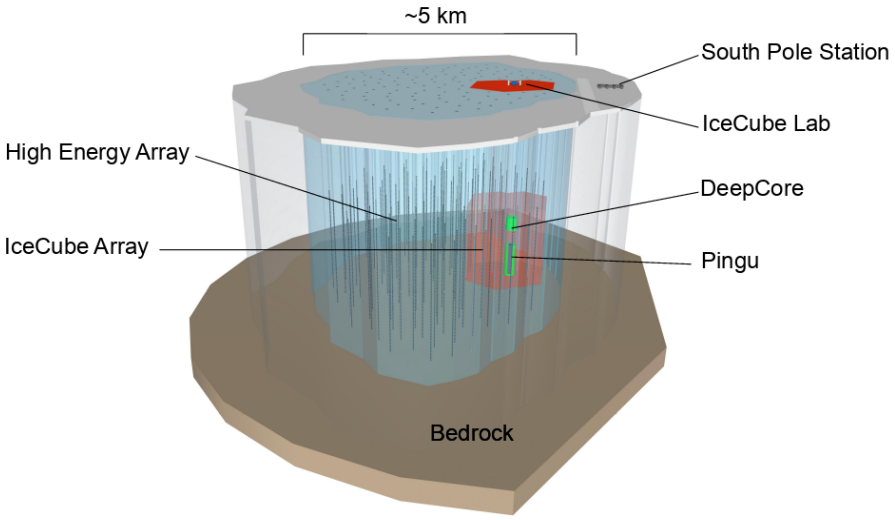

Figure 3.1: Baseline IceCube-Gen2 concept showing the existing IceCube detector surrounded by the planned high energy array and the planned PINGU detector in the center. Figure taken from [45].

IceCube-Gen2 is the name given to an array of future IceCube extensions [61][62].

These extensions address some of the limiting factors in the current IceCube setup. Those are foremost the event rate and angular resolution. Depending on the channel, an increase in event rate between 4 and 10 is aimed for. For the angular resolution, approximately a factor of three increase is targeted. In combination, this will increase the sensitivity to sources five times fainter than detectable today. With the addition of a radio array, the accessible energy range of cosmic neutrinos can be increased further by several orders of magnitude compared to IceCube. The exact structure of these extensions has been changing over time with technical advancements, newly available simulations and changes physics goals, as well as political and financial constraints. A good understanding of the general direction for the planned extension can be obtained from fig. 3.1 and fig. 3.2. Fig. 3.1 shows the original IceCube array as in fig. 2.1 with the two planned extensions named PINGU and High Energy

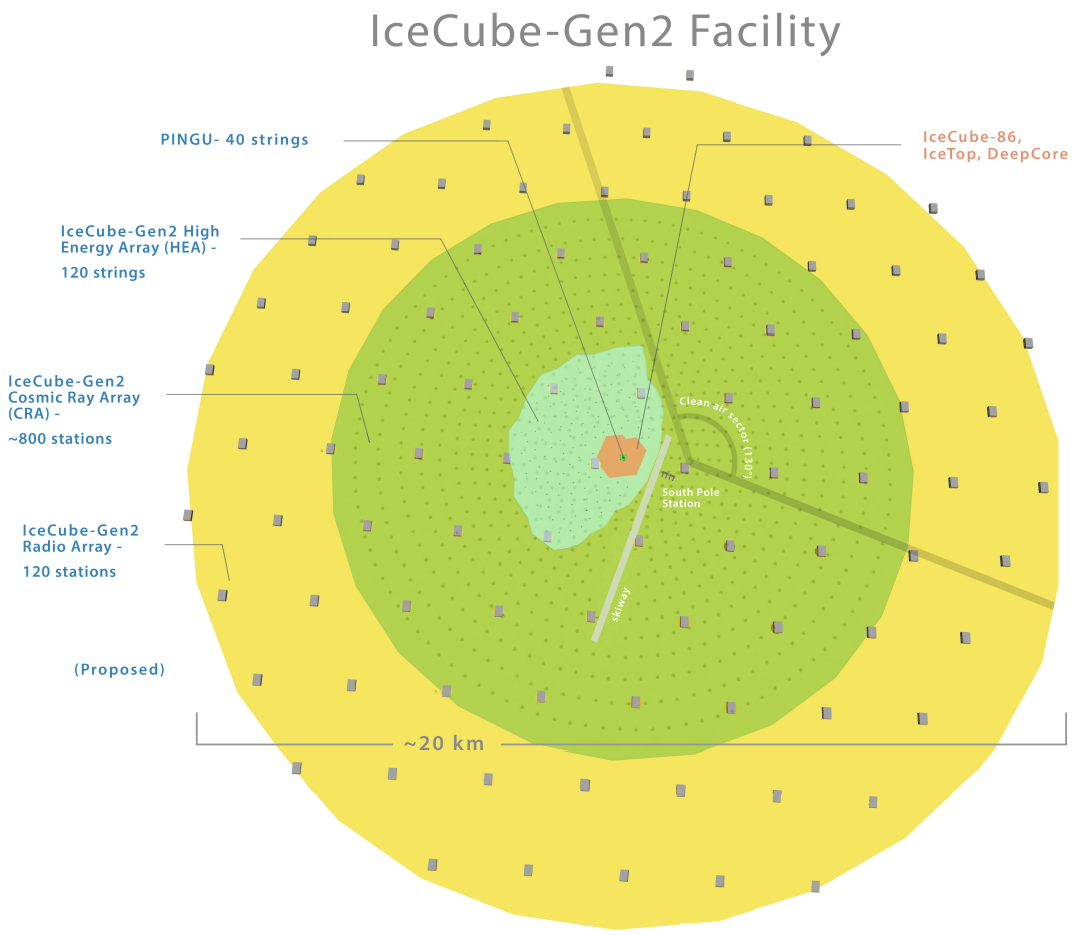

Figure 3.2: Extended IceCube-Gen2 facility concept. Orange labels are used for existing structures and blue for planned ones. White labels indicate IceCube independent structures and areas. Figure taken from [45].

Array. Fig. 3.2 shows a more expansive range of possible extensions. Besides the High Energy Array and PINGU, also a vast Cosmic Ray Array and a Radio Array are shown.

- **High Energy Array (HEA)** is the high-energy extension and the larger of the two optical in ice extensions, that increases the detector volume by almost an order of magnitude.[1] The core motivation behind the high-energy extension is an increase in statistics for point source searches and the detection of GZK neutrinos. GZK neutrinos are produced when cosmic ray protons exceed the Greisen–Zatsepin–Kuzmin (GZK) limit (50 EeV) and interact with the CMB. Both are in the high energy regime. Therefore a much larger string spacing can be used that reduces the costs significantly in comparison to the same volume in IceCube instrumentation. Currently, strings in a comparable number to IceCube are considered with a baseline string spacing of 240 m, while larger spacings were considered too. Additionally, the string length is expanded by 76 m upwards and 175 m downwards, increasing the geometric area for horizontal tracks by about 25 %. The vertical spacing of the optical modules and thus their total number strongly depends

[1] Exact numbers depend on the final design.

on the type of optical module used with its constraints and abilities and thus has not been decided yet.

- **Cosmic Ray Array** will be built after IceCube-Gen2, though its functionality and extend is currently not defined yet. In the ideal case, it will extend beyond the high-energy array and is suitable as a veto for in-ice events as well as an independent cosmic ray detector as shown in fig. 3.2. It would be an extension to IceTop and allow energy and timing resolution in each station. However financial constraints in terms of construction and operation costs make it more likely that it will be limited to a vetoing functionality with a footprint, in the simplest scenario, equal to the high-energy array. Stations are made from scintillator panels. Those panels allow for a reasonable timing but virtually no energy resolution. This could be extended by IceAct [63], a series of small, low cost, air Cherenkov telescopes designed for the harsh conditions at the South Pole. While the observation time would be limited to the winter months and good weather, this would allow a large and cost-effective extension of the veto while simultaneously enabling cosmic ray science.

- **Radio Array** is a possible extension to the IceCube-Gen2 observatory that utilizes radio detectors in dry holes near the surface of the ice. It would allow studying neutrino events with energies beyond 10 PeV due to the extended volume. It would be based on the existing technology, developed for the Askaryan Radio Array (ARA) [64] and the Antarctic Ross Ice-Shelf Antenna Neutrino Array (ARIANNA) [65].

- **IceCube Upgrade** is a small and already funded seven-string extension of DeepCore and shown in the fig. 3.3. This extension allows for an improved atmospheric neutrino event selection efficiency as well as an event reconstruction at a few GeV. IceCube Upgrade will drastically improve the sensitivity to neutrino oscillations including the measurement of tau neutrino appearance. Beyond that, the accuracy of already recorded IceCube data will be improved. To achieve this new calibration devices will be deployed with the Upgrade strings. They will improve the understanding of the detector response and the optical properties of the glacial ice. Including this data into the reconstruction of previously recorded data will improve the accuracy of the results obtained from them. Furthermore new developed equipment such as the optical module discussed in this thesis as well as others can be tested. Construction is currently planned for the austral summer 2022/2023. Additional information can be found in [66].

- **PINGU (Precision IceCube Next Generation Upgrade)** is the less visible extension in the center of DeepCore and focused on low energy neutrino detections. String spacings are reduced to $O(10\,\mathrm{m})$. This allows for more precise measurements of neutrino oscillation parameters and properties. The original intention was to deploy 26 strings in a depth between 2150 and 2450 m, with a total of 4992 sensors [67]. In this case, the sensors would have been improved DOMs, so-called PINGU DOMs (pDOMs), at every 1.5 m. However recent developments have put exact numbers, module types, structures, and even the need for PINGU itself up for debate.

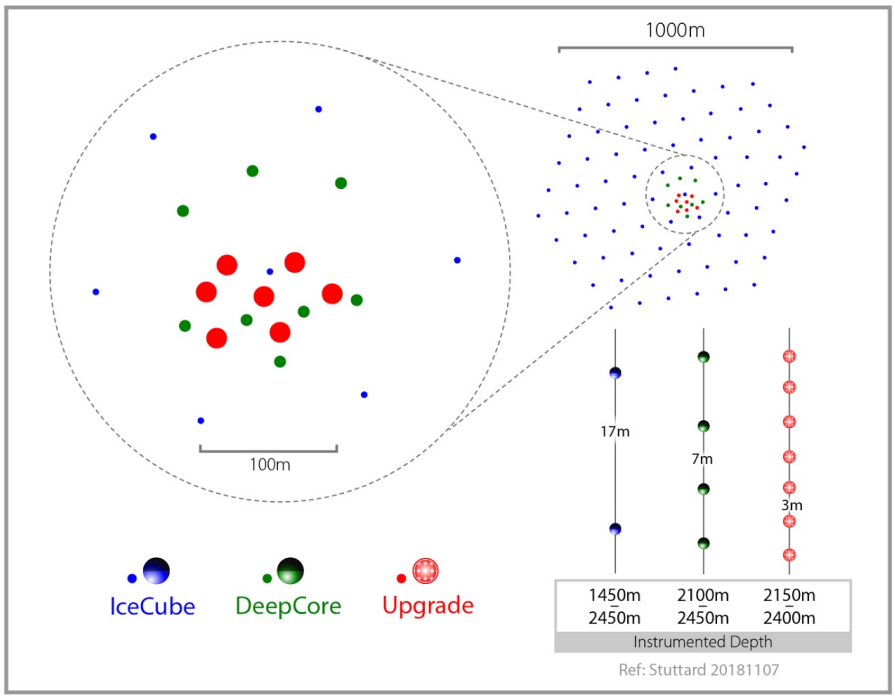

Figure 3.3: IceCube Upgrade. Illustration of a possible configuration. Figure taken from [45].

3.2 New Optical Modules

The most important new developments are the optical modules. There are several different types of optical modules (OMs) currently in different stages of the development process. In the following, these optical modules will be introduced.

3.2.1 PINGU Digital Optical Module (pDOM)

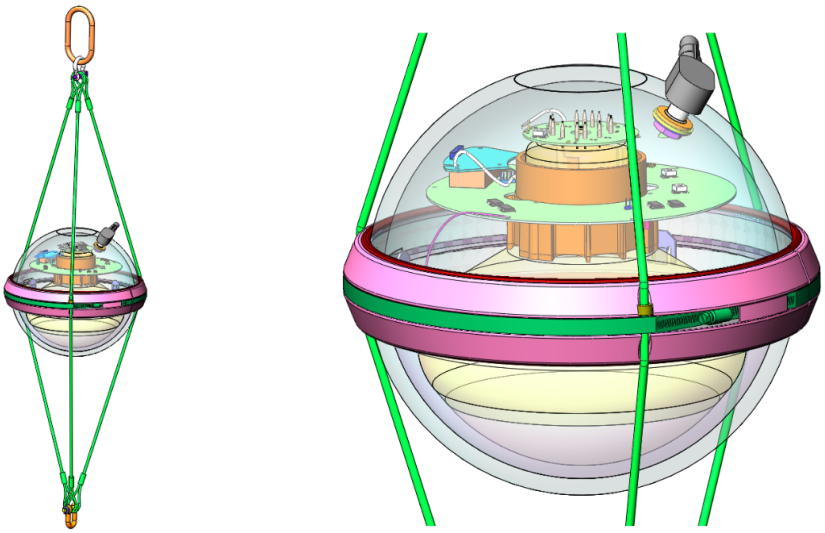

Figure 3.4: Illustration of the pDOM. Image taken from [67]

The pDOM is an updated version of the DOM [68]. As shown in fig. 3.4 it is similar to the DOM design from fig. 2.2. Major changes have thus been done on the electronics. Newly available parts allowed to reduce the electronics to a single board, hosting all the components. The additional space can thus be used to add additional sensors or calibration devices. Power consumption was also reduced. An improved PMT, the Hamamatsu R7081-2-MOD, that increases photon sensitivity, relative to the DOM, by $\approx 35\,\%$ will be used. With the possibility to build a new detector, several other OM designs have also been investigated. Some of the other OM designs have already shown to be superior to the pDOM Therefore, the development of the pDOM was stopped in favour of other prototype-OMs. Since then the performance of the pDOM has been used as a baseline to compare to other OMs. The same will be done in this thesis. Furthermore, the developments made for the pDOM will be modified and used in the other OMs.

3.2.2 Dual Optical Sensors in an Ellipsoid Glass for Gen2 (D-Egg)

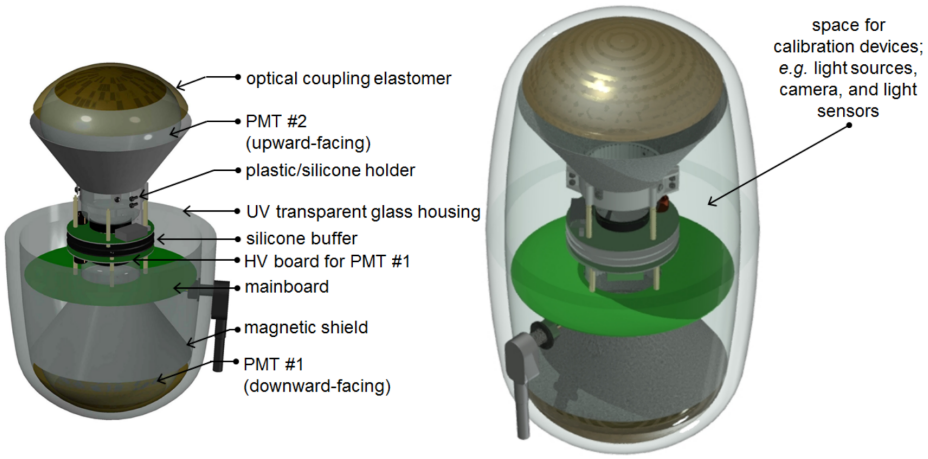

Figure 3.5: Graphic impression of a D-Egg, showing all basic components. Image taken from [69]

The D-Egg is an egg-shaped OM that uses two 8-inch PMTs, with one facing down- and the other upwards [68]. A schematic view of its components can be seen in fig. 3.5. This simple two PMT module increases the photosensitive area while decreasing the module diameter and thus reducing the drilling costs. It has already been shown that it improves photon statistics and reconstruction especially for down going events [70]. Additionally, the space between the PMTs allows for the deployment of additional sensors or calibration devices useful for the detector calibration. The D-Egg is one of the OMs that will be deployed in the physics region of IceCube Upgrade [66].

3.2.3 Multi-PMT Digital Optical Module (mDOM)

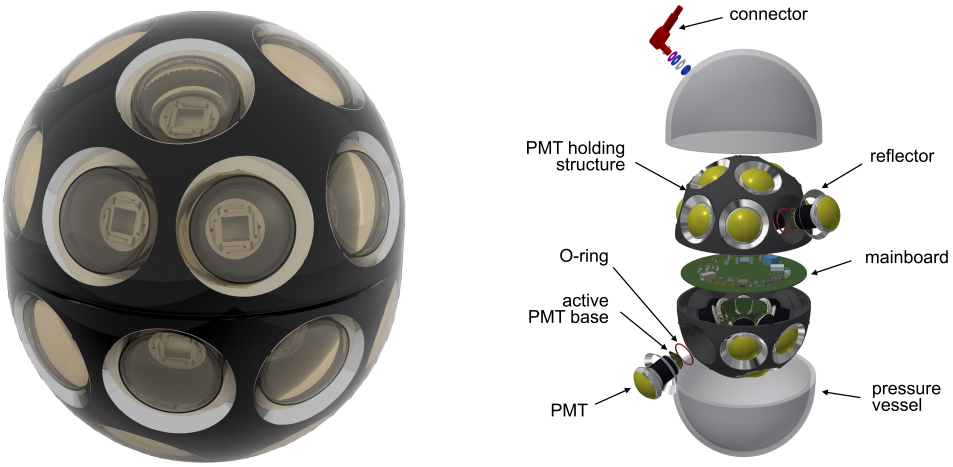

Figure 3.6: (left) Image of an mDOM. (right) Exploded diagram of the mDOM with part description. Figure taken from [45].

The mDOM for IceCube-Gen2 [71] is an adaptation of the mDOM developed for the Km3NeT experiment [72]. It holds 24 3-inch PMTs facing in all directions to increase the photosensitive

area while obtaining directional resolution, intra-module reconstruction and self vetoing within the module. A schematic view and a prototype picture can be seen in fig. 3.6. The 24 PMTs are nearly homogeneously distributed in all directions and their sensitive area is increased with small mirror shields. The electronics are housed in the center and spare areas are blacked out to avoid random reflections of light. Depending on the final design, the mDOM will have a light sensitivity between 2.24 and 2.66 times as sensitive as the pDOM [73]. This efficiency gain is partially compensated by the higher price tag and the larger diameter that increases drilling costs. The mDOM is beside the D-Egg one of the OMs that will be deployed in the physics region of IceCube Upgrade [66].

3.2.4 Wavelength-Shifting Optical Module (WOM)

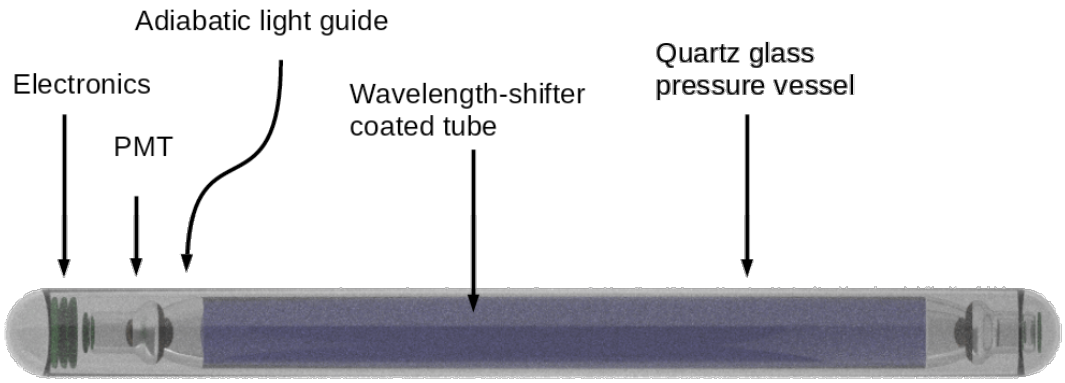

Figure 3.7: Graphic representation of a WOM showing all essential components without holding structures in a sideways position. The image is based on works of [74]

The WOM [75] is designed to increase the photosensitive area, decrease the noise rate, reduce costs and make more use of the UV-range of the Cherenkov spectrum in comparison to the pDOM. This is done by using a wavelength-shifting technology and total internal reflection to capture and transport the light to two small PMTs. That way the module can have a large photosensitive area with only two small PMTs. This increased sensitivity is accompanied by a decrease in timing resolution. A schematic of the whole module is given in fig. 3.7. With this slim and elongated pressure-vessel drilling cost can be further reduced. Since the WOM is the subject of this thesis a more detailed description of the hardware used and physical processes involved in this module can be found in chapter 4.

3.2.5 Long Optical Module (LOM)

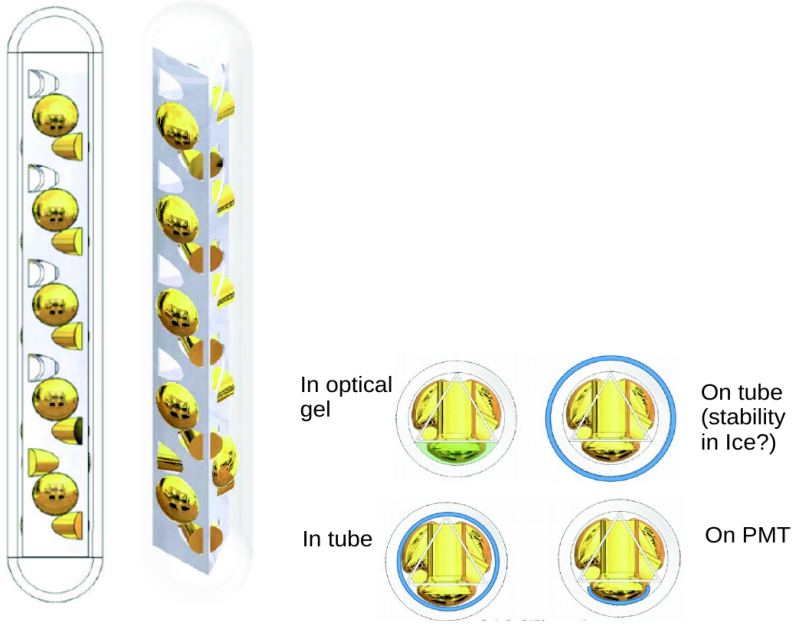

Figure 3.8: (left) Basic sketch of a LOM with the upper four right-facing PMTs removed. (right) Top view with different considered placements for wavelength-shifter or wavelength-shifter-paint. Images taken from [76]

The LOM is a hybrid between WOM and mDOM, it uses multiple PMTs facing in different directions. This way it has similar capabilities than the mDOM as shown in fig. 3.8 (left). It uses a slim and elongated pressure-vessel like the WOM with a slightly larger diameter to fit the PMTs inside. The application of wavelength-shifter at different locations are considered as shown in fig. 3.8 (right). This module is in its early stages of development and not all design decisions are final yet. The LOM thus combines many advantages of WOM and mDOM with the potential to save costs while making use of directional reconstruction and additional photons from the UV-range due to the use of a wavelength-shifter. Since this module is in the early prototyping phase there is currently limited information available.[2]

3.2.6 Fiber Optical Module (FOM)

The FOM is an array of wavelength-shifting fibers bound together every few meters to read out the ends with small PMTs as shown in fig. 3.9. This concept allows for direct contact between the ice and the light guide. A pressure-vessel is not required and thus there is no gap between pressure-vessel and wavelength-shifting tube as there is in the WOM. This setup potentially allows it to capture more of the photons reaching the sensor. At the same time, it would have an even larger sensitive area and a lower price. The downside here is that this is untested technology and there are significant risks for the fibers to be broken or bent during deployment or freezing in a way that makes photon detection or at least a sufficient calibration hard to obtain. Since this module is in the early prototyping phase there is currently limited information available.[3]

[2] For further information please contact the IceCube collaboration.
[3] See footnote 2.

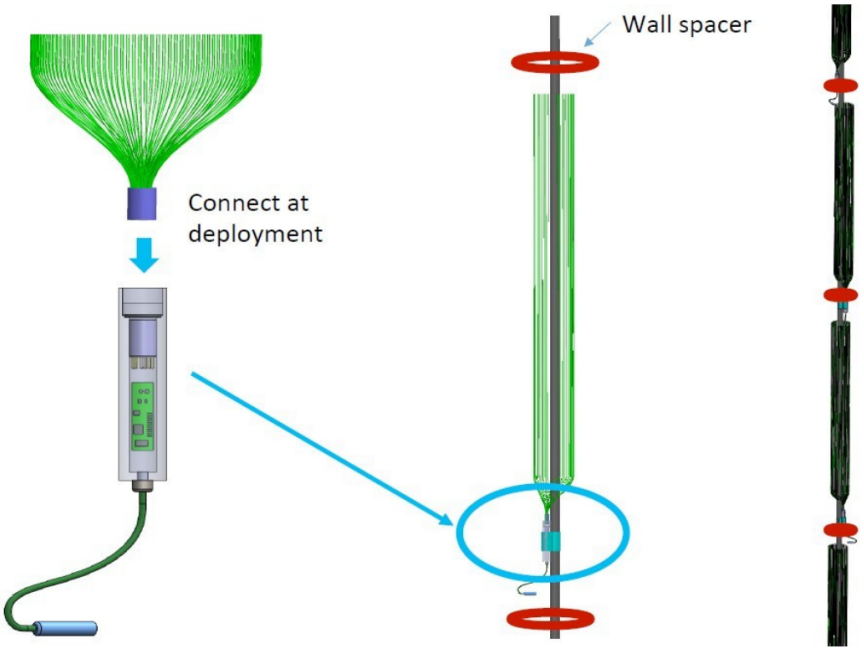

Figure 3.9: The basic concept of the FOM and its drill hole deployment configuration. Image taken from [76]

3.2.7 Precision Optical Calibration Module (POCAM)

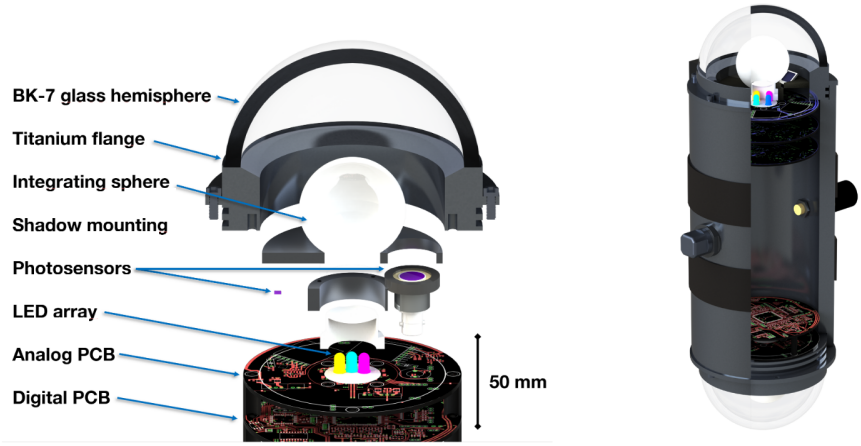

Figure 3.10: Illustration of the POCAM with a hemisphere assembly (left) and complete module assembly (right). Image taken from [77]

For IceCube events, the accuracy of reconstructions is often limited by the quality of the calibration. The most difficult parameters to understand and calibrate for are the optical properties of the ice. To improve this for IceCube-Gen2 as well as retrospectively for IceCube the POCAM has been developed [77]. An image is shown in fig. 3.10. The POCAM is a self-calibrating isotropic, nanosecond-pulsed, multi-wavelength calibration light source that allows for adjustments in pulse intensity and duration.

The isotropy is obtained by using a semi-transparent PTFE[4] integrating sphere. Integrated photosensors allow for self-calibration. It is planned to deploy several PCAMs in IceCube Upgrade. First tests with prototypes have been performed within the GVD telescope in Lake Baikal.

[4] Polytetrafluoroethylene is also known as Teflon.

CHAPTER 4

The Wavelength-shifting Optical Module (WOM)

In this chapter, the concept, components, and basic properties of the Wavelength-shifting Optical Module (WOM) are introduced. A description of the underlying physics for each of the components is given as needed. All developments presented in the following chapters will be based on the design and concepts noted below.

4.1 Concept

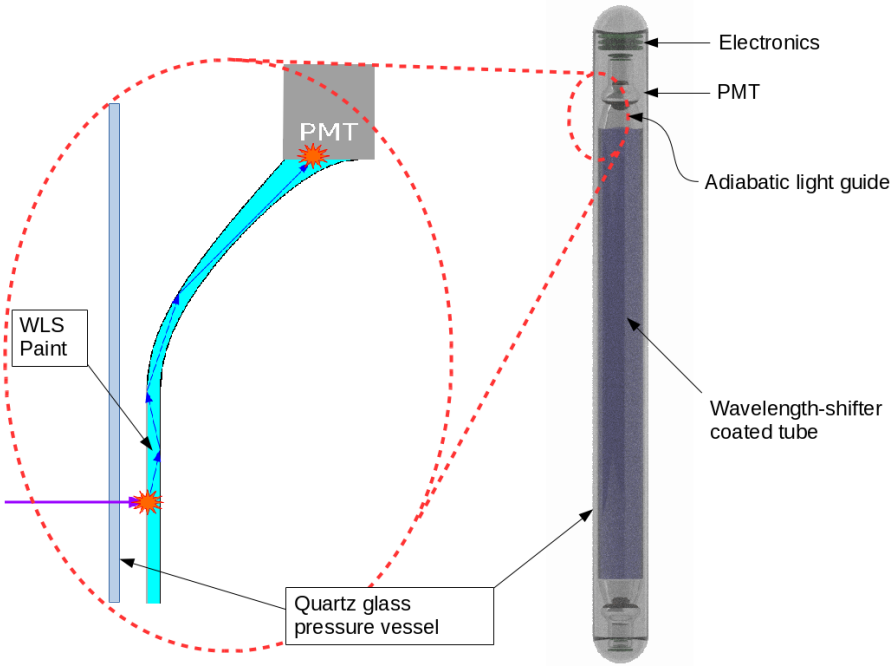

Figure 4.1: Illustration of the WOM components and its basic functions. The image is based on works of [78] and [74].

Fig. 4.1 shows on its right a digital visualisation of a full WOM. For illustrative purposes, the holding structures within the pressure vessel on the top and bottom are omitted.
Unique to the WOM is the wavelength-shifter (WLS) coated tube responsible for capturing the photons

and guiding them towards the PMTs on the ends. To allow the use of small PMTs with low dark noise, adiabatic light guides[1] are used as an adapter at each end. Each adiabatic light-guide is connected to a PMT. Both PMTs have an electronic readout board. The main OM electronics are hosted in the top of the module above the upper PMT. The lower PMT is connected to the mainboard via cables that are fed through the center of the WLS tube. This entire module is placed in a quartz glass pressure vessel.

The left side of fig. 4.1 illustrates the detection principle. A UV photon on a path towards the OM is shown as a purple arrow coming from the ice with a refractive index of about 1.33 as it enters the pressure vessel. The pressure vessel itself has a refractive index of about 1.5 and thus the probability of reflection is small in comparison. When leaving the glass of the pressure vessel towards the interior the refractive index drops to 1 due to a small air/vacuum gap. At this point the probability for reflection is higher, especially for photons coming from steep angles to be reflected back into the ice. Assuming the photon passes through as illustrated and hits the surface of the WLS tube, it will likely enter the thin layer of WLS paint on the surface of the coated tube. The WLS concentration is designed to virtually ensure photon absorption. Within $O(1)$ ns the excited WLS molecule deexcites and emits a lower wavelength photon in the blue part of the optical spectrum, as illustrated with the orange glow. The reemission of the photon is isotropic within the medium of the refractive index 1.5 and thus theoretically about 75 % of the photons can be captured by total internal reflection (TIR). The reemitted and captured light is transported by TIR towards one of the sides of the tube, as indicated by the blue arrows. The adiabatic light guide theoretically losslessly directs the light towards the center. Here it can be detected by a PMT which is coupled optically to the adiabatic light guide. The PMT can detect the photon and is read out by the electronics of the module, where the signal is processed for further use.

4.2 Motivation

The original motivation for the design of the WOM was the detection of extragalactic core-collapse (CC) supernova (SN) [80]. IceCube is currently able to detect and notify other experiments about galactic core-collapse SN. Neutrinos from these SN usually have energies of $\approx 10\,\mathrm{MeV}$ [81] and thus do not exceed the detection threshold of about $10 - 100\,\mathrm{GeV}$ for IceCube. However, they are so numerous that they can significantly increase the noise level in the detector as a whole for a short period of time and thus allow a detection. CC SN in the Milky Way are rare. To increase the detection frequency of these SN an increase in the search volume beyond the Milky Way to neighbouring galaxies is the only option. With the increased distance between Earth and these SN events in neighbouring galaxies, the number of neutrinos reaching Earth decreases below the current detection threshold of IceCube. The possible signal is indistinguishable from the ambient noise which must be reduced to detect the signal. A large fraction of ambient noise is caused by thermionic emission of electrons from the photocathode of the PMT [82]. This kind of noise is proportional to the total photocathode area and cannot be reduced by a simple upscaling of the experiment. The WOM increases the photosensitive area with the WLS tube while decreasing the photocathode area. This feature is still unique to the WOM.[2] Compared to the DOM, the WOM has several other advantages with few disadvantages.

On the advantageous side, there is a low noise rate. Additionally, the WOM has a high UV sensitivity which allows it to profit from the λ^{-2} behaviour of the Cherenkov spectrum. Combined with the large

[1] Theoretically lossless light concentrators developed in [79]. Though latest simulations and measurements show suboptimal light concentration.

[2] And possibly the FOM.

photosensitive area the WOM becomes a calorimetric detector. Aside from the beneficial physics properties, the WOM also allows for cost reduction. The costs of the WOM components are lower than most[3] other proposed modules [74]. This is due to the small low-cost PMTs that make up most of the costs in other modules. Furthermore, the smaller diameter of the WOM as compared to the pDOM, D-Egg, or mDOM decreases the drilling cost for the ice holes significantly.
The downsides for the WOM are mostly defined by the loss in time resolution due to the WLS and the light propagation in the tube. The pressure vessel for the WOM is more expensive than those used for other modules since it is more expensive but UV transparent quartz glass is used as opposed to borosilicate glass. In comparison to the mDOM and D-Egg, there is no directional resolution when only one WOM per string position is used. However, due to the small diameter of the WOM, deployment of 3 WOMs per string position as a single module is feasible while still saving on drilling and module costs relative to the sensitive area [74].

This means, when it can be shown that the decrease in timing resolution has little to no effects on reconstruction accuracy the WOM will increase performance and reduce costs for the detector while simultaneously enabling extra-galactic CC SN detection. However, for this to be accomplished the properties of the WOM and our understanding of them need to be improved.

4.3 Components

In this section, the individual components of the WOM will be introduced. Specifically, the pressure vessel, WLS paint, WLS tube, adiabatic light guide, and PMT will be addressed. Previously obtained results will be presented alongside.

4.3.1 Pressure Vessel

To increase the sensitivity for the UV photons in the Cherenkov spectrum the pressure vessel needs to be transparent to these wavelengths. In previous OMs borosilicate was used as a material for the pressure vessel. Since borosilicate has limited UV transparency, quartz glass has been chosen as a good candidate material for the WOM pressure vessel. A comparison of the transparencies between both materials can be seen in fig. 4.2. For the measurement, two prototype end caps for the WOM have been used. The thickness of the borosilicate was 8 mm and 9.5 mm for the quartz glass. The measurement shows the ratio of light passing from a lamp to a spectrograph, with and without end cap in the light path. The Fresnel corrections to account for reflection have been applied. The reason the relative intensity exceeds the theoretical maximum of 1 can be explained by the focusing effect of the end caps curvature. Yet it can be seen that the UV transparency of quartz glass exceeds that of borosilicate. Due to superior transmission properties, quartz glass are used for the first prototypes. Since quartz glass has a higher price than borosilicate, it remains to be seen which material delivers a higher photon per money ratio for deployment.

On a prototype pressure vessel, the ability to hold a vacuum over several months has been successfully tested as well as pressure tests of up to 5250 psi ($\approx$ 360 bar). Tests with higher pressures are planned for the future.

[3] Except the FOM

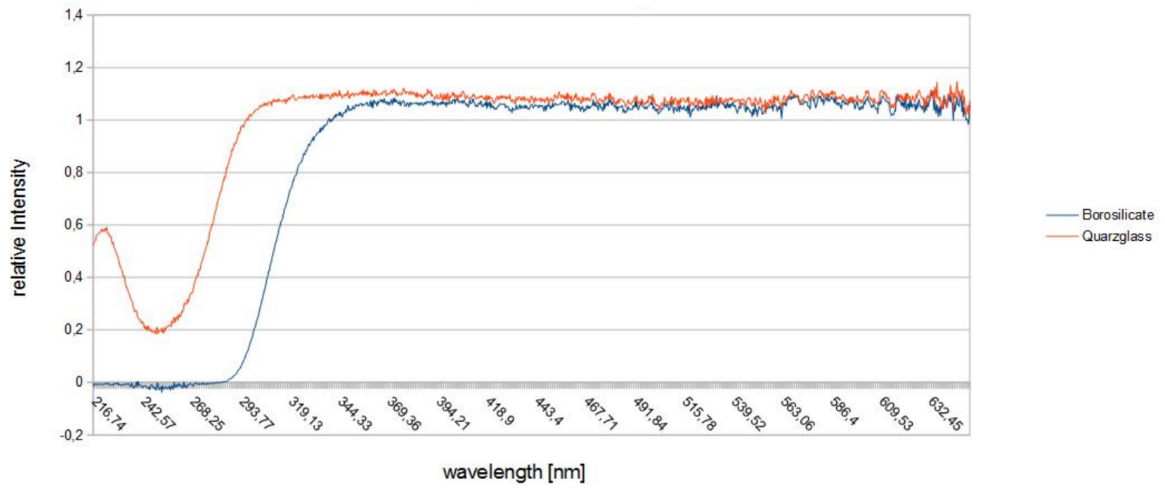

Figure 4.2: Comparison of wavelength-dependent transparency between borosilicate and quartz glass. Taken on a 8 mm thick end cap of a pressure vessel for borosilicate and a 9.5 mm end cap for quartz glass. The measurement and the plot were produced by [83].

4.3.2 Efficiency Enhancement by Refractive Index Matching

As previously mentioned the transition from the outside to the inside of the WOM causes some losses. The air gap between pressure vessel and PMMA tube is particularly responsible for significant losses due to reflection on the glass to air interface at large photon incident angles. For maximum efficiency, a high refractive WLS material directly deployed in ice would be needed. This approach is taken by the FOM but is otherwise difficult to accomplish for WOM-like OMs. However, when looking at the transition `outside` → `quartz glass` → `gap` → `PMMA tube and WLS` it might be possible to fill the `gap` with a material other than air or vacuum to achieve a higher ϵ_{comb}. In fig. 4.3 the total theoretical capture efficiency of the WOM ϵ_{comb}[4] is calculated as a function of the refractive index n_{fill} of the `gap` material, for the `outside` materials water/ice and air. The calculations are based on Snell's law and the Fresnel equations with the refractive indexes taken from [84] at 589.29 nm. It was assumed the refractive index of the PMMA and the WLS paint is identical to that of quartz glass. It became clear that a `gap` material with a refractive index slightly above that of the `outside` material maximizes the capture efficiency. For the WOM the `outside` material is ice and the best n_{fill} is 1.34 [85]. A material such as perfluorohexane ($n = 1.25$)[5] mixture, oils or alcohols are possible candidates. No further investigation into these materials has been done yet. Therefore the calculations in this thesis are done with air as a fill material, but in theory, a good matching can increase the total module efficiency by more than 50 %.

4.3.3 Wavelength-Shifting Paint

The wavelength-shifter (WLS) paint was previously developed in [86] during which the first measurements of its basic properties were taken. The spectral behaviour has been shown to match the requirements of the WOM.

[4] Assuming all other components work at their theoretical optimum and the PMT has 100% photon capture efficiency.
[5] At room temperature

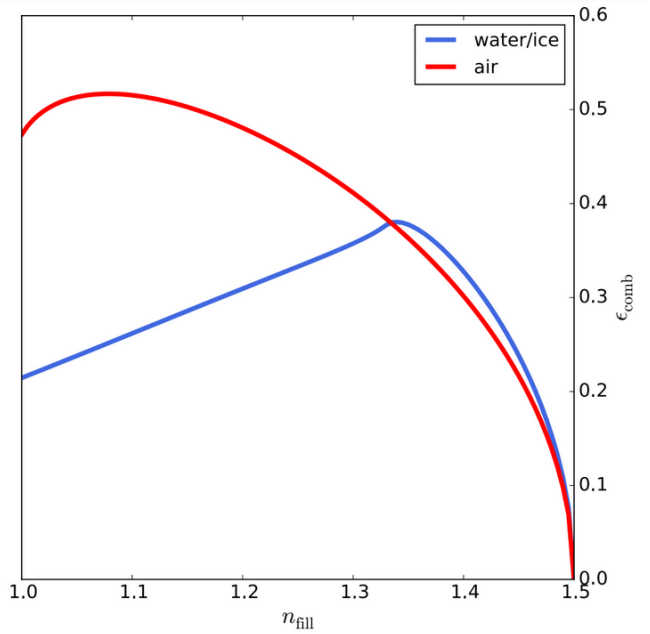

Figure 4.3: Total theoretical photon capture efficiency of the WOM ϵ_{comb} for water/ice and air as the ambient medium as a function of the refractive index n_{fill} of the material between pressure vessel and WLS tube. This plot was created by [85].

Wavelength-shifter

A wavelength-shifter (WLS) is a photo-fluorescent molecule that absorbs photons of a certain energy range and emits one or more lower-energy photons as a result. The efficiency with which a WLS can do this is the quantum yield (QY) as shown in eq. 4.1. It is an intrinsic property and not to be confused with the quantum efficiency (QE) in eq. 4.2 that depends on the specific use eg. the used solvent. The relaxation or decay time of the excited molecule is usually in the order of nanoseconds and the re-emission direction is arbitrary. There are many different types of WLS available today, organic and inorganic. The WLS used in this thesis are all organic and the wavelength-shifting process is facilitated, as with most organic WLS, by one or more benzene rings. The combination of σ_s and σ_p bonds in benzene rings facilitates the absorption and emission processes. These molecules are mostly planar and thus stack well. Stacking allows non-radiative energy transfer and reduces the quantum efficiency (QE). Alternative WLS with aggregation-induced emission that have a 3-dimensional structure do exist but generally obtain a lower QE. Therefore a sufficient separation of the molecules and high optical densities are key to obtaining a high QE. The WLS used in this thesis are p-terphenyl (PT) with a QY> 80 % [87] and Bis-MSB with a QY of 0.926 ± 0.053 [88] or 98 % [89] or 96 % [90] depending on the source. A more detailed description of the underlying physics can be found in the previous work on the WOM [86]. Additional information on the construction of WLS can be found at [91].

$$\text{QY} = \frac{\text{\# emitted photons}}{\text{\# absorbed photons}} \tag{4.1}$$

$$\text{QE} = \frac{\text{\# reemitted photons}}{\text{\# incident photons}} \tag{4.2}$$

Paint

The paint in most contexts is a liquid composed of a binder, a thinner, and a pigment. The thinner e.g. solvent dissolves the binder and sometimes the pigment as well. When a paint is applied to a substrate the thinner evaporates and the binder with the pigment remains as a thin solid layer. In the application here the pigment is the WLS. The binder does not just hold the WLS in place but also separates the WLS molecules to avoid crystallisation and maximises quantum efficiency. The effect of solvent evaporation on the optical surface quality so far could not be separated from other light loss mechanisms. Commercial glossy paints are often made from two components to obtain the best surface quality. Since the pigment here also needs to be dissolved this currently seems infeasible for this application.

Application for the WOM

The WLS paint used for the WOM was developed in a prior thesis [86]. Key findings were the current best paint mixture, its emission and absorption behaviour as well as an approximation of the quantum efficiency (QE). Furthermore, a dip-coating process was developed to apply the paint to the light-guiding tube.

The current best mixture consists of Bis-MSB (0.13 %), p-Terphenyl (0.27 %), toluene (77.31 %), and Paraloid B72 (22.29 %).[6] Toluene is a good choice as thinner, since it dissolves Paraloid B72 and WLS well but is not very aggressive on PMMA, the material the tube is made of. Still, it dissolves PMMA slightly and thus creates a good bond between paint and tube.[7] Bis-MSB and p-Terphenyl (PT) are the WLS pigments. PT shifts photons from $\approx 280 - 330\,\text{nm}$ to $\approx 345\,\text{nm}$. The corresponding absorption and emission spectra for PT can be seen in fig. 4.4 (left). Due to insufficient light intensity below $\approx 280\,\text{nm}$, measurements in that region are not reliable any more. The large error of the emission spectrum is a consequence of the spectrograph used. Due to the aforementioned large error on the emission spectrum, which is required to determine an efficiency spectrum, only an absorption spectrum for PT is shown.[8] For Bis-MSB an efficiency and an emission spectrum are shown in fig. 4.4 (right). It shows that Bis-MSB shifts photons from $280 - 300\,\text{nm}$ to $\approx 420\,\text{nm}$ while there is a slight decline in efficiency at lower wavelengths. The efficiency spectrum was taken on a 30 cm long 2 cm diameter PMMA tube with a photodiode (PD). Since it is currently not possible to accurately derive the absolute number of photons from the PD measurement only a lower limit is given for the efficiency.[9] The same measurement for the combination of both WLS is shown in fig. 4.5. The addition of PT compensates the deficiency of Bis-MSB at lower wavelengths. The emission spectrum for the mixture is the same as Bis-MSB since the emission from PT is reabsorbed by the Bis-MSB. The efficiency spectrum in fig. 4.5 drops off at about $\approx 395\,\text{nm}$, and earlier than the $\approx 400\,\text{nm}$ in fig. 4.4 (right). This was caused by a switch of binder from PMMA to Paraloid B72.

To apply the paint on the light-guiding tube, it is immersed in paint and withdrawn at a well-defined velocity from the paint. The immersion duration and withdrawal velocity allow one to control the paint thickness. The optimal values depend on the used materials and had to be re-evaluated in this thesis.

[6] By weight

[7] Recent measurements show that more PMMA is dissolved than previously assumed. Thus the immersion duration might have a strong influence on the paint thickness and the tube's light capture efficiency.

[8] For completeness an efficiency measurement is plotted in fig. A.8.

[9] This is due to total internal reflection in the glass cover of the PD. This will be addressed with more depth in the next chapter.

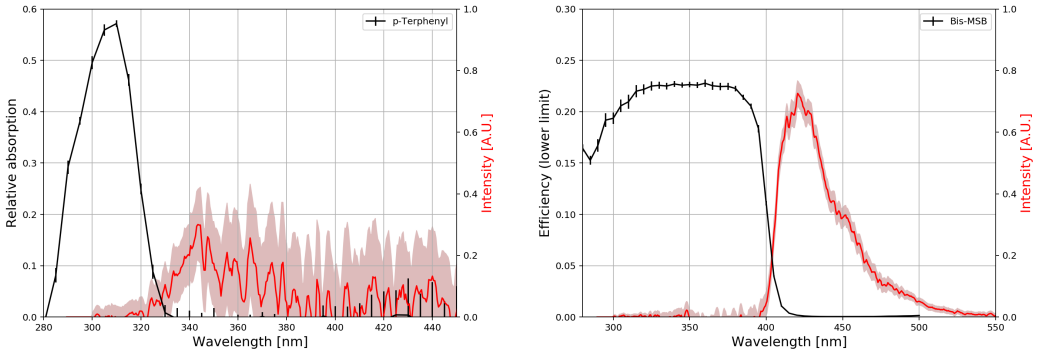

Figure 4.4: (left) p-Terphenyl absorption and emission spectrum. (right) Bis-MSB light capture efficiency and emission spectrum. The data for these plots was taken from [86].

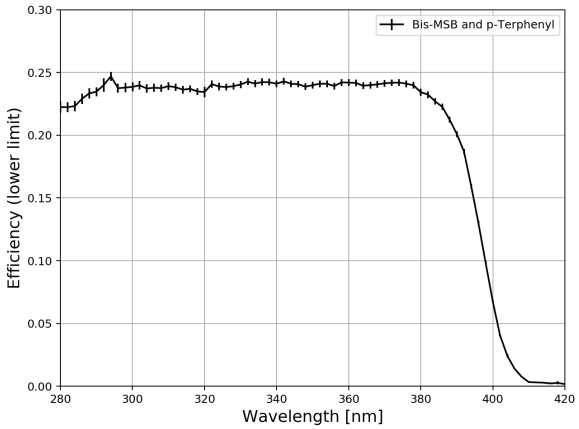

Figure 4.5: Light capture efficiency for a paint consistent of Bis-MSB, p-Terphenyl, toluene, and Paraloid B72. Taken on a 30 cm long 2 cm diameter PMMA tube with a photodiode (PD). The data for this plot was taken from [86].

4.3.4 Light Propagation Concepts and Components

This section gives an overview of the different light propagation concepts and components used by the WOM. Specifically, total internal reflection in the WLS tube and the adiabatic light guide is discussed.

Total Internal Reflection

Total internal reflection (TIR) is a concept that is essential to the working principle of the WOM; it is a direct consequence of Snell's law as stated in eq. 4.3.

$$\frac{\sin\theta_2}{\sin\theta_1} = \frac{n_1}{n_2} \tag{4.3}$$

1 and 2 refer to different materials with different refractive indexes n_i and the angle θ_i of a photon relative to the surface normal between both materials. When light propagates in material n_2 with a

higher refractive index than the surrounding material n_1 ($n_1 < n_2$), there is an angle θ_c under which eq. 4.3 does not have a real solution for the outgoing angle θ_1 and the light can not leave the medium. This angle θ_c is called the critical angle and can be calculated according to eq. 4.4. The photons with θ_c or larger angles will be reflected back into material 2 under the same angle they arrived at. These photons are totally reflected. With an appropriate shape of material 2, recurrent TIR can be achieved for photon capture and/or transport over long distances as is done in optical fibers.

$$\theta_c = \arcsin\left(\frac{n_1}{n_2}\right) \tag{4.4}$$

The WLS Tube

The WOM uses TIR to capture and transport light to the ends of the WLS tube. The wavelength shifting paint has a comparable refractive index to the PMMA of the tube. The paint is applied as an outer layer with $O(10\,\mu\text{m})$ thickness [86]. The WLS molecules can be assumed as isotropic emitters within the paint layer. Since the paint layer thickness is much smaller than the tube radius, the outer tube surface can be approximated as flat for the WLS. Therefore if the first reflection occurs on the outside of the tube the reflection probability can be approximated by a flat surface. Assuming a rod with a cross-section is shown in fig. 4.6 instead of a tube, it can be seen that once a photon is reflected on the inside of the rod, it will continuously be reflected under the same angle. Optical fibers operate based on this principle.

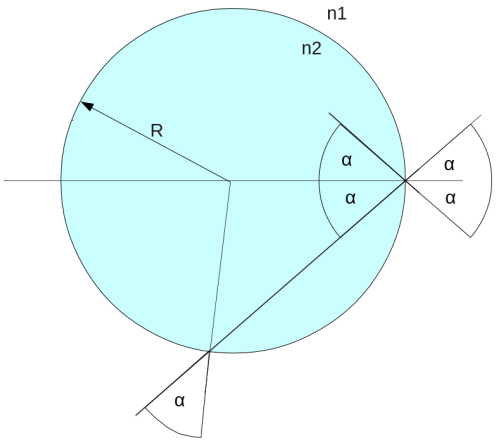

Figure 4.6: Illustration of perpetual light reflection in the cross-section of a high refractive index ($n_2 > n_1$) rod. Taken from [86].

In the next step, a tube instead of a rod is considered. From Snell's law, it follows that any light leaving the tube material towards the inside has to re-enter the tube under the same angle[10] and thus the above arguments from fig. 4.6 apply again. However, as mentioned earlier cable and possibly other installations will run through the center of the tube. Therefore, light must only be transported in the wall and not the center of the tube. From simple geometric considerations shown in fig. 4.7 (left), it can be seen that due to the curvature of the tube the reflection on the inner wall will always occur at an identical or steeper angle than the one on the outer wall ($\alpha \geq \beta$). Since a steeper angle has an equal or higher probability for reflection and the incoming angle always equals outgoing angle the simplification

[10] For infinitely long tubes.

of fig. 4.6 can be used again. In combination with the assumption that the photon is emitted at or very close to the outer surface, the capture efficiency of a tube can be calculated from a flat plate as illustrated in fig. 4.7 (right). The solid angle Ω in the figure can be calculated according to eq. 4.5. To obtain the fraction of light captured, the second cone is accounted for, the function normalized and the critical angle is calculated from eq. 4.3 and inserted for ω, resulting in eq. 4.6. For PMMA ($n_2 \approx 1.5$) and air ($n_1 \approx 1$) the capture efficiency was calculated to be 74.5 %.

$$\Omega = 4\pi \sin^2\left(\frac{\omega}{4}\right) \tag{4.5}$$

$$\epsilon_{\text{captured}} = 1 - 2\sin^2\left(\frac{\arcsin\left(\frac{n_1}{n_2}\right)}{2}\right) = \cos\left(\arcsin\left(\frac{n_1}{n_2}\right)\right) \tag{4.6}$$

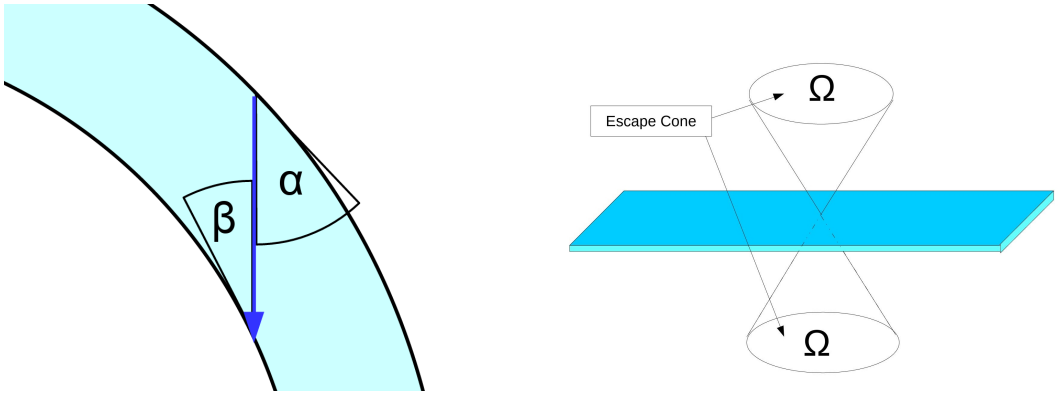

Figure 4.7: (left) Illustration of reflection angle relations in a tube for the inner and outer surface. (right) Illustration of non captured light in form of solid angle light cones, taken from [86].

Adiabatic Light Guide

In order to use the largest diameter PMMA tube that fits the pressure vessel while using the smallest possible PMT, an adiabatic light guide was designed. It redirects the light from the tube to the PMT and is another application of TIR in the WOM. Its shape was previously calculated [79]. Two independent techniques based on skew invariance and étendue conservation have been used to calculate the optimal shape. Both approaches agreed with one another. The resulting shape is shown in fig. 4.8 on the left as well as a prototype on the right. Several light guides have been produced in the local workshop and externally at Kümpel Kunststoff-Verarbeitungswerk GmbH. During this thesis, some initial tests concerning the light guide and its attachment to the PMMA tube were completed. However, the results were not conclusive. A description of the gluing approaches can be found in chapter A.4.4. Further studies are needed to determine and maximize overall performance. Therefore all calculations done in this thesis exclude this component for the time being and assume 100 % transport efficiency. It should be noted that the latest simulations at Mainz University showed that losses were kept to a minimum but a large fraction of light entering the light guide is reflected back into the WLS tube. The reason for the back reflection appears to be directly linked to the shape of the adiabatic light guide.

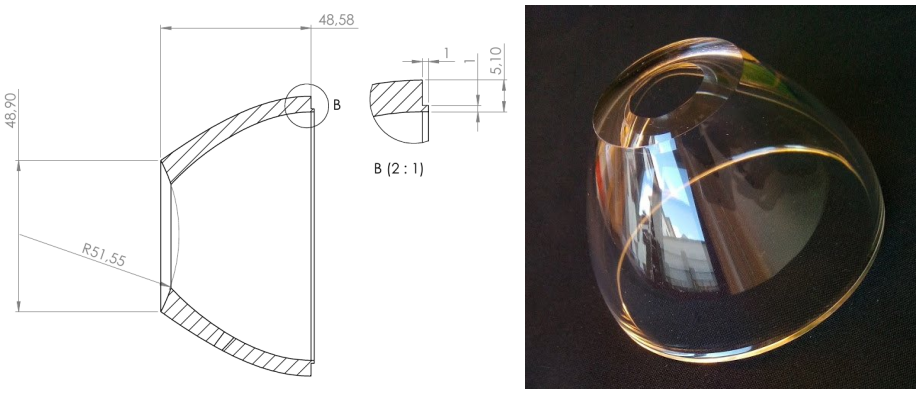

Figure 4.8: (left) Technical drawing of an adiabatic light guide created by the staff at DESY based on the work in [79]. (right) Picture of the first adiabatic light guide prototype made by Kümpel Kunststoff-Verarbeitungswerk GmbH.

4.3.5 Photo Multiplier Tubes

Photomultiplier tubes or PMTs are light detection devices based on the photoelectric effect. They are capable of detecting low-intensity light down to single photons and produce a proportional charge output with gains in the range of 10 to 10^7 [92][93]. In fig. 4.9 the process of photon detection is depicted. The main body of the PMT usually consists of a glass vacuum vessel with metallic connectors on the back end. The inside of the front end of the vacuum vessel is vacuum metalized[11]. The center of the glass body houses a dynode structure. For photon-detection, light impacts the front side with the metal deposits. The photons need to traverse the glass vessel until hitting the vacuum-metalized inner surface. Given sufficient energy, it removes an election via the photoelectric effect. During operation a high voltage is applied between the vacuum metalized layer or cathode and the first dynode. The electrical fields accelerate the free electron. To direct the electrons towards the first dynode a focusing electrode between the first dynode and the cathode is often used. Upon impact with the first dynode, additional low energy electrons are emitted. Each consecutive dynode has a higher positive voltage applied to it so the process is repeated for each new electron until the anode is hit with a large number of electrons. At the anode, the charge is large enough that a signal can be read out by an electronics setup.

For the WOM it is currently planned to use the Hamamatsu R12199-02. This PMT will also be used for the mDOM, in that context it has already been investigated thoroughly [73][95]. According to the manufacturer, it is rated with a typical peak quantum efficiency of 26 % at 420 nm, photocathode area with a 72 mm diameter, wavelength range from $300 - 650$ nm and a gain of 5×10^6 for the bialkali version [96][97]. In addition, a super bialkali version has recently become available which could further increase the efficiency of the WOM.

To determine the noise behaviour at low temperatures the WOM group at Mainz University did some dedicated measurements as shown in fig. 4.10 (left). At relevant temperatures, the noise level is about $50\,\mathrm{s}^{-1}$. To determine possible asymmetries, a photocathode scan shown in fig. 4.10 (right) was performed. Clearly visible is a gradient from the top right to the bottom left with a difference between

[11] A process that deposits a thin layer of metal on a substrate by heating metal in a vacuum.

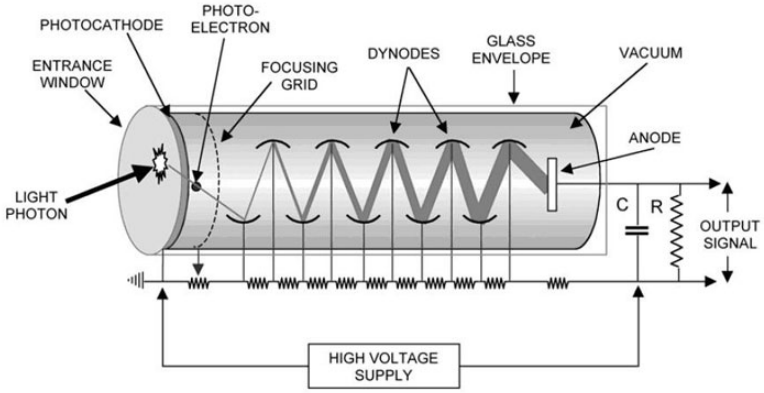

Figure 4.9: Illustration of the structure and working concept of a PMT. The picture was taken from [94]

the two of about 20 %. This is caused by the orientation of the first dynode.[12] For different positions on the cathode the impact angle of the photoelectrons on the first dynode changes and therefore so does the detection probability. Every PMT expresses this behaviour in a more or less pronounced form. It is an important systematic effect to consider in this thesis since often different parts of the PMT are illuminated for signal and reference measurements.

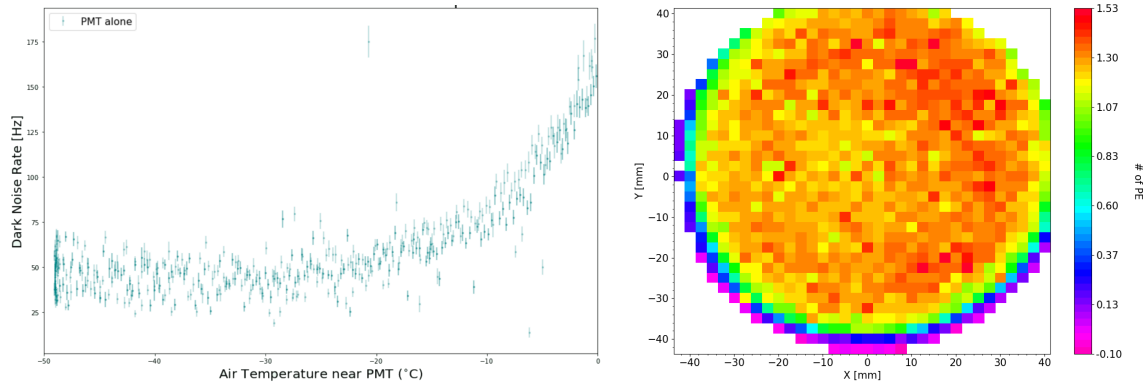

Figure 4.10: (left) Noise rates of the Hamamatsu R12199-02 measured and plotted by [98]. (right) Relative photon sensitivity of the Hamamatsu R12199-02 as a function of position measured and plotted by [99]. Absolute intensity of the light source was not measured. Illumination perpendicular to the curved surface. The first dynode faces $\approx 190^{\circ}$.

Due to the Hamamatsu R12199's curved surface and limited size, it was necessary to use other PMTs during the measurements in this thesis as well as other photosensitive devices such as photodiodes. The specific model used will be named in the individual measurement descriptions.

[12] Facing $\approx 190^{\circ}$, based on a coordinate system with the reference direction from the pole to the horizontal right and counterclockwise increase in degree.

4.4 The Combined Module

When all the components are combined the module properties can be determined, most importantly the combined efficiency ϵ_{comb} and expected noise rate.

4.4.1 Efficiency

The total efficiency ϵ_{comb} is the product of all individual efficiencies as described by eq. 4.7.

$$\epsilon_{\text{comb}} = \epsilon_{\text{PMT}} \cdot \epsilon_{\text{ALG}} \cdot \epsilon_{\text{Tube}} \cdot \epsilon_{\text{WLS}} \cdot \epsilon_{\text{Capture}} \cdot \epsilon_{\text{Glass}} \tag{4.7}$$

ϵ_{PMT} is a scalar determined from the wavelength-dependent PMT sensitivity $R_{\text{PMT}}(\lambda)$ and the normalized WLS emission spectrum $S_{\text{WLS}}(\lambda)$ as defined in eq. 4.8. It describes the probability of an average photon emitted by the WLS to be detected by the PMT.

$$\epsilon_{\text{PMT}} = \int S_{WLS}(\lambda) \cdot R_{\text{PMT}}(\lambda) d\lambda \tag{4.8}$$

ϵ_{ALG} is the transport efficiency of the Adiabatic Light Guide (ALG). It represents the ratio of the number of photons coming out of the smaller end to the number of photons going into the wider end. Since the ALG was not the focus of this thesis ϵ_{ALG} is assumed to be one if not specified otherwise.

ϵ_{Tube} is the photon transport efficiency within the tube. It determines how many photons reach either end of the tube after being geometrically captured for all possible photon paths. ϵ_{Tube} cannot be analytically calculated, only simulated or measured. It depends on the absorption and scattering probability of the photons in the tube. If not specified otherwise it is averaged over the whole length of the tube.

ϵ_{WLS} is the wavelength-shifter efficiency. It is the product of the photon absorption probability $\epsilon_{\text{WLSabs}}(\lambda)$ and the WLS quantum efficiency QE. The photon absorption probability $\epsilon_{\text{WLSabs}}(\lambda)$ is defined by the optical density of the WLS and the WLS quantum efficiency QY (the number of photons emitted per absorbed photon). The former can be varied with the paint thickness and the latter was previously estimated to be close to unity [86].

$\epsilon_{\text{Capture}}$ is the capture efficiency. It is the product of the geometric capture efficiency of the tube $\epsilon_{\text{CaptureGeo}}$ and the refractive capture efficiency $\epsilon_{\text{CaptureRef}}$. The geometric capture efficiency $\epsilon_{\text{CaptureGeo}}$ should be the theoretical value 74.5 %. The refractive capture efficiency $\epsilon_{\text{CaptureRef}}$ depends on n_{fill} as shown in fig. 4.3. For the calculations in this thesis $n_{\text{fill}} = 1$ is assumed, so a gain of > 1.5 for all ϵ obtained is feasible.

ϵ_{Glass} is the probability as a function of wavelength λ for a photon to pass through the glass of the pressure vessel. For most wavelengths relevant to the WLS it can be assumed to be one.

The WLS tube is the novel component in this design and therefore will have special attention in this thesis. Measurements on the tube combine several of the parameters. They are represented by ϵ_{Wt} as stated in eq. 4.9 and 4.10.

$$\epsilon_{\text{Wt}} = \epsilon_{\text{WLS}}(\lambda) \cdot \epsilon_{\text{CaptureGeo}} \cdot \epsilon_{\text{Tube}}(d) \tag{4.9}$$

$$\epsilon_{\text{Wt}} = \frac{N_{\text{out}}(\lambda, d)}{N_{\text{in}}(\lambda)} \tag{4.10}$$

4.4.2 Noise

As a unique selling point of the WOM, the noise rate has to be determined as a whole since each component might bring additional radioactive impurities increasing the noise of the bare PMT. The noise of the bare PMT was previously shown in fig. 4.10 (left). In fig. 4.11 the other main components are measured. First, the end cap is placed directly in front of the PMT. The mean noise rate between -20 and $-50\,^{\circ}\mathrm{C}$ increases to $153\,\mathrm{s}^{-1}$, showing that the Borosilicate end cap has significant radioactive impurities. Placing the end cap behind the PMT reduces the mean noise rate to $47\,\mathrm{s}^{-1}$, showing that the impurities have almost no contribution at the final position of the end cap. Adding the adiabatic light guide and a wavelength-shifting tube increases the noise rate to $72\,\mathrm{s}^{-1}$. Considering that the wavelength-shifter is also a scintillator which could pick up ambient radiation and cosmic rays, this noise rate is rather low. Adding the quartz glass pressure vessel increases the average noise rate to $630\,\mathrm{s}^{-1}$. This is much higher than the desired noise rate of $< 100\,\mathrm{s}^{-1}$. Further investigation showed a $\approx 150\,\mathrm{ppm}$ $^{238}\mathrm{U}$ contamination[100]. Contacting other suppliers proved quartz glass with a much lower concentration of radioactive elements can be bought in various optical qualities and prices, making additional noise smaller than $10\,\mathrm{s}^{-1}$ possible [100]. These values are only theoretical so far.

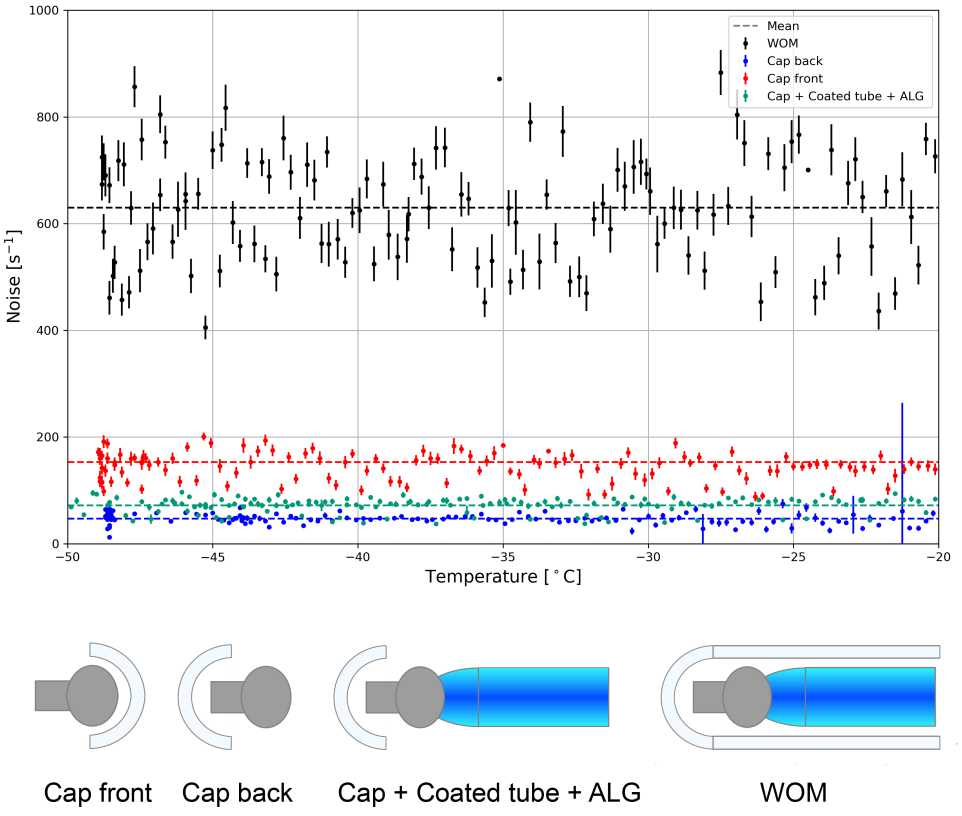

Figure 4.11: Noise rates for different parts and constellations at relevant temperatures. Based on data from [98].

CHAPTER 5

Physical Characterisation of the WOM

This chapter takes a closer look at the most important performance parameters of the WOM, with a specific focus on the wavelength-shifting and light-guiding tube. It starts with the results obtained in [86] and shows the progress in understanding and improving the WOM performance. This is followed by a general discussion of systematic errors for the measurements presented.

5.1 Previous Results

In the previous work [86], the measurement of ϵ_{Wt} was a key component. More detailed evaluation, however, showed that these results contain a systematic error that is not accounted for. This section presents how the measurements were performed, what the results were, how the systematic error was discovered, and what effect it has on the previous conclusions.

5.1.1 The Measurement Setup

To determine the WLS tube efficiency ϵ_{Wt}, the setup shown in fig. 5.1 has been used. It is comprised of a high-pressure xenon arc lamp, a monochromator [101], two PDs [102], two lock-in amplifiers[1] and several optical components. The monochromator is a tunable bandpass filter[2] for the broad spectrum of the xenon lamp. The different wavelengths are spatially separated with a reflective grating and, thereafter, the desired wavelength is cut from the spectrum with an aperture stop. As shown in the figure, the outgoing light is periodically blocked with a chopper wheel. Whereafter it is split between a reference PD (to correct for intensity fluctuations of the light source) and a test beam. For measurements, the optical sample is introduced in the test beam. All optical components are shown in fig. 5.1. The chopping[3] is necessary for the lock-in amplifiers to work and suppress the ambient light as well as other noise.

5.1.2 Data Evaluation

For an accurate measurement, both a measurement (M) as well as a calibration measurement (CM) is required. The measurement setup is depicted in fig. 5.1. For the calibration measurement, the coated sample is taken out and the light guide is directly pointed on the signal PD. Starting from the original

[1] Stanford Research Systems SR830 [103]
[2] FWHM $\approx$ 3 nm.
[3] Periodically blocking the light beam with a chopper wheel. Also see fig. 5.1.

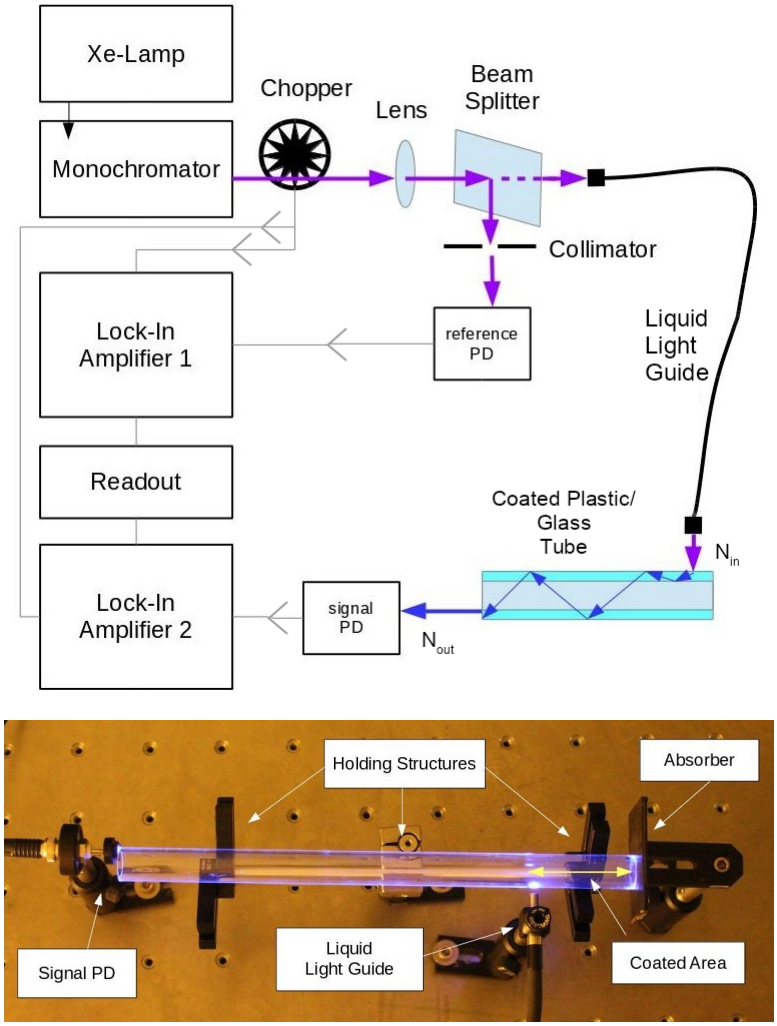

Figure 5.1: (up) Illustration of the PD based measurement setup used to measure the data in fig. 4.5. (down) Picture of a PMMA tube sample in the measurement setup. Images were taken and modified from [86].

definition of the efficiency $\epsilon_{\mathrm{Wt}}(\lambda)$ as stated in eq. 4.10, a modified equation can be created that takes the specifics of a measurement into account. $N_{\mathrm{in}}(\lambda)$ is the number of total photons emitted by the setup, derived from the calibration measurement. $N_{\mathrm{out}}(\lambda, d \approx 27\,\mathrm{cm})$ is the number of photons detected on one side of the tube during the actual measurement (M), with a distance of $\approx 27\,\mathrm{cm}$ from the light input. To correct for intensity fluctuations from the light source, a correction term $C(\lambda)$ is introduced as stated in eq. 5.1. As shown in eq. 5.2, the correction therm is just the ratio of the values read from the reference PD during the calibration measurement $\mathrm{Ref}_{\mathrm{CM}}$ and the measurement $\mathrm{Ref}_{\mathrm{M}}$. Without intensity fluctuations $C(\lambda)$ is 1 and has no effect on the result.

$$\epsilon_{\mathrm{Wt}}(\lambda) = \frac{N_{\mathrm{out}}(\lambda, d \approx 27\,\mathrm{cm})}{N_{\mathrm{in}}(\lambda)} \cdot C(\lambda) \tag{5.1}$$

$$C(\lambda) = \frac{\mathrm{Ref}_{\mathrm{CM}}}{\mathrm{Ref}_{\mathrm{M}}} \tag{5.2}$$

The number of photons emitted, $N_{\text{in}}(\lambda)$, is obtained from the current Sig_{CM}[A] measured at the signal PD in the calibration measurement and the conversion function $R_\gamma(\lambda)$[A · s] for the PD, as stated in eq. 5.3. The conversion function is defined in eq. 5.4 and uses the PD response function[4] $R_{\text{PD}}(\lambda)[\frac{\text{A}}{\text{W}}]$ and the photon energy $\frac{hc}{\lambda}$[J] to convert detected current in photon numbers. τ[s] is the integration time of the measurement.

$$N_{\text{in}}(\lambda) = \frac{\text{Sig}_{\text{CM}}(\lambda)}{R_\gamma(\lambda)} \cdot \tau \tag{5.3}$$

$$R_\gamma(\lambda) = \frac{hc}{\lambda} \cdot R_{\text{PD}}(\lambda) \tag{5.4}$$

Since the PD is smaller than the tube end, a geometric correction factor, σ_{cor}, is introduced to $N_{\text{out}}(\lambda)$, as shown in eq. 5.5. σ_{cor} is equal to the ratio of the area on one tube end and the part of that area that is covered by the PD. The uncorrected number of photons $N_{\text{out,det}}(\lambda)$, detected at the end of the tube, is obtained from the current $\text{Sig}_{\text{M}}(\lambda)$[A] measured as described in eq. 5.6. Since the detected photons are now shifted in wavelength, the conversion to photon numbers is achieved based on the measured emission spectrum ($S_{WLS}(\lambda)$) of the paint. This is done by calculating the average photon number for a given current as described in eq. 5.7.

$$N_{\text{out}}(\lambda) = N_{\text{out,det}}(\lambda) \cdot \sigma_{\text{cor}} \tag{5.5}$$

$$N_{\text{out,det}}(\lambda) = \frac{\text{Sig}_{\text{M}}(\lambda)}{\langle R_\gamma \cdot E_\gamma \rangle} \cdot \tau \tag{5.6}$$

$$\langle R_\gamma \cdot E_\gamma \rangle = \int R_{\text{PD}}(\lambda) \cdot S_{WLS}(\lambda) \frac{hc}{\lambda} d\lambda \tag{5.7}$$

5.1.3 Results and Problems

The result of this measurement[5] and the correction described above can be seen in the previous chapter in fig. 4.5. The values are given as lower limits because the PD is unable to detect the whole angular distribution of photons leaving the tube, thus underestimating the efficiency. This was revealed by angular sensitivity measurement of the PD and later confirmed by the manufacturer. PDs are semiconductor-based light detectors similar to solar cells. To protect the sensitive semiconductor surface, the sensor itself is in most cases placed in a sealed protective casing as illustrated in fig. 5.2.

In most cases, the volume between the protective glass window and the sensor is filled with an epoxy resin for optical coupling. The manufacturer (Hamamatsu) confirmed that this is not the case for their UV-sensitive PDs since the resin is not UV transparent. Instead, the volume is left empty ($n \approx 1$), causing light under steep angles to be reflected on the inner glass surface. This is confirmed by the measurement shown in fig. 5.3. As sketched on the left, the full angular input distribution was measured with a PMMA half-cylinder lens directly coupled to the PD. The cut-off at about 41°, and some scattered light beyond that, can be seen on the right. For comparison, a measurement without the lens (and thus less steep input angles for the PD) is also shown. Due to this complication, it was decided to proceed to measure with PMTs and only use a PD where absolute values are not relevant. This is a better choice since no air gap exists for PMTs. This does not mean that there is no angular dependency

[4] Intrinsic to the specific PD (type) and for the PDs used in this thesis supplied by the PD manufacturer.
[5] Scaled by a factor of two to approximate the output for both tube sides.

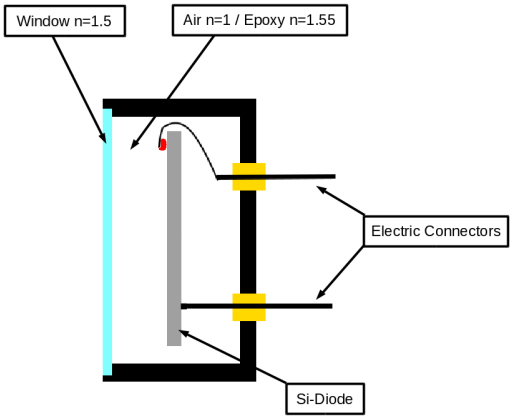

Figure 5.2: Sketch to illustrate the casing design of most PDs.

for the photon acceptance, however, in the final prototype, PMTs will be used, and therefore, the results from PMT measurements should represent a realistic estimate for the final module performance. This means that all efficiency measurements performed previous to this thesis are only lower limits. Since the exact angular distribution of light in the tube is difficult to measure, it is not possible to reliably correct or scale previous measurements accordingly.

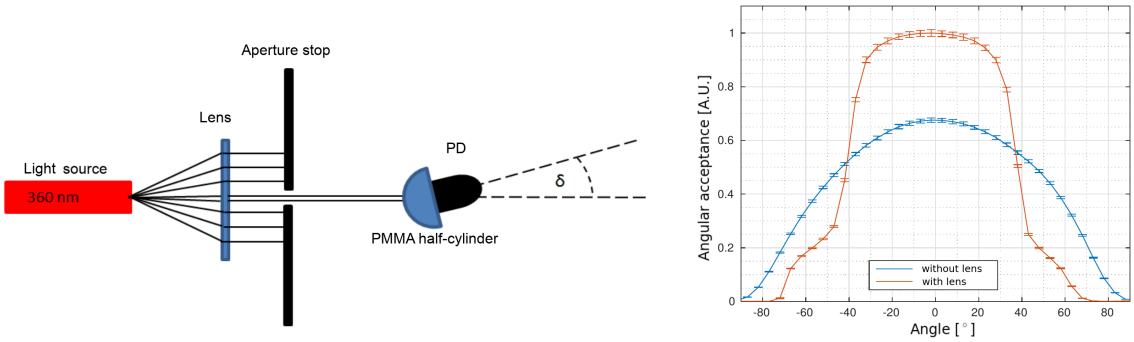

Figure 5.3: (left) Setup to measure PD angular acceptance for optically coupled light guides. (right) Results from the angular acceptance measurement, with and without optically coupled PMMA half-cylinder lens. Both images are translations from [104].

5.2 First PMT Measurements

In the next step, first measurements with a PMT and small (2 cm) tubes are performed. For that, a different laboratory setup, as well as different measurement and evaluation methods, are required.

5.2.1 The Setup

In order to circumvent the PD issues, a PMT based test stand was set up. The basic setup can be seen in fig. 5.4. A signal generator (used as trigger) sends a signal to a LED/Laser-driver[6] to generate a

[6] PDL 800 B Laser Pulser from PicoQuant [105]

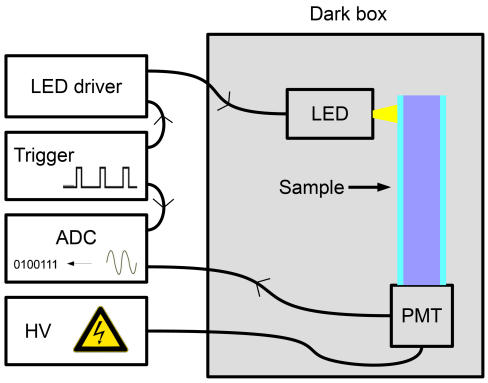

Figure 5.4: Illustration of the PMT setup.

light pulse. The light pulse is directly (in a reference measurement) or indirectly (through a sample in a signal measurement) detected by a PMT. The PMT is supplied by a high-voltage power source (HV) and sends its signal to the analog-to-digital converter[7] (ADC). The ADC is also triggered by the signal generator, to integrate the waveform produced by the PMT and to store the value digitally. The trigger to the ADC is delayed in comparison to the LED, to account for the longer signal-path length. The light-sensitive part of the setup is placed inside the dark box, shown in fig. 5.5 (left). The optical setup is shown in fig. 5.5 (right), depicting a sample measurement.

Figure 5.5: (left) The dark box build for PMT measurements. (right) Sampling setup.

For the pulsed LED, two different suitable wavelengths were available: 310 and 370 nm. Both have higher intensities than suitable for the measurements. Therefore, the light is attenuated for PMT measurements. The attenuation is done with either two 10 % neutral density (ND) filter (for the 310 nm LED) or a combination of a 1 % and a 0.32 % ND filter (for the 370 nm LED).[8] To more accurately obtain the desired light intensities, a variable aperture is used. For a calibration measurement, the light

[7] 8 channel charge integrating ADC, MOD. V 265 [106]

[8] Due to the use of reflective filters the actual attenuation might differ from the linear combination of the individual attenuations.

produced by this LED attenuator combination is directly pointed at the PMT. For the measurement setup, the test tube is put in front of this setup, as shown in fig. 5.5 (right). The test tube is placed between the PMT and absorber in a way that only a small amount of pressure is applied. The black absorber reduces inaccuracies in the measurement from photons being reflected at the tube end. Absorber and PMT are coupled to the test tube with a small amount of optical grease. The PMT used is an R11265U-200 by Hamamatsu [107]. This PMT was chosen because of its flat surface that easily couples to the tube.

5.2.2 Measurement and Evaluation Techniques

With the above-described setup, the PMT can be operated in a dynamic or single-photon range. The possible evaluation methods change depending on the type of operation.

Dynamic Range Measurements

For the dynamic range, the light intensity is chosen such that for each LED pulse $n >> 1$ photons are detected. n is not constant, but will fluctuate slightly around an average $\langle n \rangle$. When sampling many times, a histogram on the resulting charge on the anode can be created.[9] n is Poisson distributed, and since $n >> 1$, it can be approximated as a Gaussian distribution. Since a PMT, with a Poisson distributed amplification process, is used for the photon detection, the Gaussian properties of the resulting histograms are enhanced. An example of a histogram is shown in fig. 5.6.

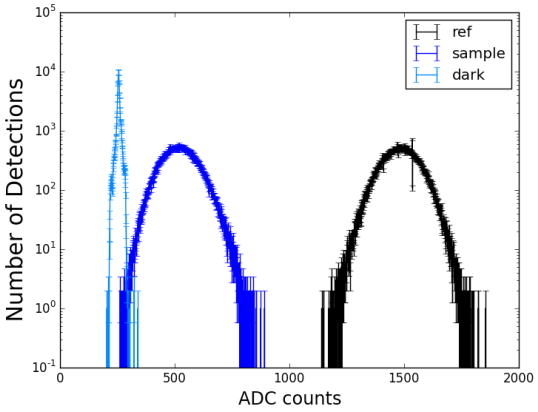

Figure 5.6: Exemplary histograms for measurements in the dynamic range. the first (light blue) peak is the zero or dark measurement without light. The second (dark blue) peak is a measurement of a sample. The third (black) peak is a reference measurement with the light source directly pointing at the PMT. ADC counts correspond linearly to the collected charge.

Evaluation of Dynamic Range Measurements

To determine the efficiency from a dynamic range measurement, an additional dark measurement[10] is required. The dark measurement determines the average charge for a null-measurement. Eq. 5.8 describes the efficiency based on a dynamic range measurement. μ_i is the mean value for the measurement $i \in$ [sample, dark, ref]. $\tilde{C}(\lambda)$, as described in eq. 5.9, is the correction factor for the

[9] The process used for the histogramming the data depends on the data taking device.
[10] An identical measurement without light.

wavelength-dependent PMT response, analogous to the PD measurement. $R_{\mathrm{PMT}}(\lambda)$ is the PMT response function and ϵ_{PMT} the probability to detect a photon emitted by the WLS, as described by eq. 4.8.[11] The factor of two compensates for the side of the test tube that was not read out.[12] This evaluation is reliable, provided that the PMT response is linear with intensity. This has to be tested for each PMT model and gain used. In most cases, this a given when the intensity is kept low.

$$\epsilon_{\mathrm{Wt}} = 2 \cdot \frac{\mu_{\mathrm{sample}} - \mu_{\mathrm{dark}}}{\mu_{\mathrm{ref}} - \mu_{\mathrm{dark}}} \cdot \tilde{C}(\lambda) \tag{5.8}$$

$$\tilde{C}(\lambda) = \frac{R_{\mathrm{PMT}}(\lambda)}{\epsilon_{\mathrm{PMT}}} \tag{5.9}$$

Single Photon Measurements

For the single-photon measurements, the light intensity is chosen in a way that approximately one or fewer photons are detected per trigger event. In general, an average of $\frac{1}{10}$ photons per trigger event is a useful value to aim for. At this rate, multiple detections are suppressed by a factor of ≈ 20; but the rate is high enough for a reasonably short measurement time and a high signal to noise ratio. This is not possible when two measurements with different intensities are compared and a compromise in the detection rate must be found. In contrast to the dynamic range measurement, a single-photon measurement does not rely on the number of photons per event for evaluation. In a single-photon measurement, the number of photons in the so-called single photoelectron (SPE) peak, is used for the evaluation. In other words the number of photons seen over several trigger events. An exemplary histogram of such a measurement is shown in fig. 5.7. It can be seen that the vast majority of events are in the pedestal. It represents the samplings where no photon was detected. The central lower peak is the desired SPE peak.

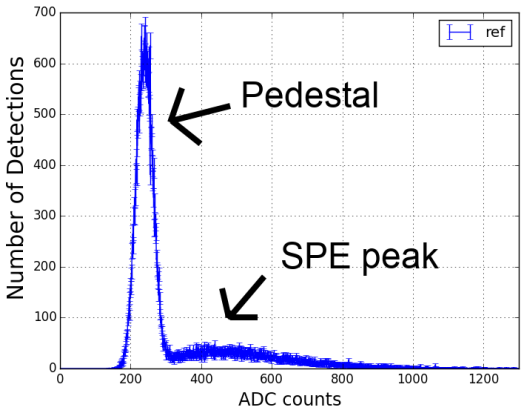

Figure 5.7: Exemplary SPE histogram. The large peak (at about 250 ADC counts) is the so-called pedestal and it represents a zero measurement. The small peak (at about 500 ADC counts) is the SPE peak.

[11] The PMT response functions are taken from the datasheets of the individual PMT type used.
[12] This is mainly done for legacy reasons.

Fitting of SPE Measurements

To compare SPE measurements, it is important to know the number of hits in the pedestal or the SPE peak. The pedestal is noise dominated and, therefore, approximately Gauss shaped. The SPE peak is an accumulation of Poisson-distributed interactions at the different dynodes in addition to the noise and, thus, also approximately follows a Gauss distribution. Both functions overlap slightly. The size of the overlap and the width of the distributions varies depending on electronic noise, gain, PMT and ADC used.

Based on this simplified model, the fit method [108] involves fitting two Gaussians to the histogram (one for each peak). Two examples are shown in fig. 5.8. The left plot is an example of a good result and the right an example of a bad result (in comparison to the majority of fits). Both are no ideal fits, as the corresponding $\frac{\chi^2}{\text{d.o.f.}}$ values of 1.39 (left) and 2.40 (right) show. Especially in the right case, the Gaussian distribution for the SPE peak extends to lower x-values than the pedestal. This is physically implausible and overestimates the size of the SPE peak when integrating the area under the curve. In both cases, the number of measurements with large charge depositions are underestimated. This method can be a useful first approximation, but is ultimately unreliable. The efficiency can be estimated according to eq. 5.10, under the condition that the total number of events is identical in the reference and in the sample measurement. G denotes the integral of a Gaussian curve. As before, the factor of two compensates for the side of the test tube that was not read out.

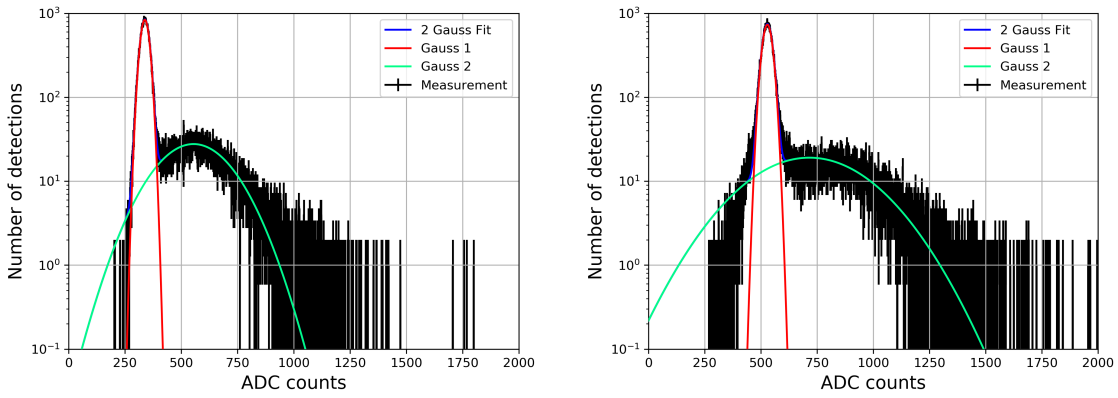

Figure 5.8: Exemplary histograms for fitting two Gaussian functions to two SPE measurement with different light intensity and gain. (left) An example of a reasonable fit, with a $\frac{\chi^2}{\text{d.o.f.}}$ of 1.39. (right) An example of a poor fit, with a $\frac{\chi^2}{\text{d.o.f.}}$ of 2.40.

$$\epsilon_{\text{Wt}} = 2 \cdot \frac{G_{SPE,sample}}{G_{SPE,reference}} \cdot \tilde{C}(\lambda) \tag{5.10}$$

A reason for the low fit quality is that there are not just single photons detected (as SPE would imply) but multiple (> 1) photons. In SPE measurements, the multi photo-electron peaks (MPEs) are smaller than the SPE and merge with it. Without additional constraints, it is difficult to fit multiple Gaussians to these distributions, since the degrees of freedom increase and the best fit results are not a representation of the underlying physics. The numbers of photo-electrons are Poisson distributed. Therefore, a reduction in photon intensity can increase the accuracy of this method. To estimate the accuracy of this method,

the integral of both distributions was summed and compared with the sum of all events. For most cases this matched within less than $1 - 2\,\%$. The result itself, however, fluctuated more than for other methods described in this section. This seems partial due to the large difference in intensity between measurement and calibration measurement, as well as the fit quality.

Cutting for SPE Measurements

Another rudimentary method, used to make decisions on an individual event basis, is the application of a cut between pedestal and SPE peak. This method is also applied in IceCube [46], as a first measure to suppress noise signals below $25\,\%$ of the charge for an average SPE-pulse is discarded. Though the cut makes it harder to determine an error for the overlap of pedestal and SPE-peak. To keep the overlap as symmetric as possible, the cut is applied in the minimum between both peaks. An example can be seen in fig. 5.9. Between signal and reference measurement, there are two ways to do this. The cut could be set once (for instance with the reference measurement) and applied for all other measurements, or it could be set for each individual measurement. To evaluate the events, the number of events on each side

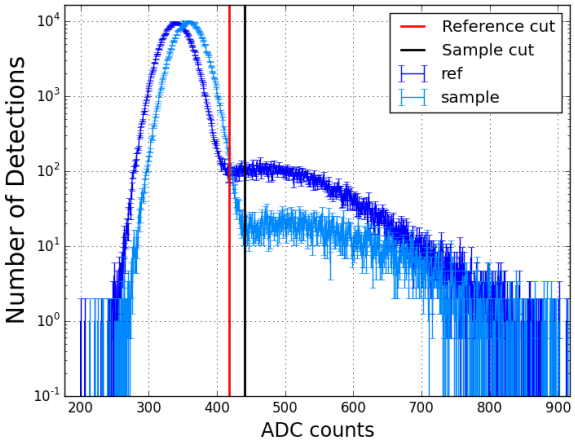

Figure 5.9: Exemplary histograms for cuts between pedestal and SPE peak.

are summed up to determine the number of events in the pedestal and the SPE peak. To determine the efficiency, the ratio between sample ($N'_{\mathrm{SPE,sample}}$) and reference SPE peak ($N'_{\mathrm{SPE,reference}}$) measurement sums (including the correction factor $\tilde{C}(\lambda)$) can be used, as described by eq. 5.11. Again, the factor of two compensates for the side of the test tube that was not read out.

$$\epsilon_{\mathrm{Wt}} = 2 \cdot \frac{N'_{\mathrm{SPE,sample}}}{N'_{\mathrm{SPE,reference}}} \cdot \tilde{C}(\lambda) \tag{5.11}$$

To approximate the error, it is determined how much the efficiency would change when the chosen cut value is moved ±10 ADC bins. This produces four values, two for each the sample and reference measurement. For all combinations, of sample and reference measurements, eq. 5.11 is evaluated again. The largest difference of any of these reults to the original result is used to determine the error for this method. It remains to be noted, that with large differences in intensity between compared measurements, the pedestal/SPE-peak overlap-ratio changes to an unknown degree. This effect is reduced when the maximal gain is chosen, yet this produces a non-neglectable systematic uncertainty. The value of 10

bins was chosen empirically. When pre-amplifiers or newer devices were used, the number of bins was adapted accordingly. An illustration and test of accuracy, including overlap but not under-amplified photons, for the 10-bin error calculation method can be found in chapter A.2.1.
The measurements performed to determine ϵ_{Wt} show large differences in intensity. Therefore, it is unavoidable to have MPE contributions when measuring an SPE distribution. For both the fit method, as well as the cut method, there needs to be an MPE correction. Up until now, MPE contributions are weighted as one photon. To correct for that, it is possible to determine (from the probability for a no-photon detection; the pedestal size) the statistically expected ratio of events with 1,2,3 or more photons. This is done by using the Poisson distribution as stated in eq. 5.12.

$$P(i, < n >) = \frac{e^{-\langle n \rangle} \langle n \rangle^i}{i!} \tag{5.12}$$

This means that $P(i, \langle n \rangle)$ is the probability for i photons to be detected when $\langle n \rangle$ is the expected number of detections for a single trigger. With N_Z being the number of events in the pedestal, and N_T the total number of events, it is possible to determine $\langle n \rangle$ according to eq. 5.13.

$$\langle n \rangle = -\ln \frac{N_Z}{N_T} \tag{5.13}$$

The absolute efficiency for the cut and the fitting method is then calculated according to eq. 5.14.

$$\epsilon_{\mathrm{Wt}} = 2 \cdot \frac{\langle n_{sample} \rangle}{\langle n_{reference} \rangle} \cdot \tilde{C}(\lambda) \tag{5.14}$$

This correction is performed on all applicable measurements in this thesis.

Improved Fitting of SPE Measurements

With these corrections, it is also possible to constrain the size of additional Gauss distributions in a multi Gauss fit. Any given Gaussian distribution (G) (as in eq. 5.15) can be described by an area or scaling factor (A), its position (μ) and its width (σ).

$$G(x \mid A, \mu, \sigma) = \frac{A}{\sqrt{2\pi\sigma^2}} e^{-\frac{(x-\mu)^2}{2\sigma^2}} \tag{5.15}$$

Assuming these values are determined for the pedestal of an SPE measurement, the number of photons (A)[13] in any subsequent Gaussian distribution for SPE and MPEs can already be determined from the Poisson distribution if the total number of events (N_T) is known. Thus, the Gauss distribution describing the SPE only requires the determination of its position (μ_{SPE}) and width (σ_{SPE}). If the detection of two photoelectrons is viewed as the independent detection of two photoelectrons, the corresponding peak can be described as the combination of two independent normal distributed variables. It would follow that $\mu_{\mathrm{2PE}} = 2\mu_{SPE} - \mu_{\mathrm{pedestal}}$ and $\sigma_{\mathrm{2PE}} = \sqrt{2}\sigma_{\mathrm{SPE}}$. Expanding this to all MPEs, then eq. 5.16 and eq. 5.17 follow for $i > 1$.

$$\mu_{i\mathrm{PE}} = \mu_{\mathrm{pedestal}} + i \cdot (\mu_{SPE} - \mu_{\mathrm{pedestal}}) \tag{5.16}$$

$$\sigma_{i\mathrm{PE}} = \sqrt{i} \cdot \sigma_{\mathrm{SPE}} \tag{5.17}$$

[13] Area under the curve.

Therefore, a five parameter fit with one constant is able to describe an SPE histogram using infinitely many Gaussians distributions as shown by eq. 5.18.

$$\begin{aligned} M(x \mid N_T, & A_{\text{pedestal}}, \mu_{\text{pedestal}}, \sigma_{\text{pedestal}}, \mu_{\text{SPE}}, \sigma_{\text{SPE}}) = \\ & G(x \mid A_{\text{pedestal}}, \mu_{\text{pedestal}}, \sigma_{\text{pedestal}}) \\ & + G(x \mid N_T \cdot P(1, <n>(A_{\text{pedestal}}, N_T)), \mu_{\text{SPE}}, \sigma_{\text{SPE}}) \\ & + \sum_{i>1} G(x \mid P(i, <n>(A_{\text{pedestal}}, N_T)), \mu_{i\text{PE}}(\mu_{\text{pedestal}}, \mu_{SPE}), \sigma_{i\text{PE}}(\sigma_{\text{SPE}})) \end{aligned} \tag{5.18}$$

The efficiency ϵ_{Wt} can be calculated based on $P(i, <n>(A_{\text{pedestal}}, N_T))$ and eq. 5.14. Applying this technique in practice has shown some complications.

While the fits look very good on visual inspection (as for example in fig. 5.10), their $\frac{\chi^2}{\text{d.o.f.}}$ depends on the specific setup (PMT, ADC/ADQ, gain, light intensity, number of measurements) that is used. For fig. 5.10 the $\frac{\chi^2}{\text{d.o.f.}}$ is 3.55. This is rather high but in this specific case due to the very high statistics and hence the relatively small errors. Applying this method to the histograms in fig. 5.8 produces $\frac{\chi^2}{\text{d.o.f.}}$ in the range of 1.1 to 1.2 and is, therefore, a significant improvement over the two Gauss fit. An inspection of the residual in fig. 5.10 shows that the range between pedestal and SPE has the highest discrepancy. This is the range where usually under-amplified photo-electrons are detected. Under-amplified electrons are those following an ineffective trajectory. An ineffective trajectory could either mean that a photon produces the photo-electron at the first dynode instead of the photocathode or that the photo-electron skips the first dynode. The modelling of under-amplified photo-electrons is difficult because it depends on the structure of the individual PMT. The under-amplified photo-electrons are accounted for in the total number of events (N_T), but are unaccounted for by the model. Therefore, the number of under-amplified photo-electrons in a measurement will determine the lower bound on systematic uncertainty.

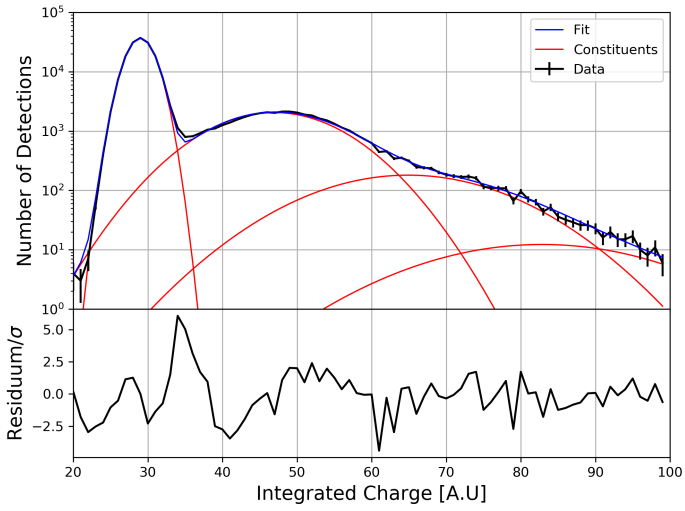

Figure 5.10: Exemplary SPE histogram for a five parameter multi-Gauss fit with a $\frac{\chi^2}{\text{d.o.f.}}$ of 3.55. The lower part shows the error weighted residuum.

Partial Fitting of SPE Measurements

Another method investigated was the partial fitting of the histogram. For this method, the approximate position and width of the pedestal are determined. Based on this, 80 % of the pedestal towards lower charges is cut off. The remainder of the pedestal and the SPE peak is fitted with one or two Gaussian distributions as well as an exponential distribution. The function is described by equation 5.19 and an example fit can be seen in fig. 5.11.

$$P(x \mid A_1, \mu_1, \sigma_1, A_2, \mu_2, \sigma_2, a, l, b) = G(x \mid A_1, \mu_1, \sigma_1) + G(x \mid A_2, \mu_2, \sigma_2) + a \cdot e^{\frac{-x}{l}+b} \tag{5.19}$$

Whether one or two Gaussian distributions produce better results, depends on the PMT and the light intensity that is used. It is generally preferred to use low light intensities and a single Gaussian distribution to reduce the probability of bad fitting behaviours. The $\frac{\chi^2}{\text{d.o.f.}}$ of the example plot is 1.37, which is good in comparison to the other methods. Though it should be taken into account that only a part of the Distribution is fitted. Using only one Gaussian distribution, this method is used in the calibration of IceCube DOMs [46]. However, under-amplified photoelectrons are not separated from the pedestal and are therefore not counted as detections. Furthermore, the mathematical description is not based on empirical physics as illustrated by the broad Gaussian distribution in the example plot. Using only one Gaussian distribution eq. 5.10 can be used for the evaluation, while having similar uncertainties as to the simple two Gauss fitting approach. The two Gauss distribution and one exponential function approach describes the distribution better, but is unsuitable for an evaluation in this context; since the second Gaussian distribution might not describe the actual MPE distribution, as it can be seen in the example plot.

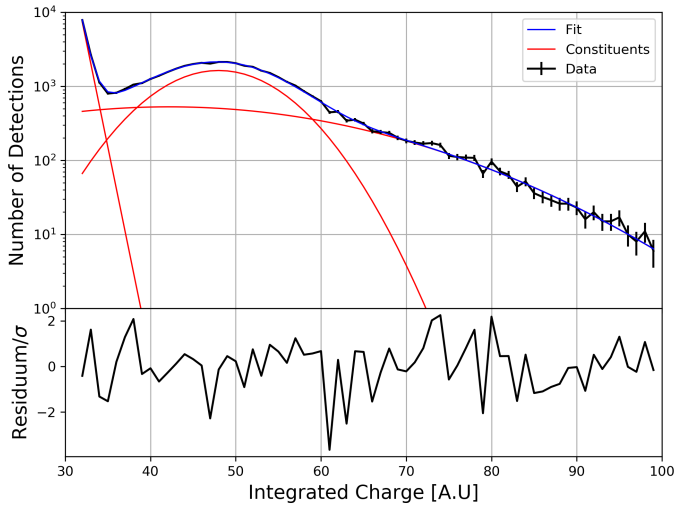

Figure 5.11: Exemplary histograms for a fit of a partial SPE histogram with a $\frac{\chi^2}{\text{d.o.f.}}$ of 1.37. The lower part shows the error-weighted residuum.

Model-Independent Evaluation Approach

The idea behind the model-independent approach is to not look at any distribution shapes or make assumptions about them. Instead, ϵ_{Wt} is calculated purely on the statistical properties of the distributions, thus also eliminating the need to model under-amplified photons. The mathematical description is based on the model-independent approach for PMT calibration found in [109]. In the paper, the mean ($E[\psi]$) and the variance ($V[\psi]$) of a single photo-electron response is described as in eq. 5.20 and 5.21, respectively.

$$E[\psi] = \frac{E[T] - E[B]}{\langle n \rangle} \tag{5.20}$$

$$V[\psi] = \frac{V[T] - V[B] - E^2[\psi] \cdot \langle n \rangle}{\langle n \rangle} \tag{5.21}$$

Where $E[T]$ is the mean of the signal measurement, $E[B]$ is the mean of a dark measurement and $V[T]$ and $V[B]$ the corresponding variances. $\langle n \rangle$ is as before the number of expected photons per trigger.[14] Assuming that $E[\psi]$ is identical for a sample and a reference measurement, it follows eq. 5.22 and 5.23.

$$\frac{E[T_{\mathrm{sample}}] - E[B]}{\langle n_{\mathrm{sample}} \rangle} = \frac{E[T_{\mathrm{reference}}] - E[B]}{\langle n_{\mathrm{reference}} \rangle} \tag{5.22}$$

$$\Rightarrow \frac{\langle n_{\mathrm{sample}} \rangle}{\langle n_{\mathrm{reference}} \rangle} = \frac{E[T_{\mathrm{sample}}] - E[B]}{E[T_{\mathrm{reference}}] - E[B]} \tag{5.23}$$

Using eq. 5.14, ϵ_{Wt} can be determined, as described by eq. 5.24.

$$\epsilon_{\mathrm{Wt}} = 2 \cdot \frac{E[T_{\mathrm{sample}}] - E[B]}{E[T_{\mathrm{reference}}] - E[B]} \cdot \tilde{C}(\lambda) \tag{5.24}$$

This way the method does not assume any particular shape for the distributions, it is based purely on statistics and a mathematical error that can be calculated based on the variances. The method basically reduces the evaluation of an SPE measurement to the evaluation of a dynamic range measurement.

Since in the paper $E[\psi]$ is the desired parameter, it contains also another method to determine $\langle n \rangle$ and, thus, ϵ_{Wt}. This method also requires a dark measurement, as well as an SPE measurement. In the dark measurement, a cut is placed at a low charge value, so that approximately one-third of all triggers falls below this value. The number of triggers that fall below the value is defined as f. The same cut is applied in the SPE measurement. The number of triggers in the pedestal is approximated by scaling the number of triggers below the cut (A_T) with f. Inserting this in eq. 5.13 produces eq. 5.25.

$$\langle n \rangle = -\ln \frac{A_T}{f \cdot N_T} \tag{5.25}$$

This way, the influence of the overlap between pedestal and SPE-peak is minimized. Based on this, ϵ_{Wt} can be determined with eq. 5.14. When in this thesis it is referred to the model-independent evaluation method, this refers to the one described by eq. 5.24 (unless otherwise specified).

[14] The variable used in [109] is λ.

Conclusion on Evaluation Techniques

To perform the PMT measurements presented in this thesis, the above measurement techniques have been evaluated. From a mathematical point of view, the model-independent evaluation approach outperforms the other methods since it is independent of the PMT type. It also accounts for under amplified-photoelectrons and can be applied to both SPE and dynamic range measurements. In praxis, this method is very sensitive to systematic effects that cannot always be corrected for, furthermore, mathematical or visual checks of consistency with the data are difficult. All contributions (especially noise) that are not linear with the number of photoelectrons, are not accounted for and can cause large fluctuations in the results. For the Analogue Digital Converter (ADC)[15] (which is used to read out signals in early measurements) several such contributions have been observed, as described in the following section. Since only the charge integral is stored, and the sampling rate was limited to about 200 Hz, a thorough investigation, of these contributions, was not always possible or feasible. Most of the above methods showed problems with these systematics. Particularly a shift in base value position and non-linear noise contributions showed to be problematic. Empirically it was shown that the cut-method (while being the mathematically least consistent method) produced the most consistent results and was therefore used for most of the measurements. For later measurements, an ADQ14[16] became available that sampled and stored individual waveforms at $\mathcal{O}$(MHz]) rates. Data quality improved significantly and all of the above methods produced self-consistent results. Therefore, evaluation of data from the ADQ14 was preferably performed with the model-independent evaluation approach for its mathematical superiority. The only shortcoming of this method has been observed with large PMTs and a position-dependent gain. In those cases, a calibration or the use of the improved fitting method is recommended. A data-based comparison between the different evaluation techniques can be found in section 5.4.4. While the significant improvements, when switching to the ADQ14, do not speak for the quality of data measured with the ADC, there was no alternative available at the time.

5.2.3 Systematics of PMT Measurements

The first measurements were done in the dynamic range of the PMT to obtain a reference. The results for the efficiency fluctuated by up to 50 %. As a result, additional SPE measurements were taken. In those three problems have been identified that are presented in the following.

Unstable Base Value

With the ADC setup, the pedestal sometimes moved between measurements, fig. 5.9 shows an example. Further investigations showed, that the effect was stronger for some channels of the device than others. While this problem could never be completely avoided a minimization was achieved by an appropriate selection of channels. As far as it was possible to determine the problem only occurred between but not during measurements. This indicates a design or ageing problem with the very old device, however, the exact cause remains unclear. Based on the maximum shift of 17 in ADC counts observed between measurements, a systematic error can be estimated for the individual dynamic range measurements. For methods like the cut method, fixed cuts can not be used, but they need to be set based on individual measurements. The individual adjustment produces additional uncertainties.

[15] 8 channel charge integrating ADC, MOD. V 265 [106]
[16] 4 channel 14-bit digitizer, ADQ14 with 1 GSPS sampling rate and USB3.0 [110]

Additional Peak

In some low-intensity SPE measurements, an additional peak could be observed between pedestal and SPE peak. This can be seen in fig. 5.12. It was observed that this "bump" is correlated to the use of a specific HV-supply. The particular power supply was not used any further to resolve the problem. Similar things tend to happen in this kind of measurement, especially when using older equipment. It is impossible to be sure that all of them have been detected. For instance, after switching to the ADQ14 it was found that about 90 % of the cables used in these measurements were insufficiently shielded [99], adding additional non-linear noise to the measurements. This produces an additional systematic uncertainty on efficiency measurements, which should be considered for all measurements taken with the ADC. Similar noise contributions have been observed on occasion with the ADQ14 as well. Since the ADQ14 records the whole waveform, these contributions can be better identified and removed. They are assumed to be related to the use of high power equipment in vicinity of the laboratory.

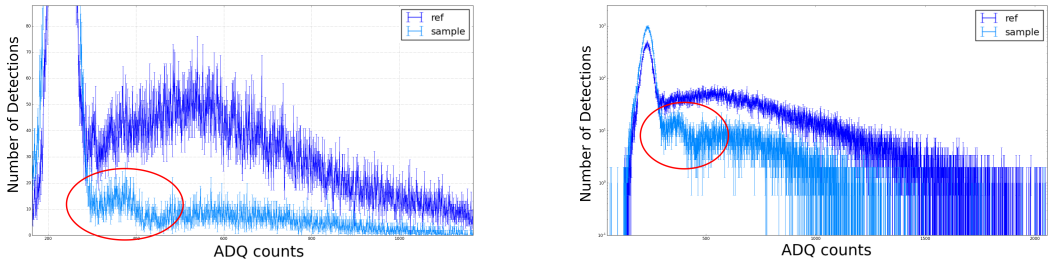

Figure 5.12: A exemplary SPE measurement to show the additional "noise" peak between pedestal and SPE peak. (left) Linear representation. (right) logarithmic y-axis.

Spatial Photocathode Sensitivity

It was also noted that in SPE measurements the SPE-peak moved relative to the pedestal between reference and sample measurement. An example is shown in fig. 5.13. The reference measurement peaks before the sample measurement. Due to the difference in intensity, the MPE contributions should have the opposite effect. Any effects related to the optical grease, that is used to optically connect the sample to the PMT, have been excluded by measurements.

Lastly, the PMT itself was investigated. For the investigation, the light source was pointed at the PMT surface. Measurements were taken on various positions of the PMT surface as illustrated by fig. 5.14 (left). The SPE-peak position was determined in each case and plotted as shown in fig. 5.14 (right). The plot shows that the SPE peak position or in other words the gain is lower in the center where the reference measurements were taken. This can be explained with the shape of the first dynode, which varies between different PMTs. To answer the question if this affects the efficiency, the SPE measurement distributions were fitted with Gaussians. Since the same low intensities were used in all measurements, it was possible to use the above described two Gaussian fitting method. The integral of the Gaussians fitted to the SPE-peaks were also plotted in fig. 5.14 (right), showing no significant effect on the photon number. However since the model-independent method relies on the gain being constant, this effect has a large influence on this method. This limits the use of this method to accordingly calibrated or very small PMTs.

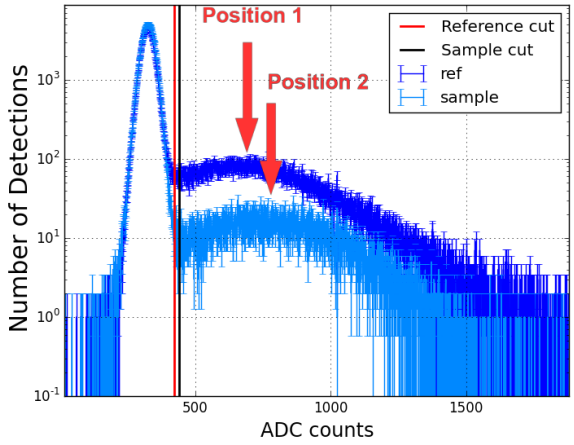

Figure 5.13: Exemplary measurement for a difference in SPE position relative to the pedestal between reference and sample measurement.

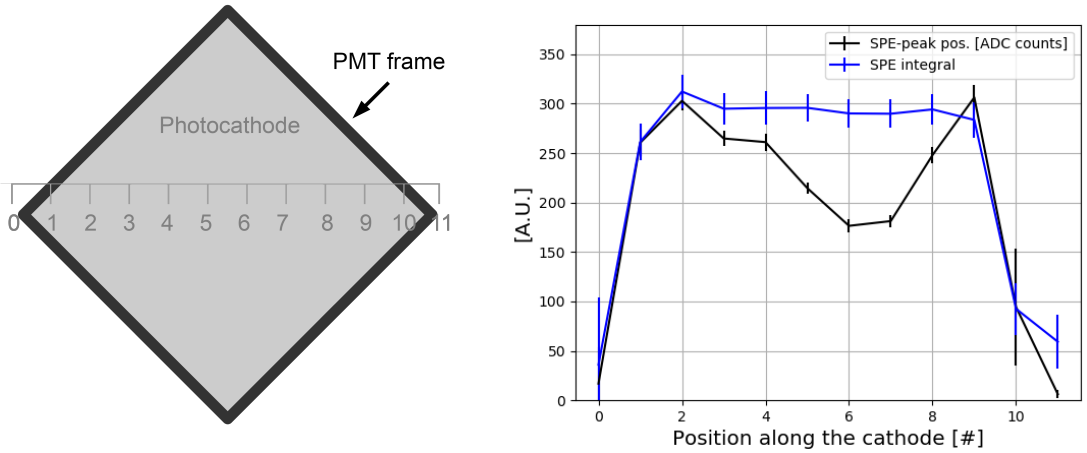

Figure 5.14: (left) The locations on the PMT (R11265U-200 by Hamamatsu [107]) the light source was pointed at during the cathode scan. Each step is about 3.5 mm. Since the placement had to be done manually the error can be approximated to be ±1 mm. (right) Results of the cathode scan in SPE-peak position and integral.

5.2.4 Results

For efficiency measurement with PMTs a test stand has been set up. 30 cm long and 2 cm diameter PMMA tubes, with a wall thickness of 2 mm, coated with a velocity of 8.1 ± 0.1 $\frac{\text{cm}}{\text{min}}$ [17] have been produced. With the paint applied to the inside and outside. The light source had a distance to the PMT of 27 cm. The measurements were performed in the SPE range as well as in the dynamic range. A range of evaluation techniques has been investigated for the SPE measurements. For its stability in comparison to the other methods, the cut method has been selected for the evaluation of SPE measurements. The cuts were applied to the lowest value between pedestal and SPE, of each measurement. This method is not ideal but for measurements with the ADC it produced the most reproducible results in comparison

[17] Coater velocity.

to the other methods. This indicates unresolved problems with the device.

In the end, four measurements at 370 nm wavelength have been performed in the dynamic range. The combined result for ϵ_{Wt} is 49.6 ± 12.4 % with an estimated systematic error of ±5 %. Also, six SPE measurements have been performed four at 310 nm and two at 370 nm wavelength. The averaged results are $\epsilon_{\mathrm{Wt}} = 52 \pm 2\,\%$ for 310 nm and $\epsilon_{\mathrm{Wt}} = 50 \pm 3\,\%$ for 370 nm. While the used cut method includes some systematic errors and the dynamic range measurements have already a large statistical error, the results indicate that the obtainable efficiencies are larger than the ones measured with PDs. However, systematics from the equipment remains a source for not quantified errors.

5.3 Efficiency at Low Temperatures

At the proposed deployment site for IceCube-Gen2 at the South Pole, the temperature conditions are very different from the test conditions in the laboratory. To test how the performance changes under these conditions, a comparison measurement for different temperatures was done. For this, a small air and light-tight box (freezer box), is equipped with a setup similar to the one in the black box as described in section 5.2.1. A picture is shown in fig. 5.15.

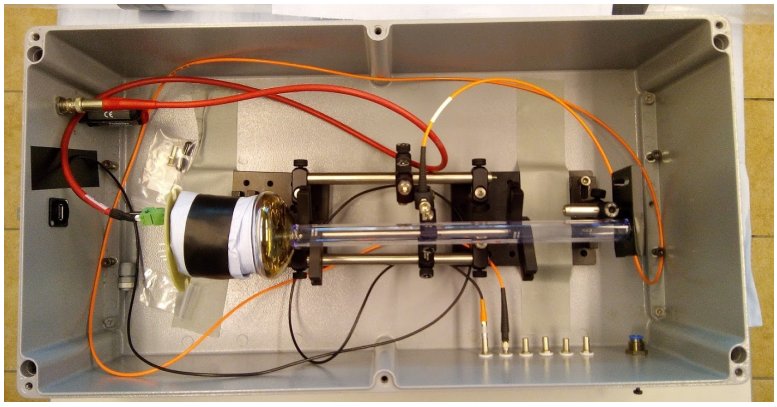

Figure 5.15: Freezer box setup to compare the paint performance at low temperature to room temperature.

The light source is now set up in another light-tight box outside the freezer since it can not be frozen. The light is feed from the box through an optical fiber into the freezer box (orange cable). The PMT used is a Hamamatsu R12199-02, that is coupled with optical gel to the sample. Larger quantities of gel are used to bridge small gaps between the curved PMT surface and the flat end of the tube. The PMT was chosen because it is also considered to be used in the WOM. This creates a better representation of the conditions in the deployed sensor. The HV (red cable) and the signal (black cable) cables are feed in the box through light-tight connectors. A 2 cm diameter PMMA tube coated on the inside and outside as in the previous sections was used. For a measurement, the freezer box is sealed and placed in a commercial freezer unit. First, a room temperature measurement at $\approx 25\,^{\circ}\mathrm{C}$ is taken. Then the freezer is switched on and once it cooled down to $\approx -50\,^{\circ}\mathrm{C}$ another measurement is taken. The same procedure is repeated for the reference measurement. This resulted in an efficiency $\epsilon_{\mathrm{Wt}} = 51.0 \pm 0.1\,\%$ for the measurement in warm conditions and $\epsilon_{\mathrm{Wt}} = 47.3 \pm 1.2\,\%$ in cold conditions, using the cut method. The absolute systematic errors are estimated again to be about 5 %. Since two almost identical measurements are compared the systematic error for the comparison with the cut measurement is minimal. It can not be excluded that humidity condensed on the tube during the cold measurement,

producing more light scattering in that measurement. However, since the box is cooled outside in any humidity would likely freeze on the box walls. Usually, these measurements are done right after one another, but in this case, it took a day for the freezer to cool down. Therefore an additional systematic error for the comparison is estimated with 5 %. In conclusion, it can be said that both measurements are consistent with each another, while the systematic uncertainties from the previous measurement apply as well.

5.4 Full-Sized Light-guiding PMMA Tubes

After successfully using the 30 cm long and 2 cm diameter tubes for paint and concept tests, the next step is the application of the same techniques to full-sized 9 cm diameter and 90 cm long tubes.

5.4.1 The New Coating Setup

For the final sensor, the entire length of the tube needs to be coated. In the old setup, a flask clamp from the chemistry department has been used to hold the tube during coating. This coats the tube from the inside and outside and leaves a non coated area on one side. Therefore a new coating procedure needs to be designed. To obtain the efficiency calculated in section 4.3.4, the paint can only be on the outside. For this purpose, a new holding structure was devised as shown in fig. 5.16. With this structure, the tube is squeezed in between a top and a bottom piece. The contact points are sealed with PTFE O-rings so that no paint can enter the tube. During the coating, this setup allows a complete immersion and thus coating of the outer surface of the tube. This way also the tube ends are protected from being coated with paint. To accommodate the larger tube a stainless steel vessel for the paint was build as shown in fig. 5.17.

Figure 5.16: (left) The pieces that hold and seal the large diameter tube for coating. (right) The same holders holding a short piece of tube for illustration.

Due to the now larger displacement and changed diameter of the paint vessel, the coating velocity needs to be adjusted. For that eq. 5.26 is used, where the real coating velocity v_{real} is calculated from the coater velocity v_{coater}, the inner cross-section area A_{vessel} of the paint vessel and the A_{tube}. The optimal coater velocity determined in [86] is $8.1 \pm 0.1 \frac{\text{cm}}{\text{min}}$. There 2 cm diameter tubes with 2 mm wall thickness have been used in a 3 cm diameter paint vessel. Now a 12.75 cm diameter vessel is used with a 9 cm diameter tube, where paint can not enter the center of the tube. This results in the optimum

Figure 5.17: (left) Stainless steel coating vessel with PTFE lid for permanent paint storage. (right) The coater with the paint vessel inside. A metal skeleton is attached to the coater to hold transparent PVC sheets creating a makeshift fume hood.

coater velocity v_{coater} for the big tube of 4.8 $\frac{\text{cm}}{\text{min}}$. Since the coater only allows a fixed set of velocities the nearest one with 5.64 $\frac{\text{cm}}{\text{min}}$ is chosen. Previous measurements in [86] indicated, that an increase in velocity only increases the paint thickness and thus the efficiency. A more detail description of the coating process, as well as the preparation of the tube for coating, can be found in section A.4.3.

$$v_{\text{real}} = v_{\text{coater}} \frac{A_{\text{vessel}}}{A_{\text{vessel}} - A_{\text{tube}}} \tag{5.26}$$

5.4.2 Cast vs. Extruded Tubes

For tubes with 9 cm diameter, two different types of manufacturing processes are available that might influence the optical properties. There are extruded and cast tubes. The extruded tubes are squeezed through a tube sized nozzle and then cooled down quickly. The extrusion process is well suited for large scale productions. The fast cooling process causes more thermal tension than slower methods. This might be compensated for by tempering the tube afterwards. In the tubes used, it was found that the surface always showed small streaks, probably caused by the nozzle. For the cast tube, a mould is used. For the production, the monomer (methyl methacrylate) is mixed with initiators and placed in the mould. To form the tube, the mould is rotated with high velocities during the hardening process. Afterwards, the cast is cooled down slowly. This produces a smoother surface and generally produces better optical properties. However, tolerances in the wall thickness are much larger. In our case, the tolerances for a 3 mm wall thickness are ±1 mm.

The tubes used until this point have all been extruded since cast tubes are not available in small diameters. To directly compare them one 9 cm diameter and 90 cm long tube of each type has been coated with WLS paint. Since small local impurities might influence the result it was decided that a measurement involving many points along the length of the tubes is most reliable. Since PMT measurements take a significant amount of time and were not automated at the time of the measurement a PD measurement with a portal robot that was available for that setup, seemed the best option. The discrepancy in the PD acceptance will only be a minor systematic effect since both tubes only need to be compared in relative not absolute efficiency.

This updated setup is based on the one described in section 5.1.1 and shown in fig. 5.1. Several devices have been added to the setup and a multifunctional DAQ system has been developed for this. A more detailed description of the extensions, the software and the usage can be found in section A.4.5. For the measurement here it is only important, that a portal robot was added as shown in fig. 5.18 (right). Here it automatically moves the light source to predefined locations along the tube to measure the relative efficiency as a function of both, position and wavelength. The PD is shifted by $\frac{\pi}{2}$ along the curvature of the tube, relative to the light source as illustrated in fig. 5.18 (left). This reduced contributions from direct light on the PD.

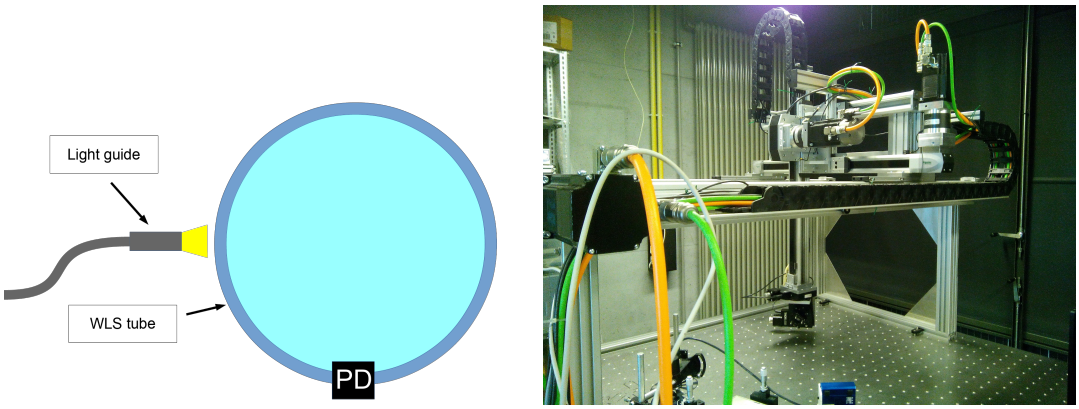

Figure 5.18: (left) The orientation of PD, Light source and tube during a measurement.(right) Picture of the portal robot with two rotational stages on the head.

The results of the measurement for an extruded tube (XT) and a cast tube (GS) are shown in fig. 5.19. The cast tube was measured from both ends, therefore the mean value of both measurements is used. The plots are for a wavelength of 360 nm. The measurements for the other wavelengths are more or less identical with different overall amplitudes. The results are scaled according to the approximate area of the tube end that is covered by the PD according to eq. 5.27. Here r is the radius, w the wall thickness of the tube and a the width of the PD.

$$\sigma = \frac{2\pi\left(r - \frac{w}{2}\right)}{a} \tag{5.27}$$

The extruded tube does not just have a lower efficiency, but it also falls off faster with distance. The lower efficiency might be caused by the quality of the optical coupling or other systematics. The fast decrease in efficiency however shows that the light-guiding properties of the cast tube are superior to the extruded. This may be caused by the streaks from the manufacturing process on the surface of the extruded tube or by a generally worse optical quality of extruded tubes [111].

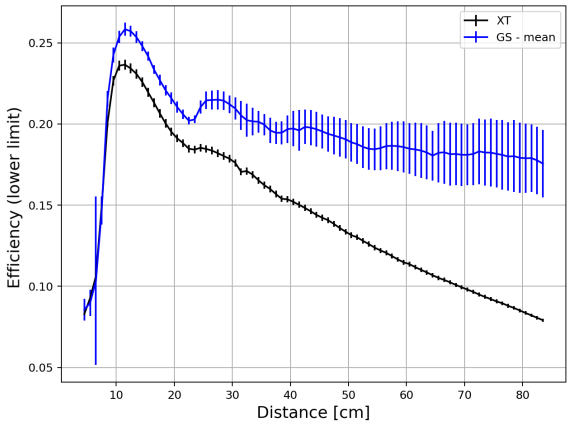

Figure 5.19: Position dependent relative efficiency comparison between an extruded (XT) and a cast (GS) tube, as a function of light source position along the tube, relative to the PD.

The measuring of both tube ends for the cast tube was originally intended as a cross-check, yet it revealed a discrepancy in the results measured on the same tube. The individual measurements are shown in figure 5.20. As it can be seen, the rotated tube also differs in transport loss. Since the effect is smaller than with the extruded tube, it appears still the better option to use the cast tubes. The reason for this could be the variation in thickness along the length of the tube, from the manufacturing process. Alternatively, the different time the bottom and the top of the tube are exposed to the solvent in the paint during the coating process might have an effect as well. This was not further investigated, but it is recommended to follow up on this once an automated PMT measurement setup is available. For the following measurements, only cast tubes are used. The difference seen here should be considered a systematic in future measurement. Additional investigation is recommended.

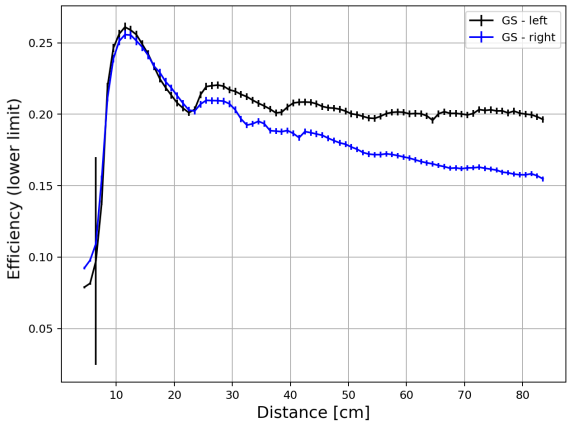

Figure 5.20: Position dependent relative efficiency comparison of a GS tube readout on the left and the right, as a function of light source position along the tube, relative to the PD.

5.4.3 Optical Prototype Efficiency

A few initial measurements with different PMTs that cover only part of the tube ends have been done. Large fluctuations and large uncertainties have been observed, with generally much lower efficiencies. A PMT large enough to measure the whole area of a tube end was not available at this point. Therefore and to test the adiabatic light guide a full optical prototype with adiabatic light-guides was assembled and measured.

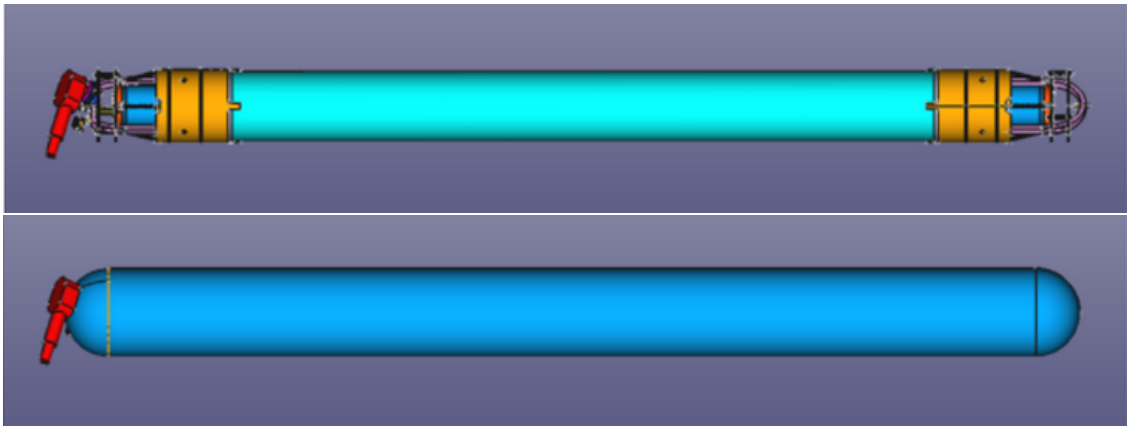

Figure 5.21: CAD-image for a fully assembled WOM without (top) and with (bottom) pressure vessel. These images were created by the technical workshop at DESY Zeuthen.

The full optical prototype consists of a coated 9 cm diameter PMMA tube, glued to an adiabatic light-guide on each side. This structure is connected to a PMT holding-device including the 80 mm diameter hemispheric PMT[18] and a spacer made from O-rings. The combined setup is placed in a pressure vessel. Schematic views of this are shown in fig 5.21 and the final prototype in fig. 5.22. A UV-curing glue[19] has been used to attach the adiabatic light guides to the WLS-tubes. The optical properties of this connection seemed insufficient, as can be seen (in fig. 5.23) there is a significant amount of light scattered at the connection between adiabatic light-guide and tube. The light guides used were made by the local workshop. They were milled and polished, however, faint streaks remain visible that likely impact the light-guiding efficiency. Another set made by Kümpel Kunststoff-Verarbeitungswerk GmbH, that showed on visual inspection a much higher quality, were not tested due to their higher price.

The efficiency was measured with both PMTs simultaneously while the pressure vessel and the PMT holding structures are not in place yet. For that the PMT was held by external structures as shown in fig. 5.22 (top) and the 370 nm light source pointed at the center between both PMTs. The result is a combined efficiency of 13.0 ± 5.5 %. This is based on 6.8 ± 3.3 % for the left and 6.2 ± 2.2 % for the right PMT. For this only, the one-sided efficiency $\frac{\epsilon_{\mathrm{WL}}}{2}$ is used and the scaling factor of 2 is removed. For both values, the cut method has been used. Observing the PMT signal on the Oscilloscope before and after the measurement showed an unusually large amount of noise. It was assumed that this is caused by cross-talk between both PMTs. Therefore the measurement was repeated measuring only the right side. Once again in the SPE range with the cut method resulting in an efficiency of 7.7 ± 1.6 % and once in the dynamic range with an efficiency of 6.3 ± 0.1 %. In both cases, the noise rate (observed on the

[18] Hamamatsu R12199-02
[19] UV-härtender Klebstoff BEST-PL 5373 from BEST-Klebstoffe GmbH & Co. KG

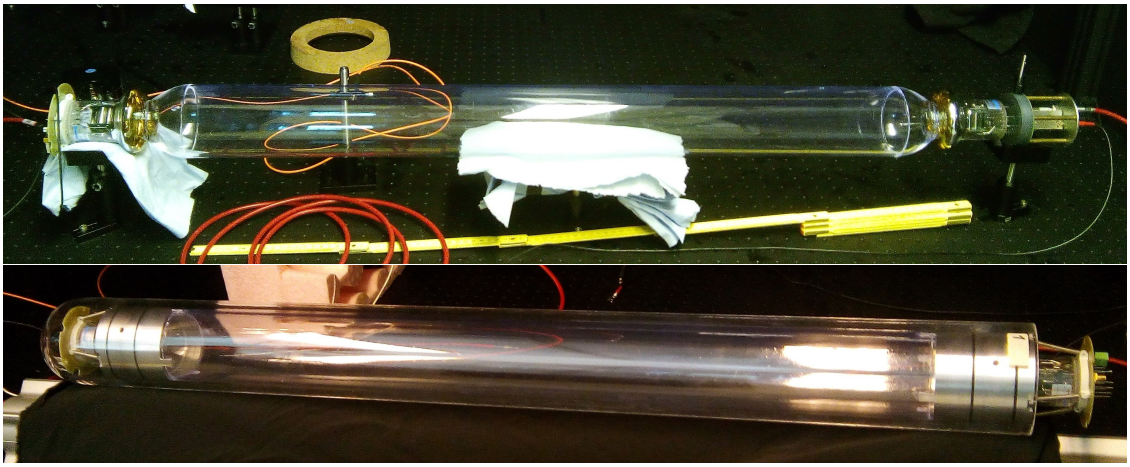

Figure 5.22: Assembled WOM without (top) and with (bottom) pressure vessel and PMT holding structure. In both images, the electronics board, except the voltage divider is still missing.

oscilloscope) appeared lower than before, yet the results remain consistent. The measurement was also repeated with the pressure vessel and PMT holding structures in place. Since the PMTs are difficult to remove from the holding structures a third identical PMT was used for the reference measurement. Unavoidable manufacturing differences between the different PMTs increase the systematic for this measurement. All PMTs were run with the same supply voltage of a 1000 V. Besides the sample and reference measurement, a dark measurement was recorded for each PMT. For each measurement $\langle n \rangle$ was calculated based on the second model-independent evaluation approach (described by eq. 5.25) to account for differences between the PMTs and ADC channels. Using eq. 5.14 the results for the one-sided efficiency $\frac{\epsilon_{\mathrm{Wt}}}{2}$ are 9.3 ± 1.1 for the left and 3.8 ± 1.8 for the right PMT. Based on [112] the difference in quantum efficiency for the Hamamatsu R12199-02 at 370 nm, can be as much as 17 % between different PMTs of the same type. Also, the PMT holding structures are glued to the WLS tube, creating a way for photons to scatter. In total, the number of systematics from the equipment, the newly introduced components and the evaluation techniques comes close to the measured value. It has become clear that the efficiencies on large tubes with adiabatic light guides are much lower than on the small tubes. To investigate this further, a more detailed look into the performance of the constituents is necessary.

5.4.4 Improved Measurement Setup for Efficiency Measurements

When new smaller PMTs with 25 mm diameter (type R1924A from Hamamatsu [113]) and the new data acquisition system (ADQ14)[20] became available, more accurate and extensive measurements were possible. With the small PMTs several could be used simultaneous and changes in gain as a function of photocathode position became negligible. The ADQ14 allowed higher data taking rates and storage of whole waveforms, instead of their integrals, as it is done by the ADC that was used before. Additionally, many previously described problems with the data acquisition disappeared. The measurements and their iterative improvement, as well as their results, will be described in the following. Due to a lack of an optically sufficient glueing technique and the additional uncertainty from its usage, the adiabatic light guides were not included for the time being.

[20] 4 channel 14-bit digitizer, ADQ14 with 1 GSPS sampling rate and USB3.0 [110].

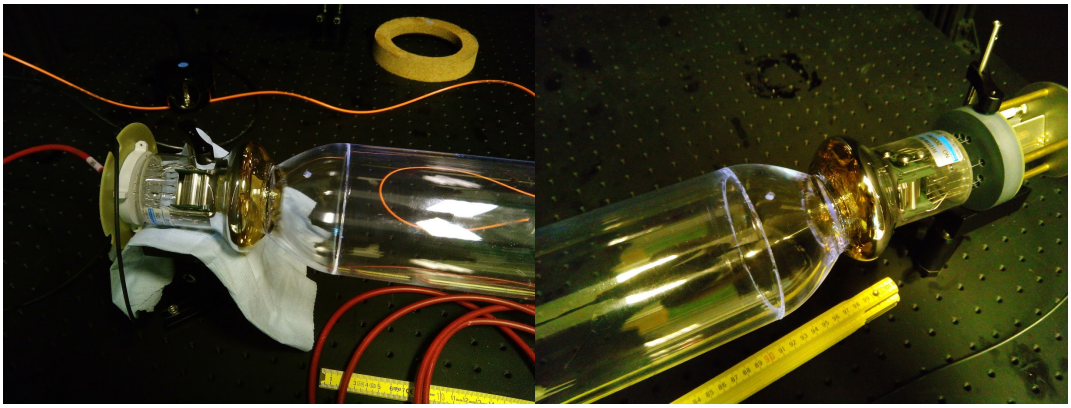

Figure 5.23: Adiabatic light guides glued to both ends of a tube and readout with a PMT. The small blueish reflection in the middle of both light guides is a small hole for cables to be feed through.

Experimental Setup

With the new equipment, a slightly modified measurement setup, as described in the following, has been assembled to evaluate the large WLS tubes. With it a measurement was performed on a 9 cm diameter PMMA tube with a wall thickness of 3 ± 1 mm. On the tube, an outside paint layer had been applied with a coating velocity of 9.24 ± 0.06 $\frac{\text{cm}}{\text{min}}$. It was placed in the PMT measurement setup as shown in fig. 5.24. On one side a black absorber was coupled to the tube with optical gel (left). On the other side, three round PMTs with 22 mm diameter sensitive area were attached with optical gel. The positioning of the PMTs is illustrated in fig. 5.25. To obtain the data, the light from a 370 nm pulsed LED is guided via optical fiber to the setup. After a reference and dark measurement for each PMT, the fiber is moved along the length of the tube with measurements taken every 2 cm, as illustrated in fig. 5.24 with perpendicular illumination. The trigger for the LED also triggers the simultaneous readout of all three PMTs in form of a 512 ns long waveform.

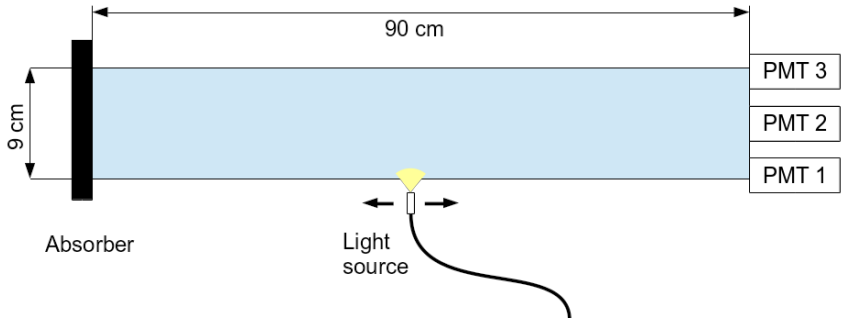

Figure 5.24: Schematic view on the measurement.

For the efficiency measurement, the individual waveforms are integrated over the relevant 60 ns window and histogrammed to a charge distribution. This charge distribution is then evaluated with the model-independent method to determine the efficiency. This method was chosen for several reasons. Due to the large tube diameter and small PMT diameter, the reference measurements are in the dynamic range while the sample measurements are in the SPE range. The model-independent method is the only method that supports this configuration without modifications. Also, the smaller diameter of

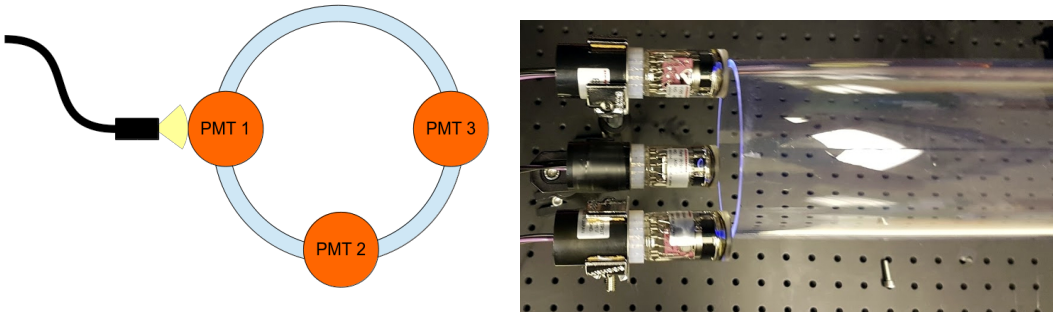

Figure 5.25: (left) Schematic view on the tube edge with the PMT arrangement and their corresponding numbers. (right) A picture of the actual setup.

the PMTs is assumed to reduce the position-dependent changes in gain, thus reducing the previously larger systematics for this method. Lastly, the data quality improved significantly with the new devices. This is mostly due to the possibility of screening the individual waveforms for irregularities and better adjustment of the relevant time frame. Previously seen, strong fluctuations in the obtained results were not observed any more. Nevertheless, this comprehensive dataset allows for a comparison of the different evaluation techniques, which was done as well with slight modifications to account for the reference measurement being in the dynamic range.

Since the new ADQ stores the whole waveform instead of just the integrated charge, it is not just possible to reduce the noise by more precisely selecting the relevant time frame, but also extract the timing information from the same measurement. To obtain the timing information from that data, each waveform is scanned, front to back, with a ≈ 0.5 SPE threshold. If a peak is larger than the threshold, the time of the threshold crossing is recorded in a histogram. An example of such a histogram is shown in fig. 5.26. The histogram represents the time resolution of the WLS tube for photon detections at a specific point on the tube.

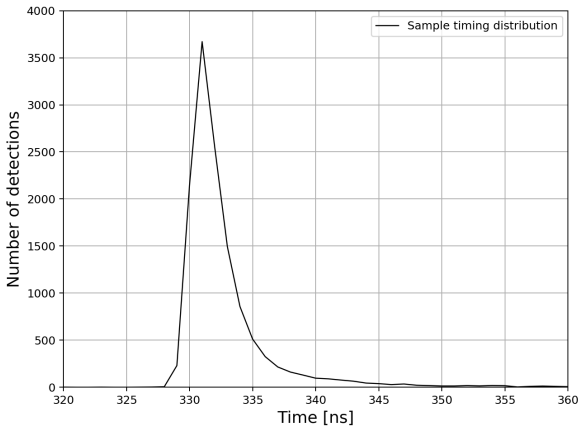

Figure 5.26: An exemplary photon arrival time histogram with ns resolution and binning. The line representation is chosen to improve readability in cases where multiple histograms are combined.

Efficiency and Distance Dependence

The efficiency measured at each PMT is shown in fig. 5.27 as a function of light source position along the tube. For the calculation of the efficiency, the model-independent method has been used. Using the new ADQ and small PMTs the results are more stable than before. For small distances between light source and the end of the tube, where the PMTs are attached, the efficiency behaves as expected. For the PMT with a line of sight to the light source, the efficiency exceeds unity due to the geometric scaling factor σ_{cor}. The efficiency of the other two PMTs decreases as the radial distance on the tube to the light source increases. For distances of the light source that are larger than 30 cm the light is equally distributed in the tube and all PMTs see similar amounts of light. The behaviour between 10 and 30 cm distance is not clear. Especially the reason for the peak from PMT 2 is unclear. It is suspected that this is caused by direct illumination of the PMT from the light source or reflection of the light in the tube. It further becomes clear that the efficiency on the large tubes is much lower than assumed from the measurement on the small tubes.

For small tubes the efficiency for 370 nm at 27 cm distance to the light source was measured to be 50 ± 3 %. At the same wavelength and distance to the light source it is only 26.4 ± 4.2 % for the larger tubes. A clear reason for the differences was not determined. The different geometry might explain part of the difference. Since the small tube is shorter (30 cm) the probability that light from the end of the tube that faces away from the PMT is reflected and detected is much higher. While it was verified that the use of the black absorber at that end reduces the measured light intensity, it was not verified that no light is reflected. Further more the wall thickness to tube diameter ratio is larger for the small tube. This reduces the number of reflections for a photon that circulates around the tube. The small tubes were also coated with WLS paint from the inside, which is not yet possible for the large tubes. Beyond that, the tubes are also purchased from different manufacturers. These are physical difference between the tubes that might explain the difference. There are also differences in the equipment used to make these measurements. Especially the measurements with the ADC setup, that was used for the measurements with the small tubes, always had a tendency to produce errors, as for example the unstable base value (described in section 5.2.3) or the insufficiently shielded cables, might have played a role.

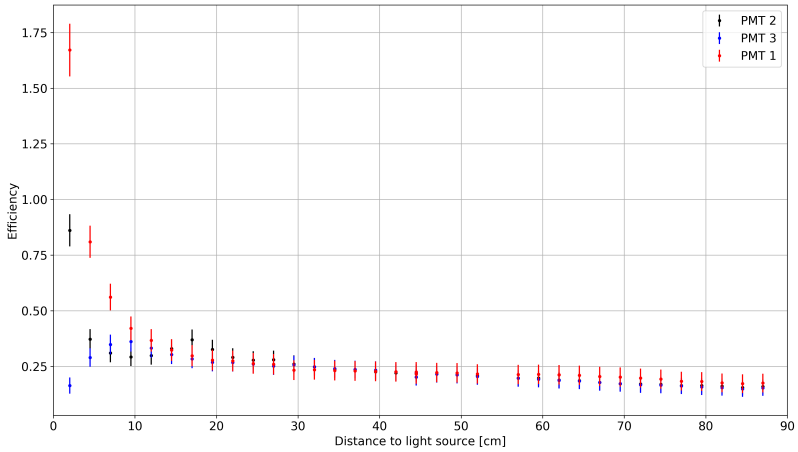

Figure 5.27: Position dependent efficiency with 3 PMTS on WLS-tube coated with a 9.24 ± 0.06 $\frac{\text{cm}}{\text{min}}$ withdraw speed. The value at 54.5 cm distance was not measured.

Comparison of Different Evaluation Techniques

To approximate the efficiency for the whole tube based on the small PMT measurements an average can be used according to eq. 5.28. PMT 2 is weighted with a factor of two due to the symmetry of the tube.

$$\epsilon_{\mathrm{Wt}} = \frac{\epsilon_{\mathrm{PMT1}} + 2 \cdot \epsilon_{\mathrm{PMT2}} + \epsilon_{\mathrm{PMT3}}}{4} \tag{5.28}$$

This average is shown in fig. 5.28 with the label "Model-Indep.". To qualitatively compare the different evaluation techniques described earlier with a single measurement, the most relevant ones have been selected and calculated as well. Considered most relevant are the cut and improved fitting (NGauss) method as well as the partial fitting method (2Gauss+Exp) for legacy reasons. Since none of these methods is can natively account for the reference measurement in the dynamic range, a few adaptations have been made. For the cut and improved fitting method, the following has been done. To obtain $\langle n_{\mathrm{reference}} \rangle$ for the reference measurement, the gain G is obtained from each available sample/SPE measurement with the method suggested in [109]. From the mean of the reference measurement data points $\mu_{\mathrm{reference}}$, $\langle n_{\mathrm{reference}} \rangle$ can be calculated according to eq. 5.29, using the weighted average of all obtained Gs.

$$\langle n_{\mathrm{reference}} \rangle = \frac{\mu_{\mathrm{reference}}}{\langle G \rangle} \tag{5.29}$$

This specifically means, that both versions of the model-independent method, as well as the SPE measurements, are used to obtain a reference. Therefore the comparison of these methods is not completely independent from one another. To determine $\langle n_{\mathrm{sample}} \rangle$ the previously described calculations for the cut and improved fitting method are used. For the partial fitting method (2Gauss+Exp) the gain G is obtained from the distance of the left most SPE-Gauss (eq. 5.19 and 5.30) to the mean of the dark measurement μ_{dark} (eq. 5.31). The calculation of $\langle n_{\mathrm{reference}} \rangle$ is performed according to eq. 5.29.

$$\mu_{\mathrm{SPE}} = \min \{\mu_1, \mu_2\} \tag{5.30}$$

$$G = \mu_{\mathrm{SPE}} - \mu_{\mathrm{dark}} \tag{5.31}$$

The results as seen in fig. 5.28 and table 5.1 illustrate the different properties of the evaluation techniques. The model-independent, the cut and the improved fitting (NGauss) method are compatible with one another. The model-independent method evaluates the results on a purely statistical basis and assuming no systematics like fluctuating gain or non-linear noise contributions, should be most accurate. This is especially the case because also under amplified photo-electrons are taken into account. The cut method is least discriminating concerning pedestal, under amplified photoelectrons and SPEs. This is reflected in the larger error that is based in the empirically determined cutting accuracy.[21] The improved fitting method describes the SPE histograms well, which is reflected lower statistical error calculated from error propagation. Yet the underlying model does not account for under amplified photo-electrons, which are more likely to contribute to the pedestal with this model. For this reason, a higher systematic is to be assumed, which is consistent with the other results. The partial fitting method (2Gauss+Exp) excludes under amplified photo-electrons since they are described with the exponential function, that does not contribute to the SPE-integral. Based on this the efficiency determined with this method should be smaller than the other methods, however, due to the gain being determined based on the position of the first Gauss this is not the case. Due to MPE contributions as well as the exclusion of

[21] Here and for all ADQ14 measurements the value is set to 3 bins.

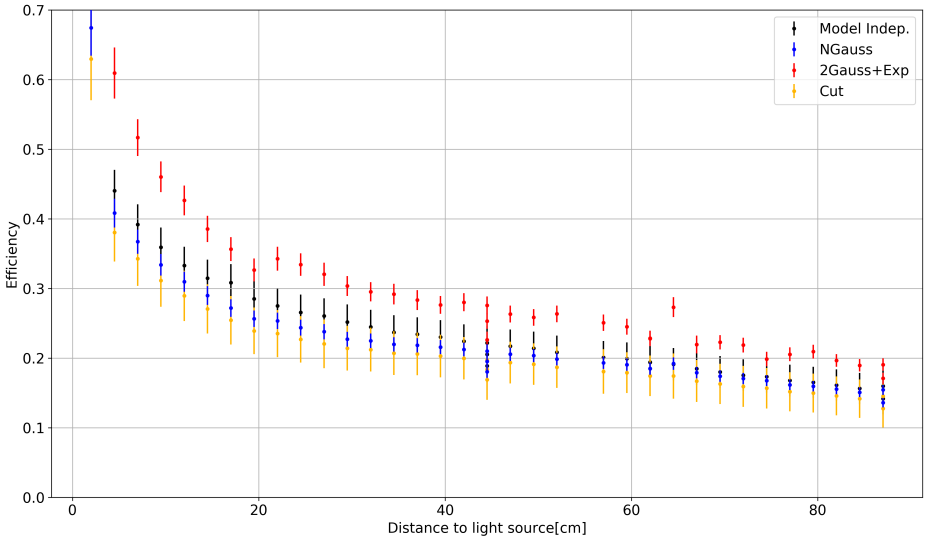

Figure 5.28: The position-dependent efficiency for the weighted mean of 3 PMTS on the same tube used for the values in fig. 5.27. Compared are different evaluation techniques to determine the efficiency.

Method	$\langle \epsilon_{\mathrm{Wt}} \rangle$ [%]	$\langle \Delta\epsilon_{\mathrm{Wt}} \rangle$ [%]
Model-Indep.	24,4	2.5
Cut	21.5	3.2
NGauss	22.9	1.1
2Gauss+Exp	28.6	1.4

Table 5.1: Mean efficiencies over all distances and their error for different evaluation methods.

under amplified photo-electrons, the distance between pedestal and SPE is overestimated, increasing the determined efficiency. The partial fitting was a first attempt to describe the data obtained from this kind of measurement and should not be used due to the inaccurate determination of the gain. It is shown here because these values have been used for the simulation in chapter 7. Appropriate corrections for this will be applied there. It is therefore recommended to use the model-independent method whenever possible. On large photocathodes, possible gain changes as a function of light detection position on the photocathode need to be corrected for. While the cut method produced more consistent results on data with not well-described noise, the additional systematic uncertainties negate any gains from the cut method. The NGauss method can be used as a fallback solution for PMTs with few under amplified photons.

Comparing this to the measurement with the adiabatic light-guide, it can be assumed that about half the light is lost when using the adiabatic light-guide.

Comparison of Different Coating Speeds

A determination of the optimum coating speed for small tubes and microscope slides has been performed in [86]. To validate these results for large tubes, measurements for selected coating speeds on large tubes have been performed as well (shown in fig. 5.2). To be able to measure all data points after

Coating speed $\frac{\text{cm}}{\text{min}}$	44.5 cm		87 cm	
	ϵ_{Wt} [%]	$\Delta\epsilon_{\text{Wt}}$ [%]	ϵ_{Wt} [%]	$\Delta\epsilon_{\text{Wt}}$ [%]
5.6	23.8	2.5	18.5	2.4
8.0	22.2	2.4	16.0	2.2
18.5	23.0	2.5	17.3	2.4
53.0	27.5	2.6	18.9	2.4

Table 5.2: Efficiencies measured for different coating speeds and distances to the light source.

one another with little to no change in the setup, only measurements at 44.5 cm and 87 cm, along the 90 cm tube, were taken. The results are shown in table 5.2. At 44.5 cm and coating speeds between 5.6 and 18.5 $\frac{\text{cm}}{\text{min}}$ no significant difference can be observed. The same is true for the measurements at 87 cm distance. Only the measurement at 44.5 cm for 53.0 $\frac{\text{cm}}{\text{min}}$ shows an increase in efficiency. This value is much higher than the previously, for small tubes and microscope slides, determined 8 $\frac{\text{cm}}{\text{min}}$. For small tubes, there are four paint layers[22] the light can potentially be absorbed in. For the large tubes that are only coated on the outside, there are just 2 layers.[23] However, the absorption measurements, with the microscope slides that also only have two layers, indicated this would suffice. To exclude systematic errors caused for example by the tube orientation or statistical fluctuations, the measurement was repeated. The results were for an unknown reason generally up to 3 % lower but the efficiency for the 53.0 $\frac{\text{cm}}{\text{min}}$ tube remained higher in comparison. Both times the same tubes were measured, therefore systematics concerning the individual tubes can not be excluded as a reason for the differences. Since no negative effects, such as a visibly degraded paint surface,[24] due to the faster coating speed were observed, the larger coating speed will be used for future measurements.

Timing

The timing histograms for PMT 1 at representative distances are shown in fig. 5.29. Depending on the position the width of the distributions is between 3 to 5 ns with a long tail. For short distances, the distribution is dominated by the decay time of the WLS. At larger distances, an additional component for different possible photon paths widens the distribution. The cumulated full width half maximum (FWHM) over the whole tube is ≈ 8 ns. The measurements from the other PMTs are comparable with slight position and cable-related time offsets.

5.4.5 Revision of the Improved Measurement Setup

Based on the experience made with the previous measurement several improvements have been made. On the tube, an outside paint layer has been applied with a faster coating speed of 53.0 ± 0.6 $\frac{\text{cm}}{\text{min}}$, since a better absorption might be achieved this way. The paint surface showed a few impurities of $1-2$ cm extent but was generally considered usable. The tube was placed in the measurement setup with four PMTs instead of three as shown in fig. 5.30 and fig. 5.32, this allows a better estimate of systematic effects, since with the given configuration two of the PMTs should see identical results. The inside of the tube in front of the PMTs is blocked with a piece of cardboard and the outside is covered with a piece of cloth, to avoid direct light that is not transported in the tube to reach the PMTs. On the other

[22] Considering an outside and inside coating on both sides of the tube.
[23] An outside layer on each side of the tube.
[24] This was previously observed on smaller tubes.

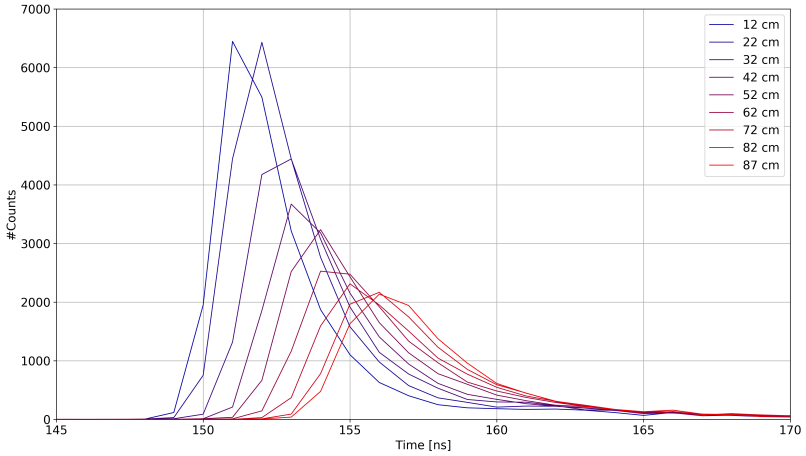

Figure 5.29: Timing distribution as measured for PMT 1 at different distances with ns binning and resolution.

side, a black absorber was coupled to the tube with optical gel as shown in fig. 5.31 (left). A picture and a schematic of that can be seen in fig. 5.31 (right). To obtain the data the light from the 370 nm pulsed LED is guided via optical fiber to the setup (fig. 5.30). After a reference and dark measurement for each PMT, the fiber is pointed again at different positions along the tube as illustrated in the figure. The trigger for the LED also triggers the simultaneous readout of all four PMTs as a waveform of 512 ns duration, including a pre-trigger time of 64 ns.

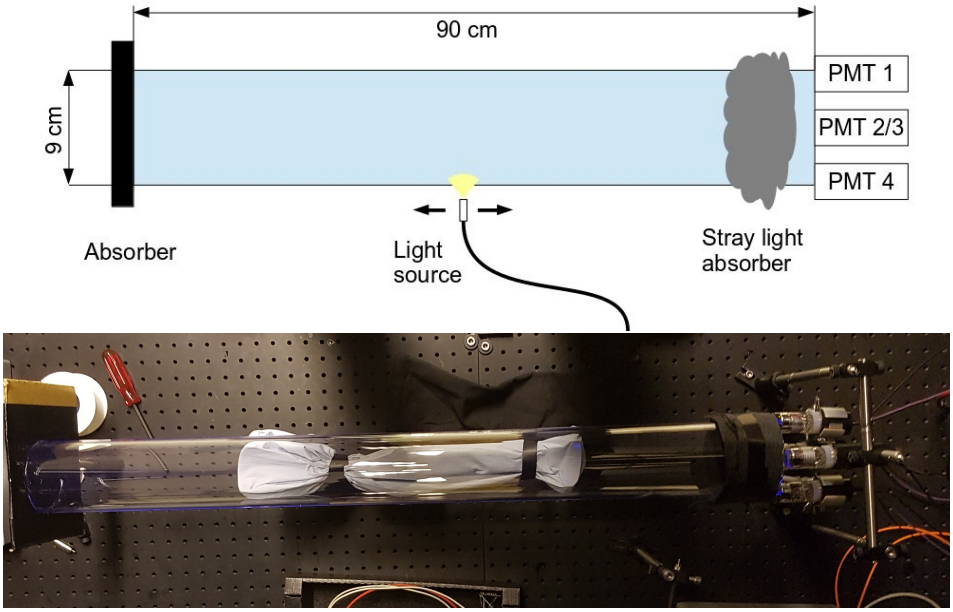

Figure 5.30: (upper) Schematic view on the measurement. (lower) Picture of the actual setup.

For the efficiency measurement, the individual waveforms are integrated over the relevant 60 ns window and histogrammed. This histogram is then evaluated with the model-independent method to

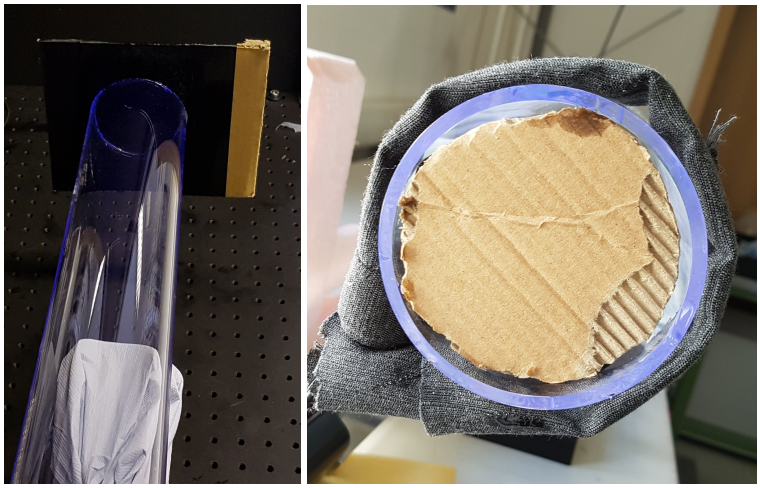

Figure 5.31: (left) Cardboard absorber covered with black tape and optical gel for better light absorption. (right) Readout end of the tube without PMTs, showing a cloth around the tube for stray light absorption and a piece of cardboard in the center for the same purpose. The other side of the cardboard is also covered with black tape.

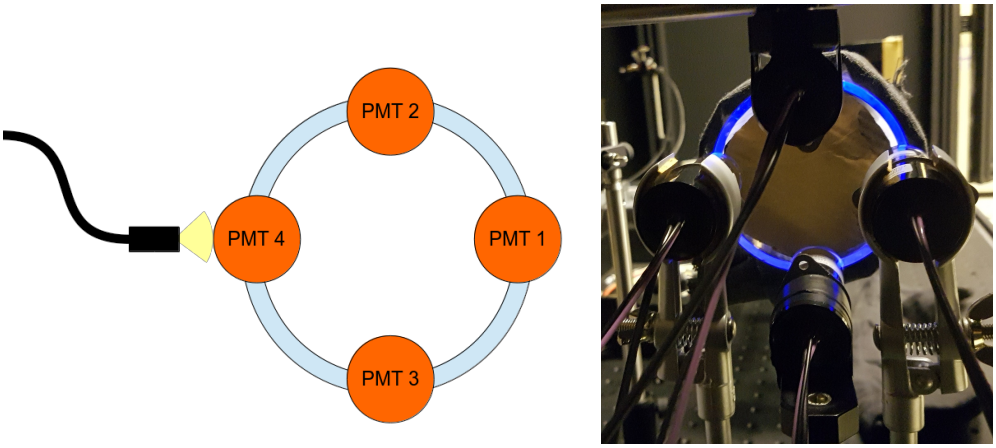

Figure 5.32: (left) Schematic view on the tube edge with the PMT arrangement and their corresponding numbers. (right) A picture from the same perspective as the left schematic.

determine the mean number of photoelectrons, its error and the corresponding efficiency. The result is shown in fig. 5.33. This is consistent with the previous measurements with slightly higher efficiency that can be attributed to the faster coating speed. The average efficiency overall PMTs and the entire length is 28.1 ± 0.5 %. PMT two and three are in symmetric position relative to the light source and should therefore see identical readings. Yet the values are not compatible with respect to the statistical uncertainties. This is again an indicator that there are underlying systematic uncertainties that are not accounted for. Since the effect is seen overall distances, the systematic is likely related to either the reference measurement from one of the PMTs or some physical difference at or near the interface of tube and PMT. There were no irregularities found in the reference measurement. Differences near the interface of tube and PMT might be an imperfection in the tube near the PMT or with the optical coupling of PMT and tube. In previous measurements, it was seen that reattaching a PMT at a different position on the tube while keeping the relative geometric position of PMT and light source the same, similar fluctuations occurred. Therefore the source of this difference is likely the optical coupling or

some unknown properties of the tube near its end.

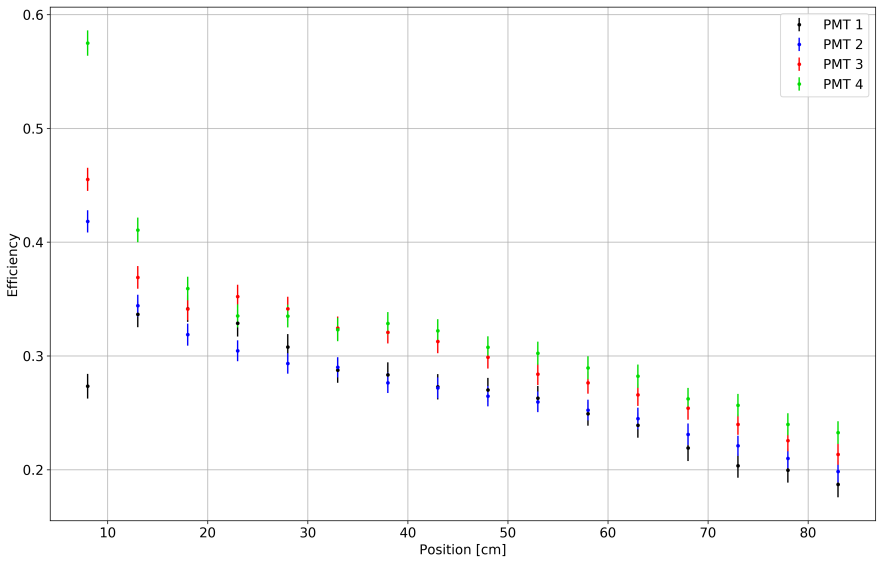

Figure 5.33: Efficiency distribution simultaneously measured with four small PMTs on one tube.

5.4.6 Timing Behaviour

To obtain the timing information from that data, each waveform is scanned within a relevant 70 ns window with a ≈ 0.5 SPE threshold. If a peak larger than the threshold is found the maximum of that peak is determined and the time where the peak reaches $\frac{1}{3}$ of the maximum is recorded in a histogram.[25] The first 10 ns are in an unphysical regime and are used to determine the noise rate that is then added to the statistical error. The additional error is typically between 1 to 2 counts per bin on average, depending on the PMT. The results for PMT 4 are shown in fig. 5.34. On the left side, the histogram of the individual timing distributions is shown as before. The difference in amplitudes in comparison to fig. 5.29 correspond to the different location of the PMT. Beyond that, there is no significant difference to the previous measurements. On the right side, the timing distributions are summed as a function of light source distance. This means the distribution for 8 cm distance is the same in both plots. The distribution for 13 cm distance in the right plot is the sum of the 8 and 13 cm distribution in the left plot. The resulting distributions approximate of the timing behaviour for a WLS-tube with the corresponding length.

Relative to the light source, PMT 2 and 3 are positioned symmetrically to each other, therefore they show the same timing behaviour. This assumption is tested in fig. 5.35. To account for the difference in efficiency measured all distributions are normalized to 1. Overall the distributions match with one another. Due to the large statistics and the corresponding low statistical error, the peaks of the distributions at 8 cm distance are not consistent within the given error. However, the ADQ14 only has a ns resolution, that corresponds to the binning used here. Any offset in timing due to the electrical setup can only be corrected up to 1 ns. Therefore a sub ns offset could explain the difference.

[25] Effectively making this a constant fraction discriminator.

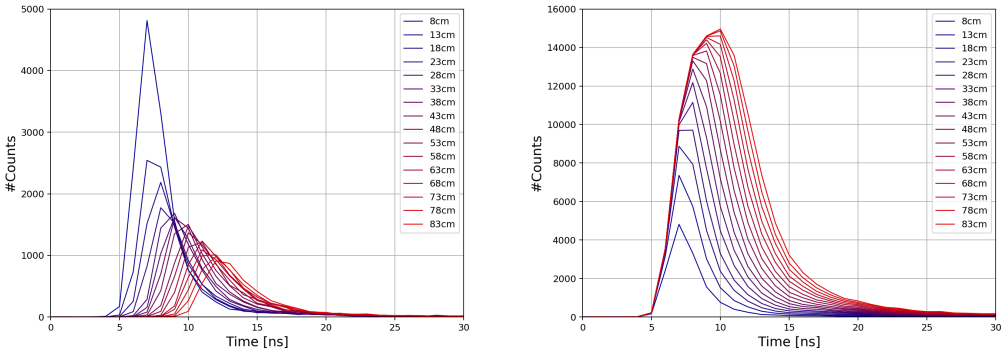

Figure 5.34: Timing distribution as measured for PMT 4 for different distances with ns resolution and binning. (left) Individual distributions. (right) Distributions cumulated over distance.

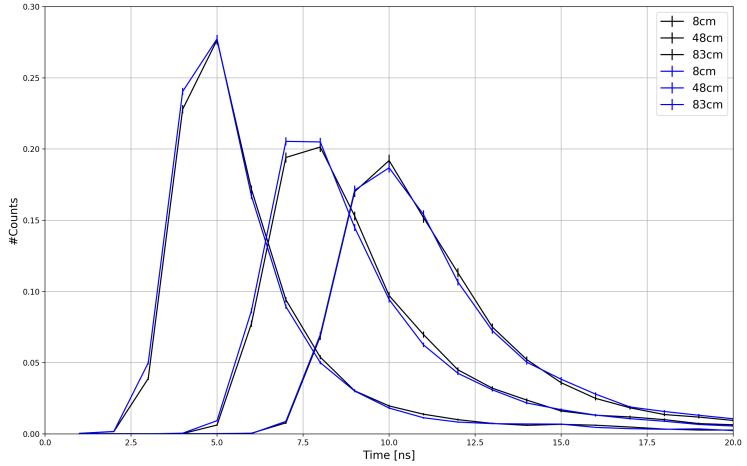

Figure 5.35: Comparison of normalized timing distributions for PMT 2 and 3, for three representative distances with ns resolution and binning.

5.5 Systematic Errors

With the work presented in this chapter, it became evident that the efficiency measurements of the WLS tubes contain many systematic effects. This section will describe them mostly qualitatively. A quantitative description would be preferable but is not always feasible in the context of this thesis. The reasons for that are hardware and time constraints. For example, a thorough scan of a photocathode requires at least $O(100)$ measurements and precise positioning of the light source. With the original equipment a single measurement takes between 20 and 120 minutes and light source positioning is done by hand. It becomes evident that even a single photocathode scan requires a significant amount of time. Several of those would be necessary just for the different PMTs used in this thesis. A similar if not larger efforts would have to be undertaken to scan an entire WLS tube. This was not considered an efficient use of time and manpower. This has been changed with a new setup including the ADQ14 as well as a portal scanner. However, the latter has not become available while the measurements in

this thesis were performed. First steps with this equipment towards understanding the systematics have been done in [114].

5.5.1 Systematic Errors from the PMT and the Evaluation

In section 5.2.3 sources of systematic errors during the PMT-data evaluation were already described, among them: unstable base value, additional peaks, spacial uniformity of PMT gains, and evaluation techniques for the PMT measurements. Where the first two apply only to the old setup. Further systematics will be discussed in this section.

Acceptance Angle of PMTs

In a WOM like setup, light can reach the photocathode under uncommonly large angles. Without coupling to a higher refractive index material photons can not reach the cathode under these angles. Without optical coupling and assuming isotropic distribution only $\approx 25\,\%$[26] of the light captured in the tube would leave the tube at both ends. The optical coupling extends this to $\approx 75\,\%$. The additional $50\,\%$ hit the cathodes under very steep angles at which the acceptance of the PMT is not well known. The distribution of light in the WLS-tube was already determined in [115] and is briefly described in section A.2.3. Based on this it can be said that the light is not uniformly distributed and at least in the orientation measured, a significant fraction is distributed within an angular range that PMTs are not exposed to without the optical coupling. The angular sensitivity of the PMTs was not measured and only the combination of the light distribution at the end of the WLS-tube and the PMT angular sensitivity would allow for a correction of potential losses here. The size of this potential effect is unknown and is therefore not corrected for, in the measurements shown.

Optical Coupling of the PMTs

Perfect optical coupling with the optical gel used in this experiment is difficult to achieve. Significant amounts of pressure can change this but this is not advised due to the fragile nature of the PMTs. The reason for those imperfections is inhomogeneity in the gel distribution and optical surfaces. The result is small air gaps. Estimated from visual inspection, they cover from 5 to 30 % of the optical surface coupling by default and thus increase reflectivity and reduce the light transmission. Actively trying to reduce this effect, by better spreading the optical gel, twisting and moving the tube relative to the PMT before the measurement, has reduced this value to about 10 % or less, by visual estimation for the measurements performed.

Additional Position Effects for PMTs

In the measurements taken in this thesis, the calibration measurement for the PMT is always taken in the center of each PMT. The WLS-tubes, however, are sometimes measured with a certain distance to the center of the PMTs due to geometric constraints. As observed in fig. 5.14, the gain of a PMT is not equal at all positions. While in that particular case the sensitivity was mostly homogeneous over the scanned surface, this is not the case for all PMTs. A more detailed sensitivity scan of a Hamamatsu R12199-02 is shown in 4.10 (right). This shows that for this particular PMT a discrepancy of the order of 10 % can be expected. Larger fluctuations of individual measurements in this plot are likely

[26] This is based on the same calculations made in 4.3.4.

of statistical nature. A more detailed description and calculation for a particular case can be found in [114]. In a similar manner distribution of light in the tube might have an effect as well.

Linearity

The linearity of the photoelectron response was not individually measured for each measurement and PMT. The linearity depends mainly on the used gain and PMT type. A representative measurement with one Hamamatsu R12199-02 was done. The light intensity for two individual LEDs and the combination of both LEDs was measured with various amplitude combinations and resulted in a deviation of $1,2 \pm 0,3\,\%$ for a change of intensity by a factor of two.

5.5.2 Uncertainties from the WLS Tube

Geometric Tube Properties

While not strictly a systematic error, the tube geometry is likely not always homogeneous. This can be seen in fig. 5.20, in this particular example it changes the outcome of the measurement by up to 25 % for the largest light source distances. The same is probably true for the surface quality. Fig. 5.19 is a good indicator for that.

Paint Quality

The surface quality of the paint has been shown to fluctuate. This can be due to small uneven structures formed in the coating process or insufficient paint thickness. Once it is possible to scan the surface of a tube with high resolution in a reasonable amount of time those structures will be easier to identify and quantify their effect. Since this is not the case yet, a few percent error should be kept in mind for this. Additionally, the paint layer thickness appears to behave differently on various materials. On smaller tubes (4 layers) and microscope slides (2 layers) 100 % absorption was reproducibly measured. For the bigger tubes (2 layers), the same coating speed does not produce the same results. Further investigation is required.

Light Distribution

As previously shown the light distribution in large tubes is not isotropic, thus scaling errors may occur if not the whole surface at the end of the tube is readout.

5.5.3 Minor Systematics

Light Source

The PicoQuant LED and driver that was used has shown good stability over several hours if it was switched on at least 30 minutes before use. In the first 30 minutes sometimes fluctuations were observed. In general, any fluctuations observed were much smaller than the other systematics and were thus neglected. For custom made LEDs driven with the pulse generator much larger fluctuations in the order of several percent were observed. Therefore these LEDs were not used. An analysis of their stability can be found in [114].

The Back End Absorber

The optical coupling to the black plate used at the back end of the tube showed similar problems as the optical coupling to the PMT. The same measures were performed to improve coupling and reduce light reflection. Since a large fraction of the light that is reflected would undergo strong propagation loses this effect can be neglected in most cases.

5.6 Summary

In this chapter, efficiency measurements, from a previous work [86], with photodiodes and small tubes (2 cm diameter) were introduced. They resulted in efficiencies (ϵ_{Wt}) of about 24 %. Furthermore, a limitation in the angular acceptance of photodiodes was shown that reduces these measurements to a lower limit, leaving the actual efficiency unclear. In response to that, a PMT measurement setup was designed and build. Several methods to evaluate these measurements were introduced and evaluated. Under ideal conditions, the model-independent method adapted from [109] has shown to be the most accurate evaluation method. Since ideal conditions in this context were often difficult to obtain, it was shown that no individual technique can always be applied, but it rather depends on the quality of the data as well as the information available about the equipment. The first efficiency measurements with small tubes and PMTs showed an efficiency of 51 ± 3 %. While this is a promising result many unresolved systematic uncertainties remain.

To verify the operational capability of the WLS-paint under cold condition, a comparison measurement was performed. The measurement in cold condition ($\epsilon_{\mathrm{Wt}} = 47.3 \pm 1.2$ %) showed slightly lower efficiencies than the comparison measurement ($\epsilon_{\mathrm{Wt}} = 51.0 \pm 0.1$ %) in warm conditions. However, due to the systematic uncertainties, they are considered consistent.

A coating setup was designed and built for large (9 cm diameter) tubes. The first comparison of cast and extruded tubes showed extruded tubes performed significantly worse than casted tubes. Casted tubes were therefore used to perform subsequent measurements. It was also shown that the particular cast tube showed differences in performance depending on which side was used for the measurement. At a maximum distance between photodiode and light source this systematic reached 25 %.

At this point, it was clear that many systematics were present when determining ϵ_{Wt}. Focussing on them as they arise might be time ineffective since evaluating one systematic might be influenced by other systematics. Also, larger systematics should be addressed first. Therefore the production of a minimum viable product in form of an optical prototype was given priority. The first prototype including adiabatic light guides was produced and its efficiency measured. The measured efficiency of the optical prototype was 13.0 ± 5.5 %. Such a low measurement was not expected. It was assumed that a large fraction of the losses were caused by the adiabatic light guide, the way it is glued to the WLS-tube or the holding structures that are also glued to the WLS-tube. Therefore, it was decided to exclude the adiabatic light guide for the time being and further evaluate the WLS-tube.[27]

With an ADQ14[28] becoming available, for measurements, it was possible to make more elaborate and accurate measurements. The measurement setup was modified to measure with three smaller PMTs at

[27] The evaluation of the adiabatic light guide was continued at the Mainz laboratory by local collaborators. Apparently, the losses are at least partially caused by the shape of the adiabatic light guide, reflecting light back into the tube. [116][117]
[28] 4 channel 14-bit digitizer, ADQ14 with 1 GSPS sampling rate and USB3.0 [110].

one large tube end simultaneously while recording all individual waveforms. The resulting efficiencies were between 21.5 ± 3.2 % and 28.6 ± 1.4 % depending on the evaluation technique used. The reason for the discrepancy to the measurements with smaller tubes remains unresolved. The most probable reasons are the large systematics, especially with the old setup as well as the different total thickness of the paint. However, an increase in coating velocity and thus paint thickness resulted in a slight increase in efficiency and is, therefore, recommended for the future. The timing distribution for different distances was also measured resulting in an approximate FWHM of 8 ns.

An improved version of the measurement with the ADQ14 introduced a fourth PMT to estimate the size of some systematics, used a higher coating velocity as well as measures to suppress stray light. An average efficiency of 28.1 ± 5.4 % was measured. While many systematics remain, this is the most reliable efficiency measured in this thesis. With the fourth PMT, two of the PMTs are in the same relative position to the light source and should measure the same result. Relative efficiency and timing behaviour matched within the given uncertainties. The absolute efficiency was lower for one of the PMTs. The reason for that is suspected to come from the optical coupling of the PMT to the tube.

Yet the central result of the measurements performed in this chapter is the identification of a large number of systematic uncertainties persistent in the measurements. Resolving these systematics is extremely difficult as many can not be clearly separated from one another and are likely of similar size. It was only possible to qualitatively describe them at this point. To quantify them additional equipment is necessary to take many more measurements in a shorter amount of time as well as to increase the precision of the measurements. A brief recommendation on measurements that should be performed in the future to gain a better understanding of the systematics can be found in chapter A.1.

In conclusion, many improvements in terms of measurement setups, evaluation techniques and general understanding have been made. Yet the complexity of the systematic uncertainties prohibited a reliable and conclusive result. The availability of a portal scanner and a subsequent increase in automation will be the next necessary step in investigating the systematics. First steps in quantitatively describing or eliminating systematics have been made in [114]. However, in [114] a WLS-paint with lower WLS concentration has been used and therefore the measurements shown there do not translate directly to the work done in this thesis.

CHAPTER 6

Model of Efficiency and Timing

This chapter focuses on the modelling of the physical processes involved in light capture and propagation within the WLS tube. In the first section, the model will be introduced. In the second and third section, a measurement for a model to data comparison is described and the model is adapted to the measurement. Subsequent sections describe the fitting procedure, the systematics and a conclusion.

6.1 Model

The model presented has the intention of describing the photon detection time and probability for a photon that was captured by a WLS molecule in the tube. Since the wall thickness of the tube is small in comparison to the tube radius, the tube can be approximated as flat, neglecting the curvature of the tube. This concept is illustrated in fig. 6.1, where light is emitted at a given distance to the light source

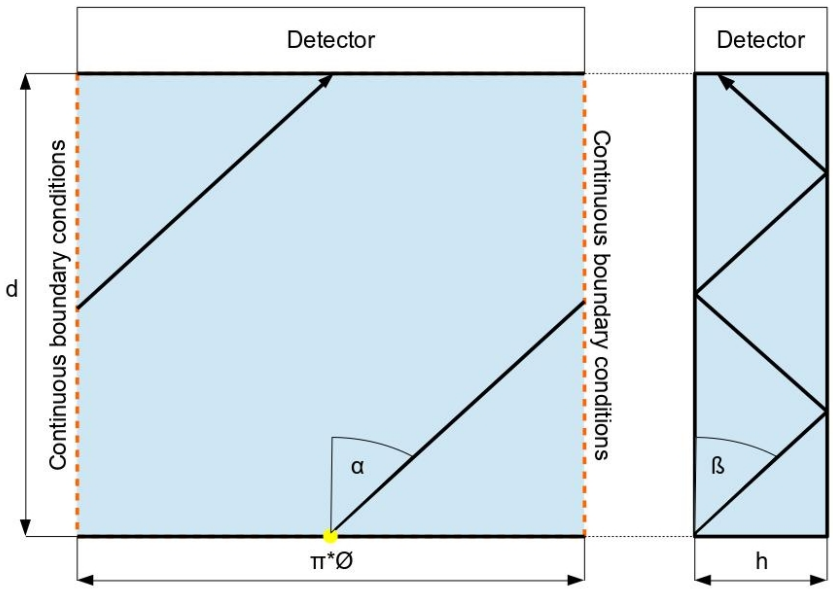

Figure 6.1: Unfolded tube with diameter ⌀ and light source to detector distance *d* on the left and side/cross-section view on the right with wall thickness *h*.

along the tube and its direction is described by two angles, one for the horizontal and vertical plane each. Light captured by the WLS has a probability of $\frac{\epsilon_c}{\gamma}$, that is theoretically 74.5 %,[1] to be emitted and captured in the tube by total internal reflection. With $\gamma \leq 1$ the emission probability of a photon by an excited WLS molecule. In turn, the probability for a photon to be emitted and not captured is $\frac{\epsilon_s}{\gamma}$ (theoretically 25.5 %). The correlation of these values is described by eq. 6.1.

$$\gamma = \epsilon_s + \epsilon_c \tag{6.1}$$

For each, the light captured and not captured, there is a probability that the light is afterwards measured by the light detector. This is described by $C(d)$ and $S(d)$, respectively, with d the distance of the WLS molecule to the light detector. Combining these, the probability that a photon from an excited WLS molecule can be observed in the light detector can be written as

$$P(d) = \frac{1}{2}(\epsilon_s \cdot S(d) + \epsilon_c \cdot C(d)) \tag{6.2}$$

with the factor $\frac{1}{2}$ accounting for the light detector only being on one side of the tube. $S(d)$ depends on the individual measurement setup and its surroundings. It can be approximated as $\frac{\Omega(d)}{4\pi} \approx \frac{\text{const.}}{d^2}$ with $\Omega(d)$ the solid angle under which the detector can be seen at distance d, when isotropic light is assumed.

$C(d)$ is at the core of the model and requires some additional explanation. For a full physics description of $C(d)$, that includes scattering and absorption, the propagation of many photons need to be individually simulated. This is because scattering changes the direction of the photon but it might still be detected or is detected even though it would not have been detected on its previous path. This can not be calculated analytically and requires extensive computing resources, which is not intended for this model. Instead, scattering and absorption is approximated by a common exponential decay constant (λ_{loss}). Then the probability to detect a photon[2] emitted at distance d under the angles α and β is described by eq. 6.3. $L(d, \alpha, \beta)$ is the path length to the detector as described by eq. 6.4. α describes the angle in the plane as illustrated in fig. 6.1. β describes the angle of up and down propagation within the wall of the tube and is limited by the total reflection angle Θ_{TOT} from eq. 6.5.

$$c(d, \alpha, \gamma) = \exp^{\frac{-L(d,\alpha,\beta)}{\lambda_{\text{loss}}}} \tag{6.3}$$

$$L(d, \alpha, \beta) = \frac{d}{\cos(\alpha) \cdot \cos(\beta)} \tag{6.4}$$

$$\Theta_{\text{tot}} = \arcsin\left(\frac{n_{\text{air}}}{n_{\text{PMMA}}}\right) \tag{6.5}$$

This assumes that scattering causes a photon not to be detected. Photons that are detected after scattering are assumed to behave similar to photons that were lost, virtually replacing them. For comparison to a measurement, this has no consequences in the efficiency domain but might cause changes in the time domain. To obtain $C(d)$, the average of $c(d, \alpha, \gamma)$ over all possible emission angles (that can lead to the detection) is calculated by integrating over these angles as described by eq. 6.6.

$$C(d) = \int_{\alpha=-\frac{\pi}{2}}^{\frac{\pi}{2}} d\alpha \int_{\beta=-(\frac{\pi}{2}-\Theta_{\text{tot}})}^{\frac{\pi}{2}-\Theta_{\text{tot}}} d\beta \frac{1}{2\pi} c(d, \alpha, \gamma) \cdot cos(\beta) \tag{6.6}$$

[1] As previously described in section 4.3.4

[2] Always assuming an ideal detector.

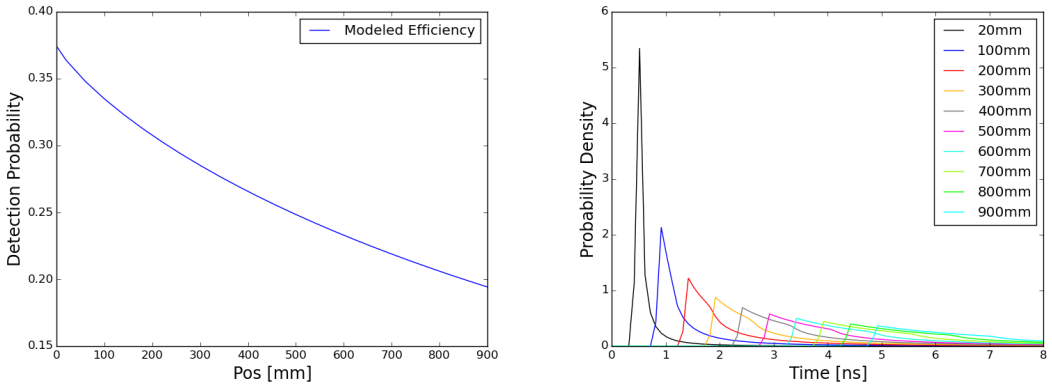

Figure 6.2: (left) Model based efficiency distribution. (right) Model based timing distribution. Parameters used: absorption length $\lambda_{\text{loss}} = 3$ m, WLS decay time $\tau = 0$, $\gamma = 1$, $S(d) = 0$ and $\epsilon_c = 0.75$

Exemplary efficiency and timing distribution are shown in fig. 6.2, with an absorption length of 3 m with no decay time, $\gamma = 1$, $S(d) = 0$ and $\epsilon_c = 0.75$. To obtain the timing distribution in fig. 6.2 (right), the propagation time was calculated according to eq. 6.7 for all possible propagation angles. These values were histogrammed, with each entry being weighted with their detection probability ($c(d, \alpha, \gamma)$. The bin size was set to 0.1 ns. 0.1 ns seemed the smallest time scale that could still be of value since the resolution in the measurement setup is restricted to 1 ns. The distributions are normalized to their integral.

$$t(d, \alpha, \beta) = \frac{L(d, \alpha, \beta) \cdot n_{\text{PMMA}}}{c} \tag{6.7}$$

To include the decay time τ, the timing distribution has to be convoluted with an exponential decay function (eq. 6.9). To also include instrumental timing resolution a Gauss-distribution (eq. 6.8) with width ω is convoluted into the distribution as well. The Gaussian has the additional advantage of, at least partially, compensating for the time smearing that is expected due to the incomplete modelling of photon scattering. Using a Gaussian here does theoretically violate causality since in the model small detection contributions of the photon would be possible before the photon is absorbed. These contributions are minor and are compatible with the desired accuracy of the model. The convolution is described in eq. 6.10, where $A(t)$ is an interpolated function resulting from the previous timing histogram. An example of a timing distribution, with some exemplary parameters for τ and ω, is shown in fig. 6.3.

$$G(t, \omega) = \frac{1}{\sqrt{2\pi}\omega} e^{-\frac{t^2}{2\omega^2}} \tag{6.8}$$

$$\mathrm{T}(t, \tau) = \begin{cases} \frac{1}{\tau} \exp^{-\frac{t}{\tau}}, & t > 0 \\ 0, & \text{otherwise.} \end{cases} \tag{6.9}$$

$$\widetilde{A}(t, \omega, \tau) = \int_{-\infty}^{\infty} \int_{-\infty}^{\infty} A(t - t' - t'') \cdot G(t', \omega) \cdot \mathrm{T}(t'', \tau)\, dt'\, dt'' \tag{6.10}$$

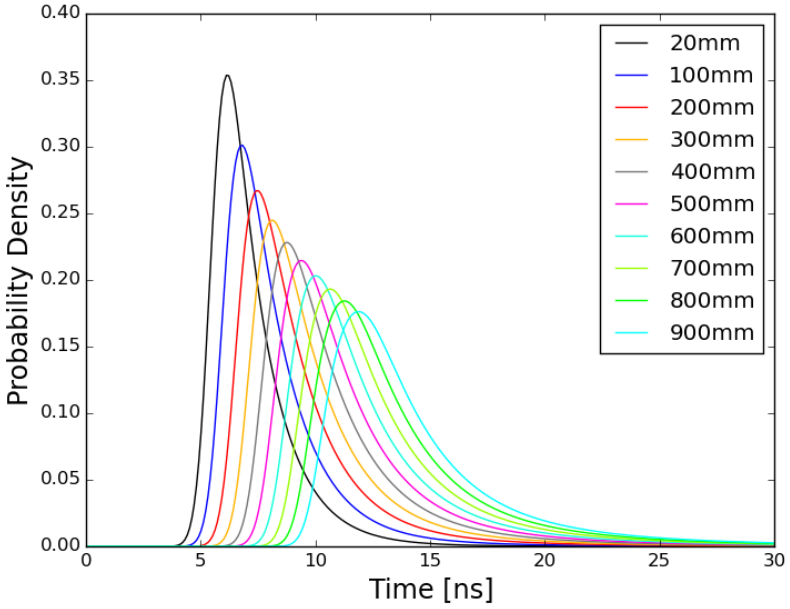

Figure 6.3: Timing histogram including decay time and Gauss broadening. Parameters used: loss length $\lambda_{\text{loss}} = 3\,\text{m}$, WLS decay time $\tau = 1.5\,\text{ns}$, Gauss-width $\omega = 0.2\,\text{ns}$, $S(d) = 0$ and $\epsilon_c = 0.75$

6.2 Measurement - Model Comparison

To determine the free parameters of the model and its description strength a real measurement is needed. For this the measurement described in section 5.4.5 was selected. It has the most comprehensive dataset, including efficiency and timing with light source position dependency. Furthermore, it has a superior resolution in comparison to older measurements. Due to stray light being blocked, $S(d)$ can be assumed to be 0. The use of four individual PMTs gives an additional opportunity to test the consistency of the model while requiring some modifications. In this section, the model is adapted to account for the four PMTs and thus allows a parameter fit of the data.

6.2.1 Adaption of the Model to the Measurement

To incorporate the 4 PMTs into the model, some parameters are adjusted individually for each PMT. The integration over α in eq. 6.6 is done numerically and only angles under which a specific PMT is hit are included. The values are stored individually for each PMT. This way 4 different efficiency and timing distributions are obtained. The fit parameters are used in the following way. The efficiency scaling in form of ϵ_c and an additional time offset Δt, that is introduced to correct for cable length variations in the measurement, is determined for each individual PMT. The loss length λ_{loss} from eq. 6.6 and additionally for the timing histograms the Gauss width ω and the decay time τ from eq. 6.10 are used globally for all PMTs.

6.2.2 Fitting the Model to the Data

To fit the model to the measurement a minimizer on χ^2 as given in eq. 6.11 is used.

$$\chi^2 = \sum_{i=1}^{k} \frac{(x_i - m_i)^2}{\Delta x_i^2} \tag{6.11}$$

Here m_i is the model value at a certain position, x_i and Δx_i are the measured value and it's statistic error respectively. i runs over all available measurements and thus the fit includes timing and efficiency data. The timing has a larger weight due to the higher number of values and smaller errors. The best fit values for these parameters are:

$$\begin{aligned} \lambda_{\text{loss}} &= 3060.99\,\text{mm} \\ \omega &= 0.6023\,\text{ns} \\ \tau &= 1.3701\,\text{ns} \end{aligned}$$

$$\begin{aligned} \epsilon_c(\text{PMT1}) &= 0.6949 & \qquad \Delta t(\text{PMT1}) &= 323.68\,\text{ns} \\ \epsilon_c(\text{PMT2}) &= 0.6937 & \qquad \Delta t(\text{PMT2}) &= 313.15\,\text{ns} \\ \epsilon_c(\text{PMT3}) &= 0.7698 & \qquad \Delta t(\text{PMT3}) &= 313.08\,\text{ns} \\ \epsilon_c(\text{PMT4}) &= 0.7703 & \qquad \Delta t(\text{PMT4}) &= 315.60\,\text{ns} \end{aligned}$$

The resulting statistical errors determined from the Hessian matrix are in the order of the least significant digit or smaller. Considering that the systematics are not taken into account, the errors from the Hessian matrix are unrealistic and thus not shown. An alternative approximation of the errors will follow in section 6.2.3. To obtain the fit values a combined number of 5112 data points have been used. 72 of those were efficiency values and the remainder timing values. The fitting range encompasses fiber positions from 8 to 83 cm in 5 cm steps and a 70 ns window for each timing histogram. With 11 fit parameters the d.o.f. are 5101. Looking at the exemplary timing distributions corresponding to this fit for PMT 3 in fig. 6.4, it can be seen that the normalized measured timings fit visually well to the modelled distributions. However the combined χ^2/d.o.f. is 6.4, showing a bad match. This is either because the models descriptive properties are insufficient or because the systematic errors are not taken into account yet.

For the efficiency values, the visual match as shown in fig. 6.5 appears reasonable considering the errors. For PMT two and three the measured values at close distances are much larger than anticipated by the model. This might be a $\frac{1}{d^2}$ contribution due to imperfect blockage of the stray light. The combined χ^2 /d.o.f. for all efficiencies is 3.9. The reason for the rather high value here is also that systematics has not been taken into account yet. Also, the number of values included in the fit is lower than the ones from the timing, while the relative error is larger. This causes these values to not contribute as much to the fit result as the timing does.

To estimate the errors, obtain a better understanding of the systematics and the match of model to data, further studies and comparison to literature values are performed in the next section.

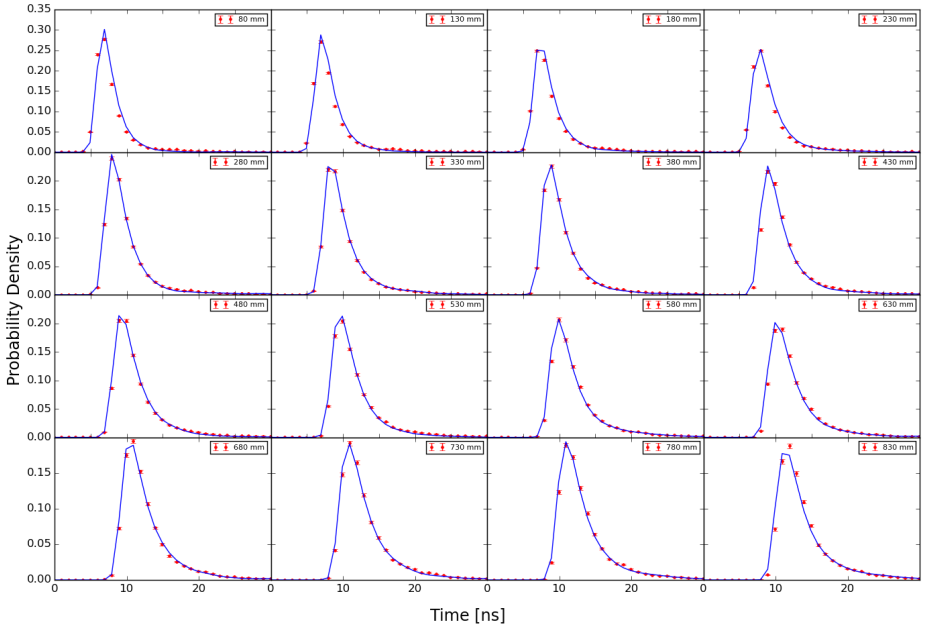

Figure 6.4: Normalized timing distributions for PMT 3. Error bars indicate data, lines indicate the model fit.

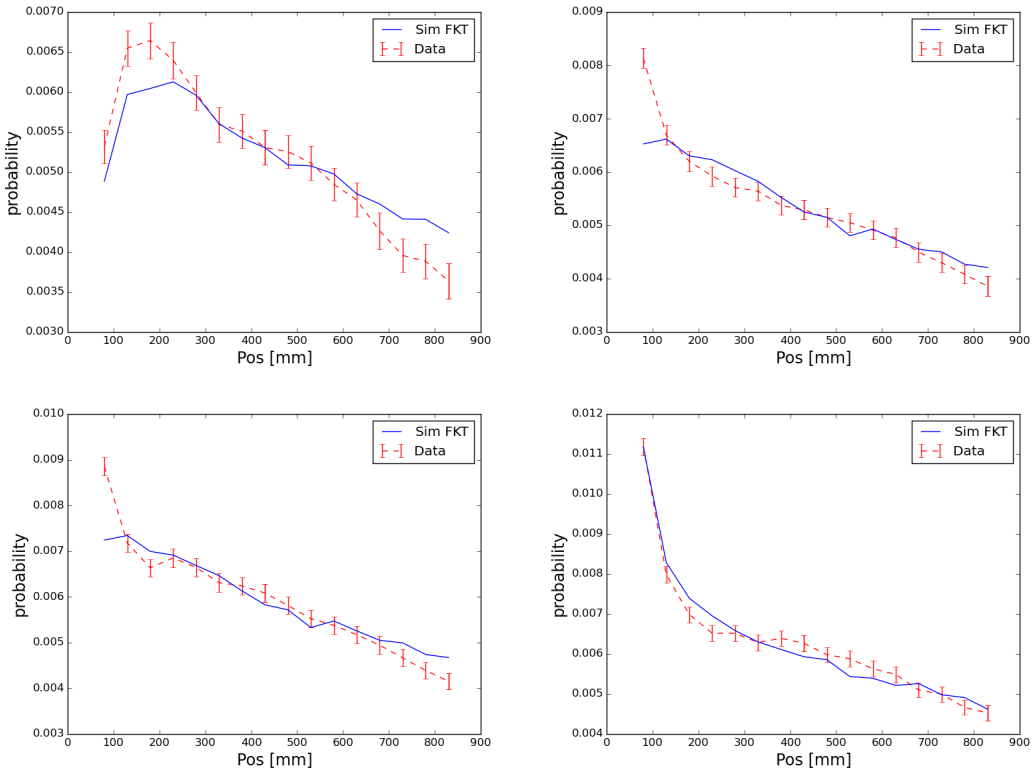

Figure 6.5: Efficiency as function of the light source position along the tube for all four PMTs. PMT 1 (upper left), PMT 2 (upper right), PMT 3 (lower left) and PMT 4 (lower right).

6.2.3 Further Studies and Evaluation of the Fit Results

In order to understand the accuracy of this method better, the fit has been performed on individual parts of the measurement. For this purpose, all timing measurements have been fitted while ignoring the efficiency and vice versa. Furthermore, the measurements including timing and efficiency for individual PMTs have been fitted. This also includes a combined fit of PMT 2 + 3 since they are symmetrically positioned towards the light source and thus should produce the same results.

The first set of results is shown in tab. 6.1. Here one can see that the loss length λ_{loss} fluctuates most while the Gauss width ω and the decay time τ are more stable. The loss length λ_{loss} with 3060.99 mm and a standard deviation between the subset fits of 430.53 mm is compatible with the rather broad literature values for absorption. Several of those literature values are given in [118], at 440 nm wavelength, which is closest to the WLS emission spectrum, they range from 1530 ± 40 mm to 7300 ± 930 mm for different PMMA samples and manufacturers. It is not surprising that the value for λ_{loss} agrees with the rather broad literature values, yet it should be considered that λ_{loss} also partially accounts for scattering. Therefore, a dedicated absorption measurement, from a sample that was used for the measurement, would be better comparison and even allow for a separation of absorption and scattering properties. A comparable model also based on λ_{loss} [116], that uses a different calculation method on a different tube, obtains a value of 2955.2 ± 153.4 mm, which agrees well with the value measured here. The Gauss width ω of 0.6023 ns with a standard deviation between the subsets of 0.0078 ns is small in comparison to the ADQ resolution of 1 ns but with a large number of statistics, a resolution of 0.6 ns is realistic. A contribution in time smearing from the scattering of photons can not be observed. Considering the small size of the PMTs the transit time spread should be comparatively low too. The decay time τ of 1.3701 ns and a standard deviation between the subsets of 0.0608 ns matches within 2σ with the 1.2 ns given in [119] for Bis-MSB without a specific substrate material. 1.5 to 1.7 ns were measured in [120] dissolved in various solvents. Given that the decay time varies depending on substrate material the value measured appears reasonable. PT is not taken into account here since the excitation wavelength in this measurement is above the absorption wavelength of PT.

	loss length λ_{loss} [mm]	Gauss width ω [ns]	decay time τ [ns]
Normal	3060.99	0.6023	1.3701
Timing only	3073.99	0.6025	1.3687
Efficiency only	2483.78	-	-
PMT 1 only	2597.24	0.6125	1.3079
PMT 2 only	3496.73	0.5896	1.4049
PMT 3 only	3520.56	0.6092	1.3877
PMT 4 only	2478.12	0.6144	1.2202
PMT 2 and 3 only	3510.95	0.6010	1.3951
Standard deviation	430.53	0.0078	0.0608

Table 6.1: Fit results for absorption length, Gauss width and decay time of a selected set of the measurement results.

In tab. 6.2 the efficiency scaling factors are shown. They are consistent with one another if a small fluctuation for the goodness of the optical coupling for each PMT is assumed. Averaging all four values and the standard deviations of their subsets we obtain a light absorption and capture efficiency of 73 ± 3 %. This is well compatible with the theoretical maximum of 75 %. It should be pointed out though that the systematic errors might well be larger than 3 % since values as much as 6 % higher

than the theoretical maximum have been determined in some subsets. Non suppressed stray light from equipment in the black-box or photons that back-scatter within the tube, might be a reason for this. A value as high as 73 % also indicates about 98 % QE of the paint. Literature values for the QY vary but are generally larger than 90 %[88][89][90]. For the paint used here, a rudimentary measurement in [86] showed values close to a 100 % which would be consistent with the results here.

Efficiency scaling factor ϵ_c	PMT 1	PMT 2	PMT 3	PMT 4
Normal	0.6949	0.6937	0.7698	0.7703
Timing only	-	-	-	-
Efficiency only	0.7412	0.7373	0.8187	0.8132
PMT 1 only	0.7305	-	-	-
PMT 2 only	-	0.6699	-	-
PMT 3 only	-	-	0.7417	-
PMT 4 only	-	-	-	0.8137
PMT 2 and 3 only	-	0.6693	0.7422	-
Standard deviation	0.0198	0.0277	0.0313	0.0203

Table 6.2: Fit results for the efficiency scaling factor ϵ_c of all four PMTs

In tab. 6.3 the timing offset values for all four PMTs are shown. They are consistent with each other and their standard variation is only about 0.02 ns which is much smaller than the 1 ns hardware resolution and the 0.6 ns Gaussian spread. For this reason, those values are considered measurement dependent constants from this point on but have no further relevance for the underlying physics.

Time offset [ns]	PMT 1	PMT 2	PMT 3	PMT 4
Normal	323.68	313.15	313.08	315.60
Timing only	323.68	313.15	313.08	315.60
Efficiency only	-	-	-	-
PMT 1 only	323.73	-	-	-
PMT 2 only	-	313.12	-	-
PMT 3 only	-	-	313.06	-
PMT 4 only	-	-	-	315.69
PMT 2 and 3 only	-	313.13	313.05	-
Standard deviation	0.02	0.01	0.01	0.04

Table 6.3: Fit results for the time offset of all four PMTs

All the off-diagonal parameters of the Hessian matrix or covariance values are smaller than the corresponding diagonal parameters, which indicates uncorrelated fitting parameters. Since the χ^2/d.o.f. is rather high these parameters are not necessarily reliable and phase space plots showing the χ^2/d.o.f. value for two fit parameters around the best fit have been created. In all 50 resulting plots, no significant interdependence between two fit parameters could be found. A representative example of those plots can be seen in fig. 6.6.[3]

[3] There is no change in fit-quality for the efficiency scaling factor in the top-left plot visible. This is due to the strong change for the time offset. For reference, the same efficiency scaling factor is used in the top-left plot.

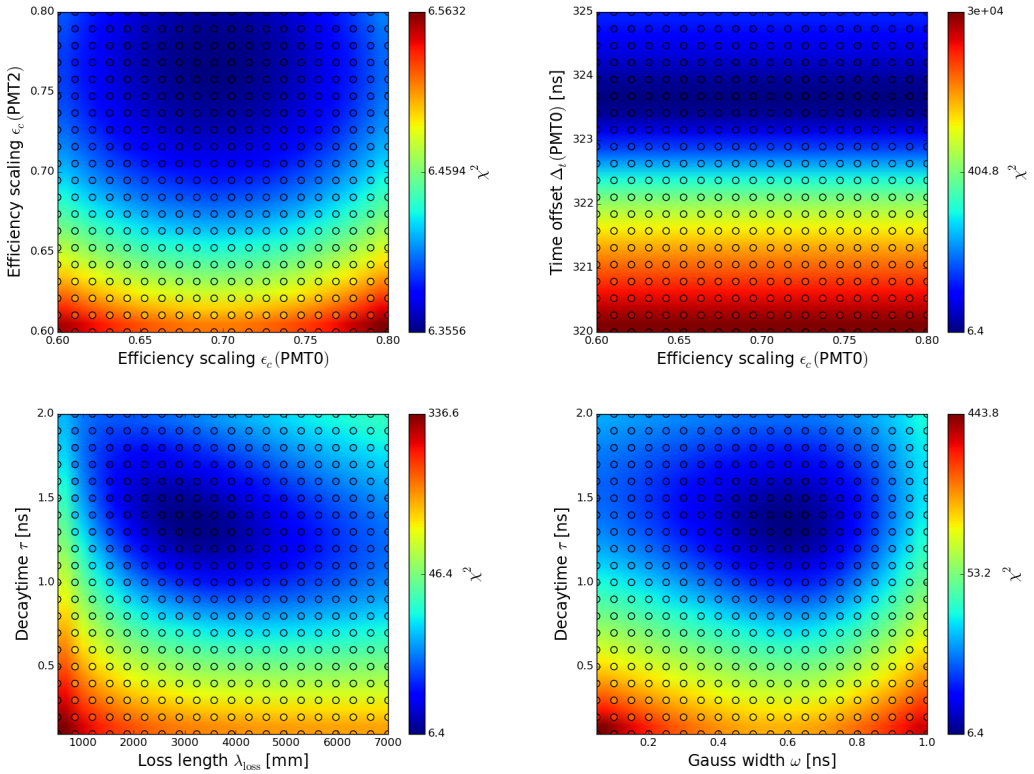

Figure 6.6: Plots showing χ^2/d.o.f behaviour as a dependence of two of the used fit parameters. Circles are points where the χ^2/d.o.f was evaluated. The colours are interpolations based on these values.

6.2.4 Systematic Uncertainties

All fit parameters with the standard deviation taken from the subsets have a reasonable agreement with literature values. To put their reliability in the context of the measurement, the most important systematic uncertainties are discussed in the following.

Acceptance Angle of PMTs

As previously discussed ins section 5.5.1, the optical coupling allows light from odd angles to reach the PMT. The light gained by optical coupling hits the cathode under very steep angles where the acceptance is not well known. Since steep angles also have long photon paths, the model is not very sensitive to losses at these angles. Therefore no conclusion on the angular acceptance of the PMTs can be drawn.

Optical Coupling of the PMTs

As previously described, perfect optical coupling with the optical gel used in this experiment is difficult to achieve. The effect to the model results should be small since again only steep angles are effected. Those angles represent a longer photon path and thus a larger probability of absorption or scattering.

Optical Coupling of the Light-Absorbing Backplate

Here the same problem as with the optical coupling of the PMTs arises, however, the effect is significantly smaller. Light at the surface of imperfect coupling might just be reflected and thus has the possibility of being absorbed while propagating to the PMTs. This effect might increase the efficiency slightly but should at least be cancelled out by the previous systematic if the quality of the optical coupling is comparable.

Positioning of the PMTs

The PMTs are positioned 90° from each other as shown in fig. 5.32. This positioning is done by hand and might have a few degrees of error thus influencing the quality of the fits. This effect can be seen best in the variations in efficiency due to the PMT positions as shown in fig. 6.5. This systematic might be partially responsible for capture efficiencies higher than the theoretical maximum of 75 %.

Paint Quality

As previously discussed, the surface quality has been shown to fluctuate for various reasons. A few percent error should be kept in mind for that. However, as long as these losses are rather uniformly distributed they are at least partially included in the fit of λ_{loss}.

Negligence of Light Scattering in the Model

Since the model does not directly include scattering, which is an effect that certainly takes place, a deviation from the measured results is expected. No deviation in the efficiency could be observed that can be attributed to light scattering. Therefore it can be assumed, that the scattering that does take place is well described by a simple exponential loss function and has otherwise no detectable contribution. In the timing distribution, a correction for the limited timing resolution was supposed to also account for additional smearing in timing, yet a χ^2/d.o.f. of 6.4 is observed. It is unclear if scattering or other underlying systematics are the cause of this.

Stray Light

Stray light in the measurement chamber is strongly suppressed by the black walls and their distance to the setup. Stray light as described by $S(d)$ is supposed to be eliminated by a cloth around the tube and an absorber in its center. As it can be seen in fig. 5.31 the absorber in the center does not cover 100 % of the center of the tube, since a perfect match would mean to much optical contact to the tube. This way a non zero suppressed $S(d) \propto \frac{1}{d^2}$ component might contribute to the measurement. This can explain the excess in the efficiency for PMT 2 and 3 at close distances, as it can be seen in fig. 6.5.

6.2.5 Results

In this chapter, a model for the light capture and propagation in the WOMs PMMA tube was suggested and fitted to measured data. It was possible to show, that the model can describe the data qualitatively well. The timing distributions have a high χ^2/d.o.f. of 6.4. The reason for this cannot be clearly determined. Considering the in comparison to the absolute value relatively small systematic errors of the timing histograms, the agreement with the model is good for the intended purposes of the model. Relative deviations are larger for the efficiencies but only have a χ^2/d.o.f. of 3.9. The still large deviation

is assumed to come from systematic uncertainties that could not be quantitatively described. The current best fit results for the main parameters (and the range of corresponding literature values) are as follows:

$\lambda_{\text{loss}} =$	$3.1 \pm 0.4\,\text{m}$	(Absorption:1.5 *to* 7.3 m / λ_{loss}:3.0 ± 0.2 m)
$\omega =$	$0.602 \pm 0.008\,\text{ns}$	
$\tau =$	$1.37 \pm 0.06\,\text{ns}$	(1.2 *to* 1.7 ns)
ϵ_c(Mean over all PMTs) =	0.73 ± 0.03	$(0.75 \cdot (0.9$ *to* $1.0))$

The standard deviation was determined from the variance of fits done on subsets of the available data and thus contain part of the systematic error. These values compare well to literature values where they are available. A further improvement could be achieved by including scattering during the light propagation. However, this would increase the necessary computation time drastically. For the same reason, the much more accurate method of likelihood profiling to determine the error was not feasible. Currently, a model fit takes, depending on the desired accuracy, between a few hours to several days.

Based on these results most of the photon losses occur during light propagation. To increase the overall efficiency material and surface quality should be further investigated and improved.

CHAPTER 7

Simulation Studies

This chapter describes how a simplified model of the WOM was built into the IceCube simulation framework. Furthermore, basic tests are conducted with those modifications in place to evaluate the performance of the WOM in different IceCube-Gen2 configurations. The results are compared to the pDOM (introduced in section 3.2.3). The pDOM is the upgraded version of the IceCube DOM and is used as a baseline comparison with identical datasets.

7.1 The IceCube Simulation Framework

The IceCube collaboration has developed a complex simulation framework, to test and train analyses as well as to improve the understanding of the processes in the ice. The framework is highly modular to make all the different kinds of applications possible. Every step from primary particle simulation, over the type or model of the ice to the OM readout is designed as an individual module. For many of these modules, alternatives exist with slightly different abilities. Overall the complete process from a particle entering the detector to the readout and analysis of events can be reproduced in a way that closely resembles the real detector. It becomes clear there are many possibilities to assemble a simulation chain. The simulation chain used for the WOM simulation will be outlined in the following four steps in this section.

- **Step 1** As illustrated in fig. 7.1 (left) an empty event file in a custom format is created. To specify the space in which the simulation can be performed, the detector geometry is attached to the file. After that, the empty event is filled with a muon event. This is done with a module called "muongun". It can create muon events with specifications as direction and energy. In this case, the direction is random to create an isotropic distribution in a specified energy range and energy distribution. The next module called "proposal" [121], propagates charged leptons and calculates how many photons are produced along the track, by the use of light distribution templates. To reduce the computation time, the simulation volume is limited to a cylinder that is sized to contain all relevant interactions. The resulting event is then stored in an event file along with many other events. This is done because this part of the simulation is identical independent of the OMs used, while the following steps differ. Which makes it possible to simulate the same events in the same geometry for different OMs. To generate in the order of a thousand events usually takes a few minutes.

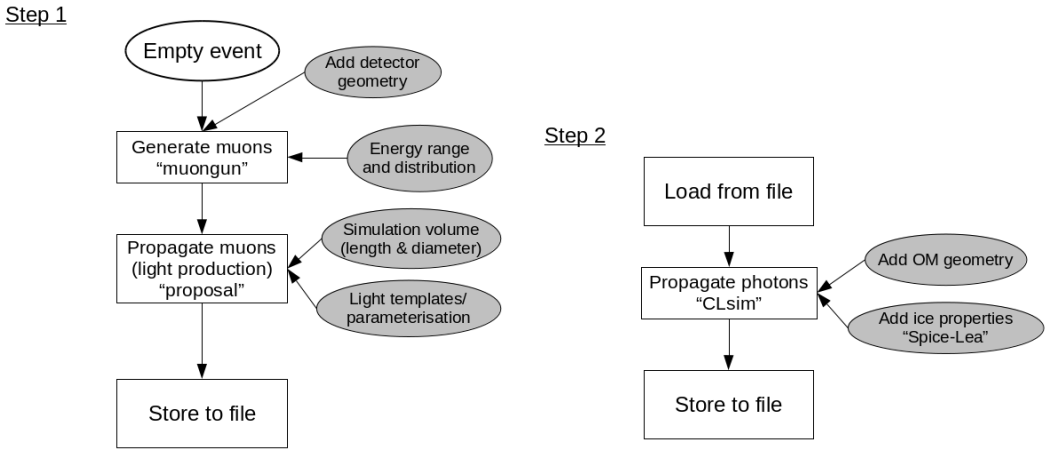

Figure 7.1: Illustration of Step 1 (left) and 2 (right) of the simulation chain used in this thesis.

- **Step 2** As illustrated in fig. 7.1 (right) the previously created file is loaded again. The individual OM geometries and the ice model "SPICE-Lea" [122] are added to simulate the photon propagation from the muon track to the surface of the OMs. This is the most computationally expensive task and takes several days to weeks on a medium-sized computing cluster, for a few thousand events, depending on their energy range. This includes already performance improvements such as layering of the ice or checking for photon interactions with OMs only when they are in reasonable proximity. The module performing these calculations is called "clsim", runs on GPUs and is written in C++ as well as OpenCL. It is one of two modules in the IceCube simulation framework to do this, the other one is "PPC". It has been chosen since it is the newest and most modular one of the two modules. The simulated photons that are propagated to the surface of the OMs are stored again in an event file for further processing.

- **Step 3** As illustrated in fig. 7.2 (left) the file with the individual photons propagated to the OM surfaces is loaded again. The detection of the photons by the modules is then simulated. The information used for that depends very much on the individual OM type, how well the module is understood and how much detail is desired. All modules have in common a wavelength-dependent acceptance function[1], a photon direction-dependent acceptance function and some kind of time modelling. To more accurately describe the behaviour of the WOM, it additionally features a position-dependent component that varies time and acceptance parameters. The details on that will be described in this chapter. The results of the simulated and detected photoelectrons are then stored in an event file for further analysis.

- **Step 4** As illustrated in fig. 7.2 (right) there are two options to proceed after loading the file produced in step 3. In a full simulation, at this point, it would be simulated if the virtual IceCube trigger would detect the event as such. A reconstruction would follow a positive trigger. However, for a realistic reconstruction, a large set of simulations is needed as a reference for the

[1] This function is also used previously in the photon generation from the muon track to optimize performance. This feature is optional but decreases the time needed for step 2 significantly. Yet it requires re-simulation of step 2 when a change to the OM acceptance are applied.

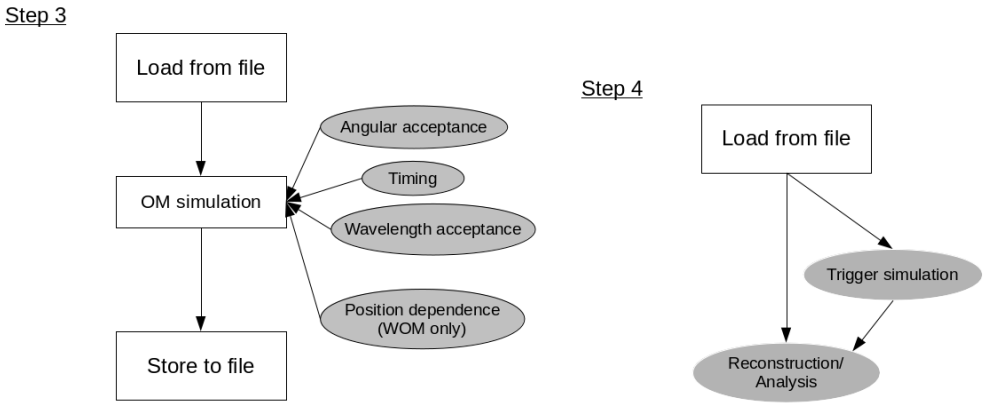

Figure 7.2: Illustration of Step 3 (left) and 4 (right) of the simulation chain used in this thesis.

reconstruction algorithm[2]. To produce those an extensive amount of computation time and effort is needed. Especially for new OMs where the necessary modification in the production algorithm need individual tweaking. For this reason, it was decided to only analyze the detected photons, which can be found in this chapter.

7.2 Photon Propagation

The photon propagation in ice, as described in step 2, is an integral part of the IceCube simulation framework. To incorporate non-spherical OMs, like the WOM, into the software, the algorithm detecting collisions between photons and OMs, in clsim, had to be changed. To save computation time the WOM is split into three independent geometric bodies. For the upper and lower end a sphere is used and a cylinder in between. For a full description of this shape, only the radius and the height of the cylinder are required. A schematic view of this separation can be seen in fig. 7.3. Interaction points are calculated for all three bodies. If more than one body is hit by a photon, the earliest interaction point in the photon path is taken as the final interaction point. Final interaction points are written into data files and are processed further later. To ensure the functioning of this detection algorithm, the distance of the photons to the OM is later recalculated with an independent program using double precision. The resulting maximum discrepancy between photon position and OM surface is 3 cm. This seems a rather large number, however discrepancies larger than 0.5 cm occur only about once in 100, 000 events. The discrepancy comes from an accumulation of rounding errors of 16 bit floating-point numbers and is the same for all other modules simulated in IceCube. The 16 bit limit is used for performance and compatibility reasons with some GPUs. A histogram of absolute photon distances is shown in fig. 7.4.

7.3 OM Modeling

To convert the incident photons into a signal comparable to the real experiment, as described in step 3, the detection of photons by the OM needs to be replicated. To do this, a combination of established theoretical knowledge and modelling of the measured data were used to simulate the photon-detection. The properties that need to be modelled are the angular acceptance, the wavelength acceptance, the

[2] To be specific for the generation of spline tables.

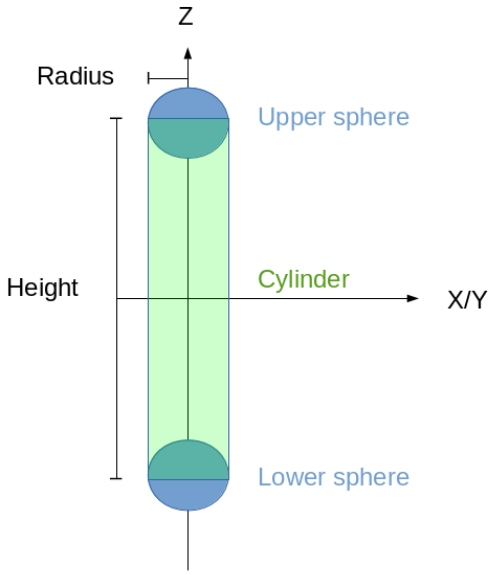

Figure 7.3: Sketch of the geometrical separation of the WOM for photon collision detection.

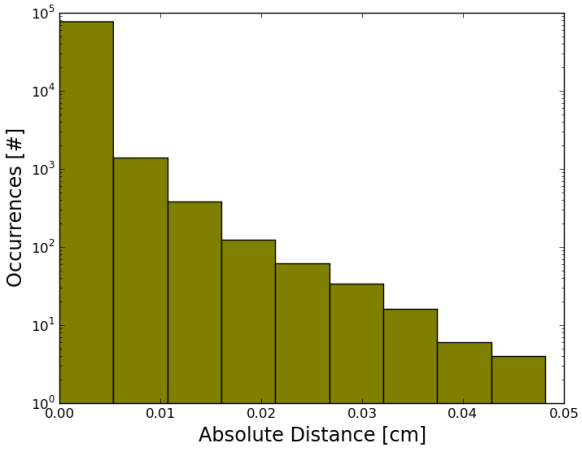

Figure 7.4: Histogram of the absolute photon distance[3] to the WOM surface.

position-dependent acceptance and the timing behaviour. To determine whether a photon is detected or not, the different acceptances are calculated on an individual photon basis and thereafter combined to a single detection probability. A pseudo-random number generator is then used to determine if the photon is detected or not. Afterwards, a detection time is determined from a probability density function (PDF) by the use of a second random number. In the following, the details on obtaining these values are described.

7.3.1 Angular Acceptance

Since the actual refraction **ice → quartz glass → air** as shown in fig. 7.5 (left) is difficult to accurately measure in our laboratory, Snell's law and the Fresnel equations [123] are used to model the angular

acceptance. The result of these calculations is the transmission coefficient as shown in fig. 7.5. The critical angle between ice and air of ≈ 0.825 rad is well pronounced. In reality, small additional smearing will likely occur due to scattering on impurities such as air bubbles in the pressure vessel glass. For better comparison to the pDOM, the angular acceptance normalized to the maximum angular acceptance is calculated and shown in fig. 7.6 (right). A homogeneous parallel light beam incident to the WOM at angle β is assumed as described by fig. 7.6 (left). Thus including the geometric aspects such as the projected area of the WOM that is reduced by $\cos(\beta)$ and the reduced acceptance due to the curvature of the WOM. For simplification, it is assumed that the end caps do not contribute to the photon detection. Alternative fillings for n_{air} are not considered.

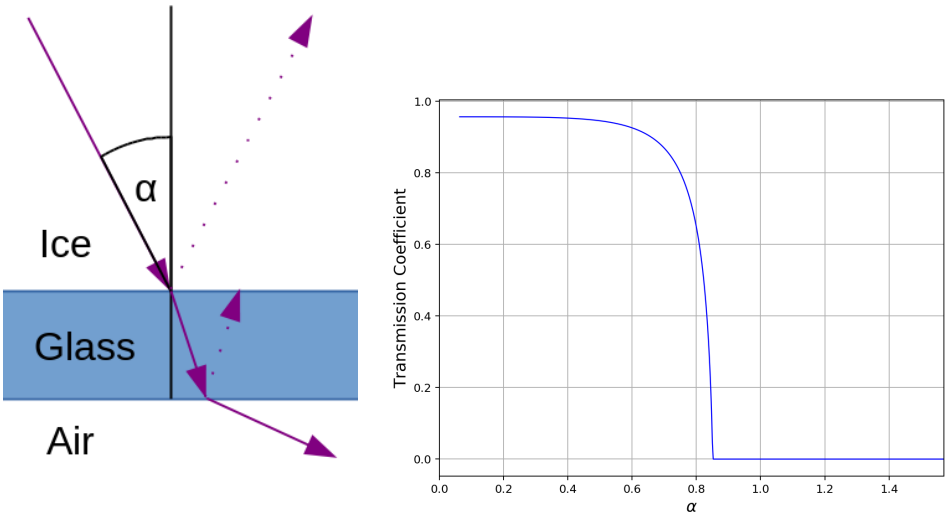

Figure 7.5: (left) Sketch of the light paths through the different materials. (right) Calculated angular transmission coefficient for $n_{\text{ice}} = 1.33$, $n_{\text{glass}} = 1.5$ and $n_{\text{air}} = 1$.

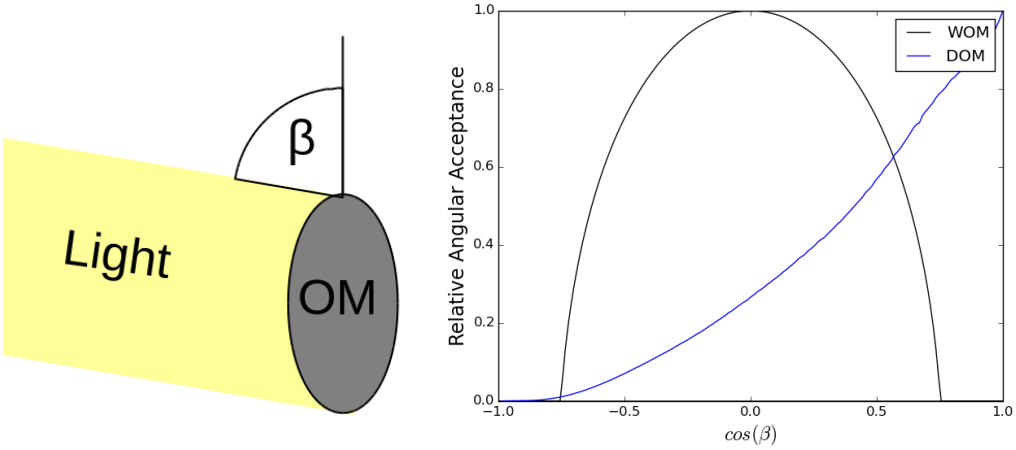

Figure 7.6: (left) Illustration of the projected angular acceptance (right) Projected angular acceptances for the WOM and the DOM for comparison. For both functions the maximum is set to 1.

7.3.2 Measurement-Based Modelling

To model the data, we have to start with a set of WOM parameters that are based on measurements. The measurement is taken with the improved measurement setup in section 5.4.4 and the evaluation with the partial fitting method (2Gauss+Exp) has been selected for this.[4] To emulate the results for a single PMT the weighted average of the three PMT, according to eq. 5.28, has been used.

Position Dependent Acceptance

For the position-dependent acceptance, the efficiency measurements at 370 nm wavelength for different positions along the tube are used. To cover the full range between 0 and 90 cm the values between measurements were interpolated linearly and for the edges, a constant extrapolation was used. A visualisation can be seen by the black line in fig. 7.7. To get an acceptance for the whole module the resulting function was first mirrored according to eq. 7.1 (fig. 7.7 red line), with $P_{\mathrm{L}}(x)$ being the detection probability for the left PMT at position $x = 0$, as a function of position x along the module. This is followed by stacking both equations according to eq. 7.2 (fig. 7.7 yellow line), thus accounting for upper and lower PMT of the WOM.

$$P_{\mathrm{R}}(x) = P_{\mathrm{L}}(90\,\mathrm{cm} - x) \tag{7.1}$$

$$P_{\mathrm{hit}}(x) = P_{\mathrm{L}}(x) + P_{\mathrm{R}}(x) \tag{7.2}$$

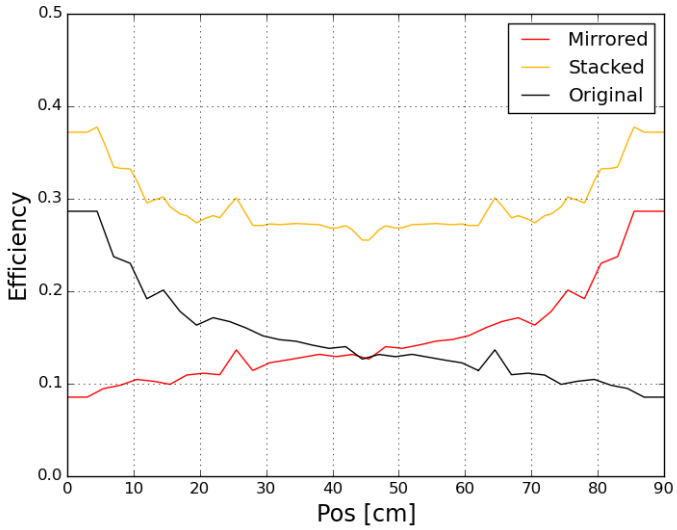

Figure 7.7: Position dependent efficiency scaled with the ratio of PMT area covering the tube to the area of the tube end. The same function mirrored and stacked according to eq. 7.2.

If it is determined by the method above that the module did detect a photon, an independent calculation determines which PMT detected the photon. For that eq. 7.3 determines the likelihood for each PMT to be hit depending on the position x of the photon. Here $P_{\mathrm{L}}(x)$ is normalized by itself plus the mirrored

[4] This was the best measurement and evaluation at the time this simulation was designed. From today's view, this is not the case any more. Appropriate corrections will be discussed at the end of this chapter.

function $P_{\mathrm{R}}(x)$, which gives the likelihood for one PMT to detect the photon opposed to the other. For the actual calculation, a random number [0, 1] is created. If this number is larger than $\mathrm{PDF}_{\mathrm{PMT}}(x)$ the right PMT at $x = 90\,\mathrm{cm}$ detects the photon and otherwise, the left PMT at $x = 0$ detects the photon. The resulting function in comparison to $P_{\mathrm{L}}(x)$ is shown in fig. 7.8.

$$\mathrm{PDF}_{\mathrm{PMT}}(x) = \frac{P_{\mathrm{L}}(x)}{P_{\mathrm{L}}(x) + P_{\mathrm{R}}(x)} \tag{7.3}$$

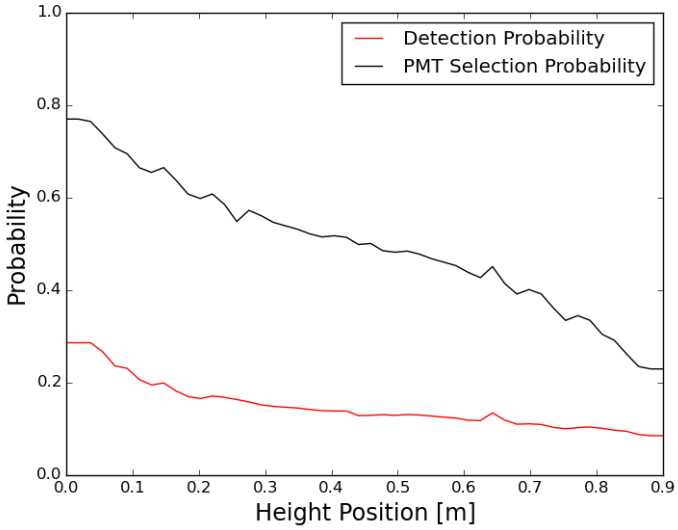

Figure 7.8: One-sided position-dependent efficiency and the resulting probability for a left sided PMT detection if a photon is sure to be detected.

Modelling of the Photon-Detection Time

For the time modelling a simple approximation of the photon propagation time within the WOM is sufficient since no reconstruction is performed based on this data. For this, log-normal distributions are fitted to the timing histograms from the measurement. For each of the resulting fit parameters, a parametrisation is found. The parametrisation allows a description of the timing distributions at any position along the tube with eight parameters. The corresponding procedure and the intermediate results are detailed in section A.3. The result can be seen in fig. 7.9. Position and width are sufficiently well described for a first performance estimate. The tail of the distribution is mostly ignored, this can be significantly improved when 2D spline interpolations based on the model in chapter 6 are used in the future.

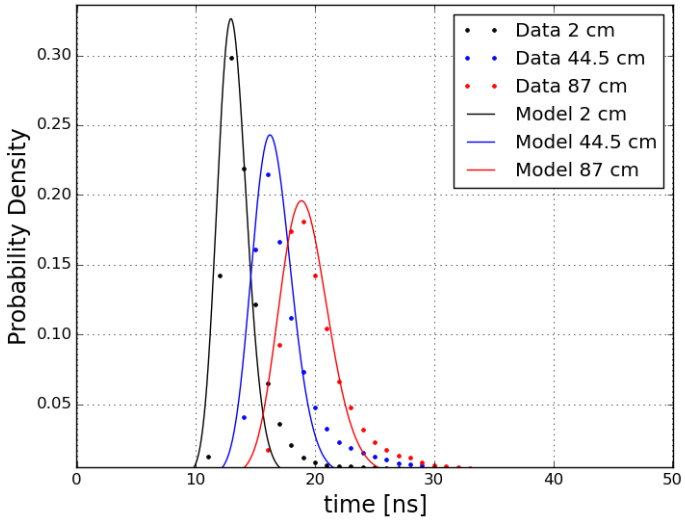

Figure 7.9: Comparison between real timing data and model.

7.3.3 Wavelength Acceptance

To account for the wavelength-dependent sensitivity a wavelength-dependent efficiency measurement as described in [86] is used as a template. Since the actual efficiency at 370 nm is already contained in the position-dependent acceptance from section 7.3.2 the relative wavelength acceptance is scaled to 1 at 370 nm. The resulting acceptance is shown in fig. 7.10.

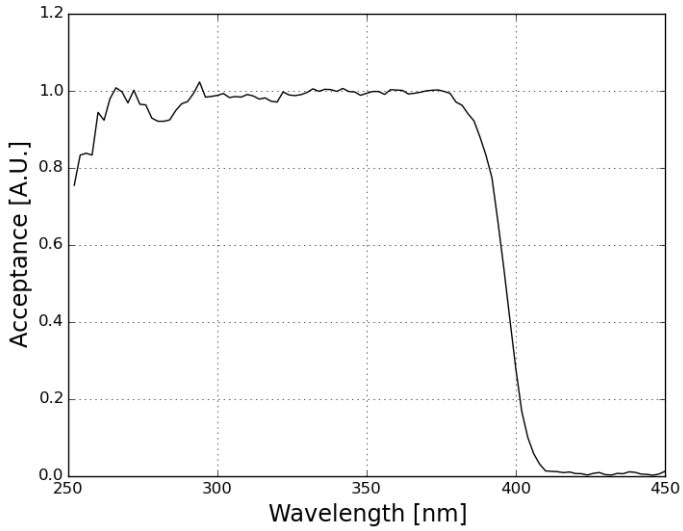

Figure 7.10: Wavelength acceptance with $f(\lambda = 370\,\text{nm}) = 1$

7.4 Gen2 performance comparison for WOM and pDOM

To estimate the performance of the WOM in an IceCube-Gen2 detector, different simulations are performed and some basic quality parameters are determined and checked. For that five different IceCube-Gen2 geometries with 80 OMs/string have been chosen to compare the WOM to the pDOM. The geometries can be seen in fig. 7.11. The banana geometry represents an asymmetric detector for a direction and time-dependent increase in muon track resolution, due to the earth's rotation. The edge-weighted geometry tries to veto events better that start outside the detector. The sunflower geometries reduce the chance of a muon passing through the center of a row of strings without being detected. There are three different sunflower geometries which only differ in their inter string space from 200, 240 and 300 m. The spacing increases the detection volume but also the energy threshold. If the geometry does not affect the parameters displayed the values for the sunflower geometry with 240 m string spacing is used. The sunflower 240 geometry is currently the preferred one since simulations based on the pDOM showed it to have a good combination of performance parameters. The WOM simulated has a height of 1.014 m. This includes a cylindrical midsection with a length of 0.9 m and 11.4 cm diameter plus a half-sphere, with the same diameter, at each end. Readout electronics are not physically modelled. The WLS tube in the WOM also has a length of 90 cm, with a diameter of 9 cm. The data used, to model the WLS tube, has a mean efficiency, over the length of the tube, of 28.6 %.

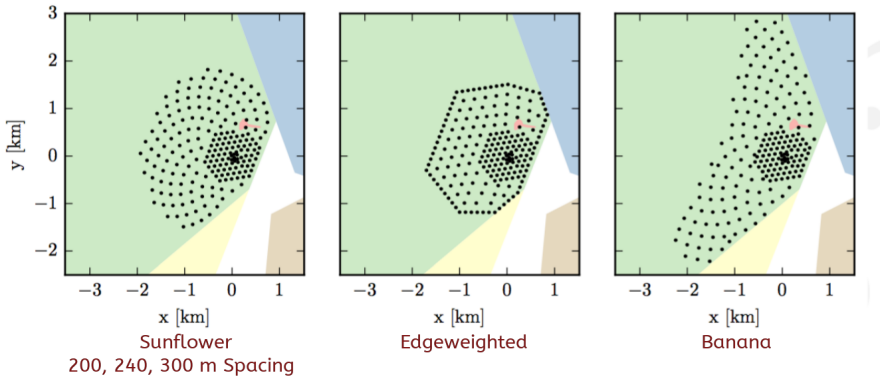

Figure 7.11: Different proposed string placement geometries for IceCube-Gen2. (left) Sunflower geometry considered with 200, 240 and 300 m mean string spacing. (center) Edge weighted geometry for better vetoing. (right) Banana shaped geometry. Figure taken from [45]

For the simulation, 5×10^5 muon events have been generated for each detector geometry. The same events have been used for both the WOM and the pDOM as described in step 1. The energy of the events ranges from 3 TeV to 1 PeV with a power-law index of -1.4. Only events with more than eight modules with photon detections are used. An exemplary event in the sunflower 200 geometry with an energy of $4 \cdot 10^4$ GeV is shown in fig. 7.12. It's a good example for the detection of photons at different times at different PMTs as represented by modules of differently coloured half spheres. The direction of all muon events is random. The corresponding angular distribution is shown in fig. 7.13. The non-flat shape of the distribution is caused by the detector geometry.

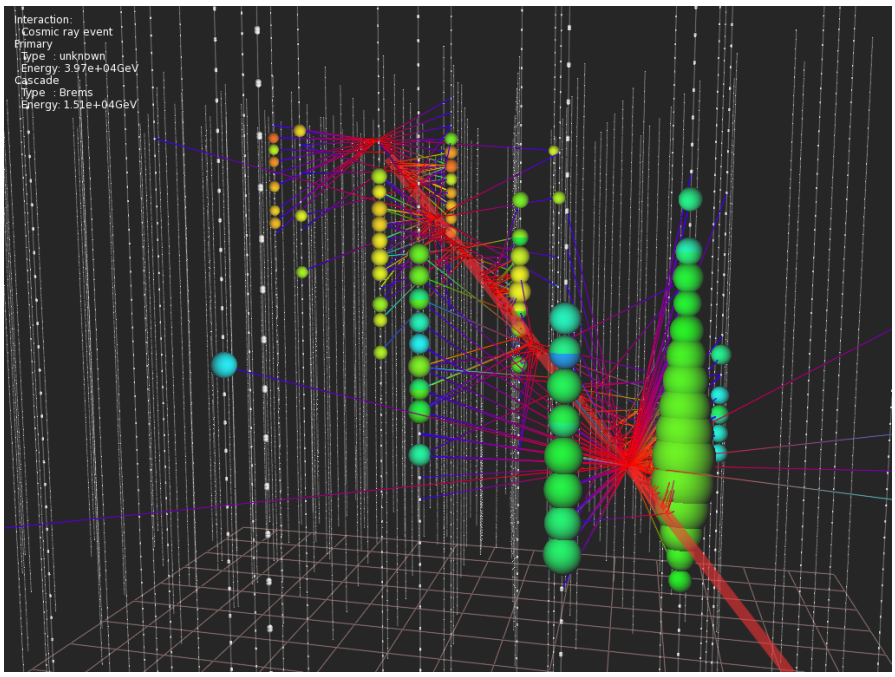

Figure 7.12: Visualisation of a simulated event in the sunflower 200 geometry.

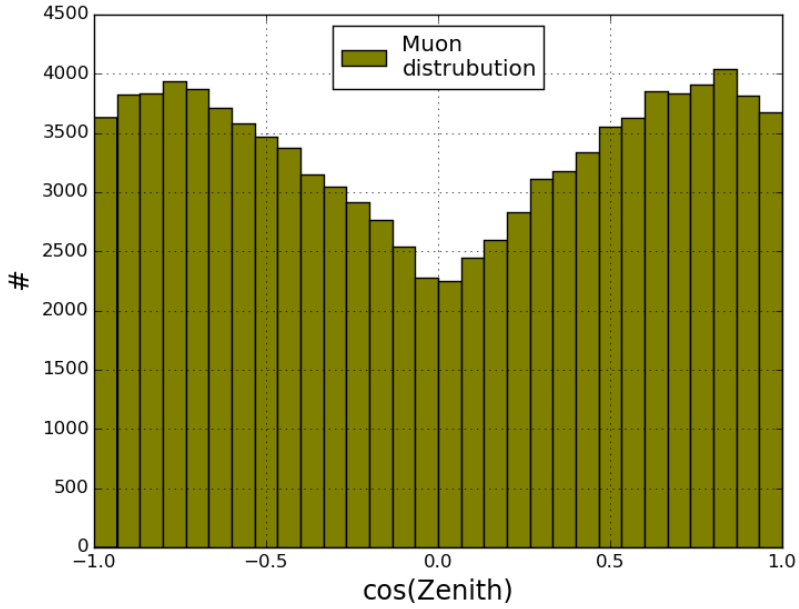

Figure 7.13: Angular distribution of simulated muons.

The first parameter of interest is the number of OMs that detected at least a single photon. The corresponding plot is displayed in fig. 7.14. As expected the number of OMs that are hit on average per event rises with energy since more photons are produced. The number rises faster for the pDOM than for the WOM. Since the WOM is more sensitive to UV-light which is absorbed faster in ice than visible light,[5] the visible photons that are detected by pDOMs travel further and consequently more pDOMs are hit. It must be taken into account, that there are more UV-photons that might produce more detections per module for the fewer WOMs that are hit.

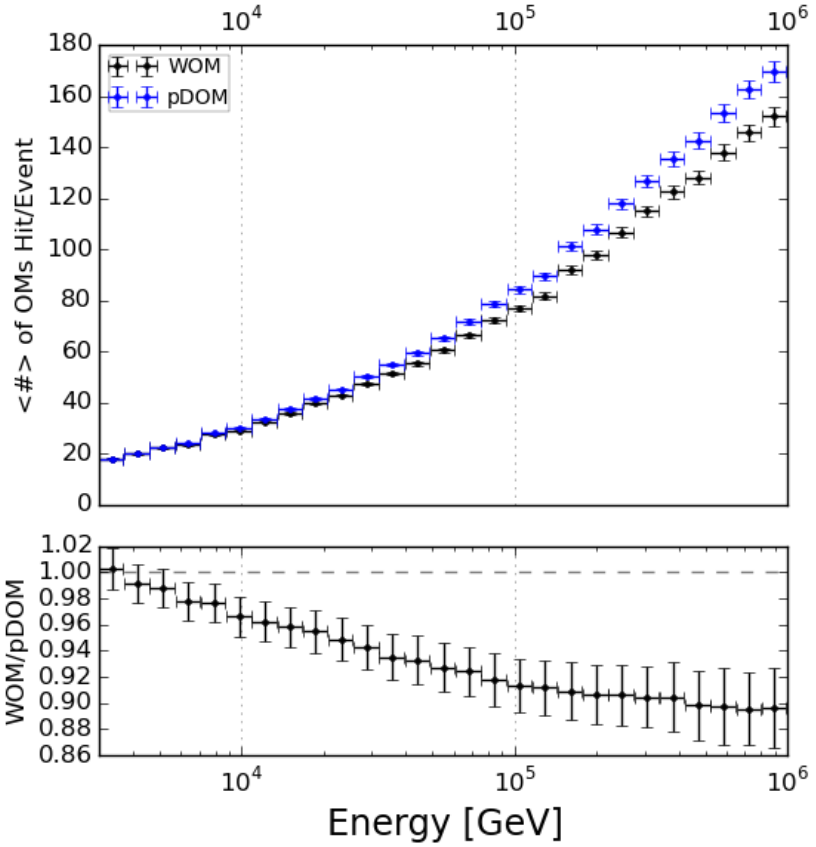

Figure 7.14: The number of OMs hit per event on average as a function of energy for the sunflower 240 geometry. This measure is not scaled with the correction factor since it does not scale linearly.

[5] According to current measurements and the ice model used. See also fig. 2.5.

To investigate this, the number of photons detected per event on average is shown in fig. 7.15 as a function of muon energy. It can be concluded that the number of OMs that detect a photon does not influence the total number of photons that are detected. The WOMs detect therefore more photons than the pDOMs in total. The number of photons rises linearly with energy. The slope is identical for pDOM and WOM, allowing the conclusion that the WOM in this scenario is 1.05 ± 0.07 times more efficient in detecting Cherenkov photons. This includes a statistical error based on the simulation. Uncertainties on the data used for the modelling are not included.

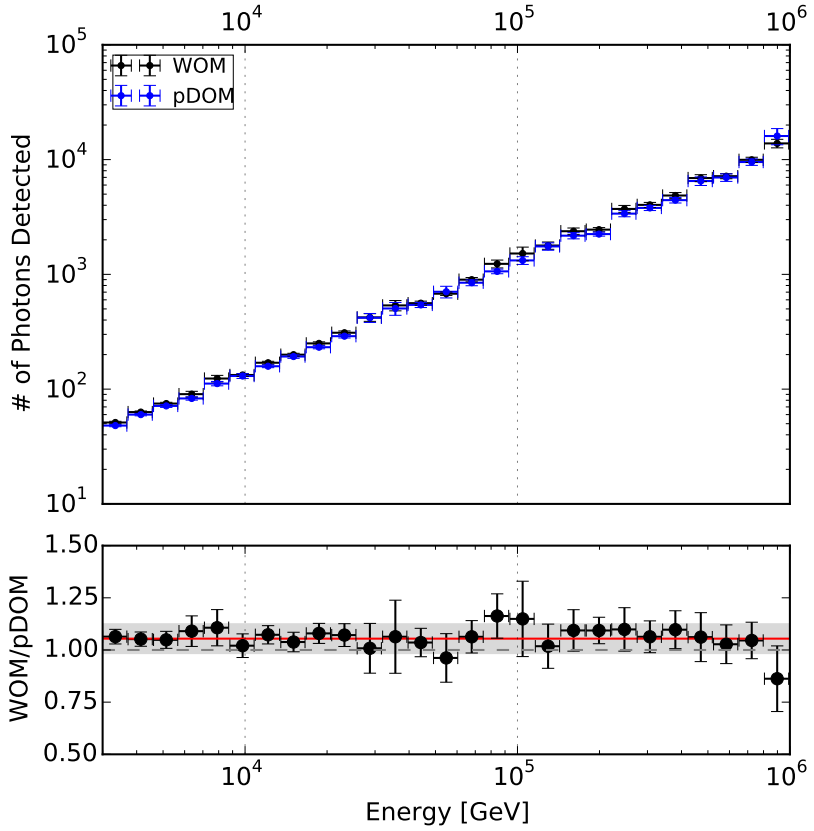

Figure 7.15: The number of detected photons as a function of muon energy for the sunflower 240 geometry.

In the following the detection behaviour as a function of distance as shown in fig. 7.16 is investigated. In this context, the distance is the shortest distance of the muon track to the OM in question. Counted are the number of photons per OM and per event on average. Since the events have different energies and thus different photon counts independent of distance, the counts are normalized by the energy of the individual events. This correction is possible since the number of photon counts scales linearly with the energy as seen before. For the WOM and the pDOM, the expected decrease with distance can be seen. For the ratio, it can be seen that the WOM decreases in relative efficiency with larger distances due to the higher UV absorption of ice. Nevertheless, the WOM outperforms the DOM within one string distance for most of the geometries investigated. The larger statistical error of the ratios towards larger distances is caused by the lower statistics in comparison to the other data points. The smaller value at 10 m and the larger statistical error, however, cannot be explained by smaller statistics and needs further investigation.

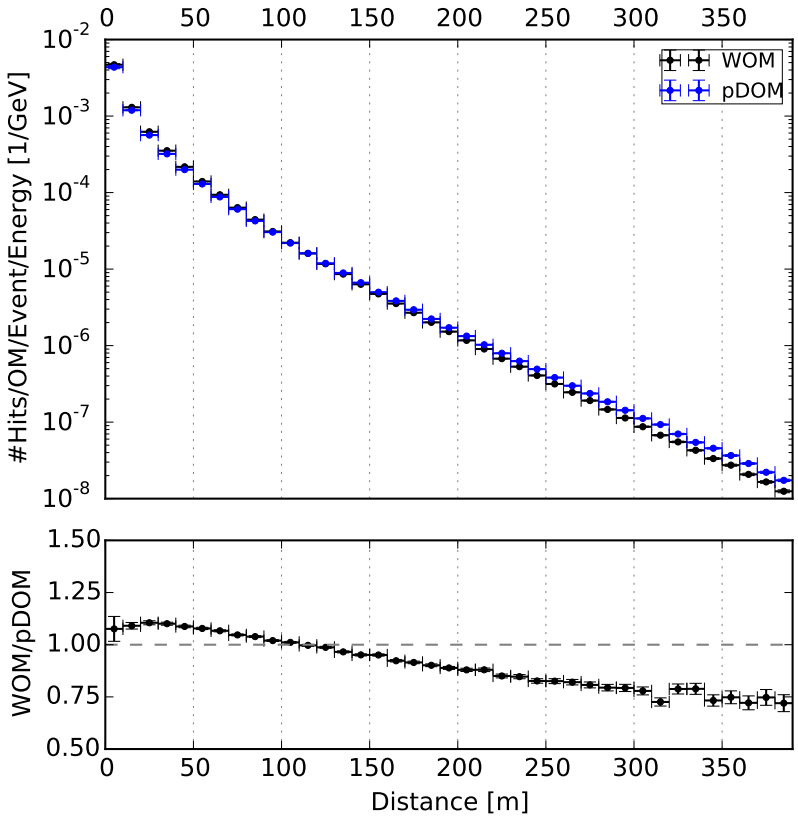

Figure 7.16: The number of photons detected as a function of distance per OM and event for the sunflower 240 geometry. Corrected with the event energy. Below the ratio between both modules.

It is suspected that the larger error is related to a larger variance between different directions caused by the differences in directional acceptances of the WOM and the pDOM. To test this hypothesis the same data is separated into three different polar angle regions of the incoming muon as shown in fig. 7.17. The functions deviate a lot from each other for short distances and different muon directions. This shows that the decrease in the ratio and the increase in error at 10 m is indeed caused by the different directional sensitivity of the OMs.

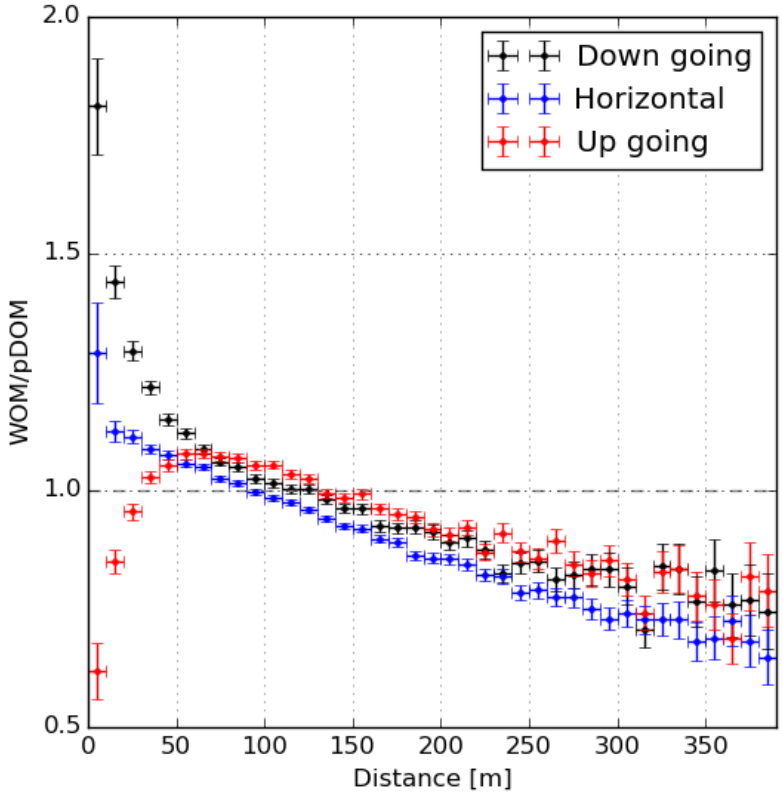

Figure 7.17: The ratio between pDOM and WOM of the number of photons detected as a function of distance per OM and event for the sunflower 240 geometry for 3 different muon direction ranges.

In fig. 7.18 (left) the photon arrival time is shown. The time is relative to the minimally possible arrival time at that OM position based on the particle track. A small overlap to negative times is caused by the finite size of the OMs and secondary particles produced by the muon. It can be seen that the distribution for the WOM is broader than for the pDOM. This is expected since the WOM produces a broader time spread due to the WLS decay time and the photon transport in the PMMA tube. The time offset of the distribution is an arbitrary parameter and depends on the function definition in the modelling as shown in fig. 7.9. It should be kept in mind that with a more realistic time modelling the timing distributions will be a bit wider since currently the tail of the timing distribution is mostly ignored. For the directional reconstruction, especially the arrival time of the first photon in an OM is important. Those are displayed in fig. 7.18 (right) with the limit to OMs within 240 m of the muon track. For the final reconstruction this arrival time distribution for different possible OM to track distances is used for all OMs, the measured times are then fitted to the distributions to determine the track position.

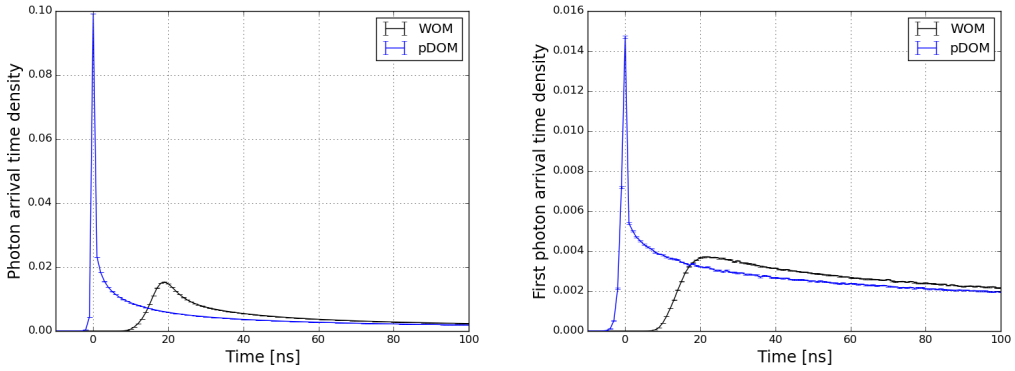

Figure 7.18: (left) Photon arrival time distribution relative to the minimum arrival time possible for the given muon-track to OM distance. (right) Same as left but only for the first photon per OM. The time offset of the distribution is an arbitrary side effect of the function definition.

7.5 Results

In this chapter, the IceCube simulation framework was introduced as well as a specific simulation chain used to compare the WOM and the pDOM. Furthermore, it was illustrated how a simplified model of the WOM was incorporated into the simulation framework. For the model, the angular acceptance was derived from theory. Other components like the position-dependent efficiency, the wavelength-dependent efficiency and the timing behaviour were derived from measurements.

With the adapted framework, simulations with the WOM and the pDOM were performed in different IceCube-Gen2 geometries. While the detector geometry had no direct influence on the investigated parameters, the individual properties of the two OMs showed a clear effect. The timing distributions for the pDOM were much narrower than for the WOM, also more pDOMs at large distances from the track detect photons than WOMs. The first effect is clearly caused by the better timing resolution of the pDOM and the second by the larger absorption of UV-photons in the ice, those which the WOM is more sensitive to. Yet the WOMs detects on average 1.05 ± 0.07 times more photons than the pDOMs

in total.[6] Furthermore, a clear difference in directional sensitivity between the modules was observed. This is to be expected due to the DOM facing downwards and the WOM sideways.

With these results, it can not be said that either OM exceeds the other in all points. The superior detector can only be determined on basis of a use case and its required parameters. A final evaluation of those will also require the implementation of a full reconstruction of the events. Yet it is remarkable that even though the WOM performed, in the measurements, much worse than expected, it is still compatible in the total number of photons detected, leaving room for improvements. Not considered in the simulation was the adiabatic light guide and the possibility of an additional increase in efficiency by matching the refractive index between pressure-vessel and WLS-tube n_{fill}.

[6] The data used to model the position-dependent efficiency is based on the outdated 2Gauss+Exp method with an average efficiency of 28.6 ± 1.4 %. The current best measurement (section 5.4.5) yields 28.1 ± 0.5 % efficiency. Considering linear scaling, the current best estimate is relative about 1.78 % lower.

CHAPTER 8

Conclusion

8.1 Results

A basic proof of concept for the WOM and the development of a WLS-paint suiting the requirements of the WOM preceded the work presented in this thesis [86]. The tasks scheduled to follow were: up-scaling the proof of concept, measuring as well as understanding the performance parameters and deployment of a prototype. New results and unexpected obstacles made it necessary to deviate from that schedule. The previously used 2 cm diameter tubes were abandoned and a full-scale optical prototype with a 9 cm tube diameter, adiabatic light guides, and exterior pressure vessel was successfully built. While the scaling-up itself was unproblematic, the measured efficiencies were much lower than expected. The lower efficiency values caused a stronger than intended focus on understanding and modelling the performance parameters. In addition, delayed or unavailable measurement equipment complicated these efforts. For this and several other reasons unrelated to the WOM, a prototype was not deployed yet. To emulate the results from a possible deployment several full detector simulations were performed with the WOM.

Early investigations showed that previous measurement results underestimated the total efficiency of the WLS-tubes to an unknown degree. This was due to a matching problem with the refractive indexes in the photodiodes used. In response, a PMT measurement setup was built and used from that point onwards. Several methods to evaluate these measurements were introduced and evaluated. Early measurements showed WLS-tube efficiencies of 51 ± 3 % on small tubes. However, even though these results were reproducible, they should be noted with caution. They only apply to small 2 cm diameter tubes at 30 cm length. Furthermore, a fair number of systematic uncertainties have been found to be related to these measurements. Those uncertainties were mostly caused by or related to the equipment used at that time.

The behaviour in cold conditions was evaluated and only a relative reduction of ≈ 6 % in efficiency compared to room temperature measurements was found. This reduction falls well into the realm of systematic uncertainties.

A coating setup was designed and built for large (9 cm diameter) tubes. An initial comparison of cast and extruded tubes showed extruded tubes performed significantly worse than cast tubes. A first prototype including adiabatic light guides was produced and its efficiency measured. The measured efficiency of the optical prototype was 13.0 ± 5.5 %. The much lower efficiency is at least partially

related to the adiabatic light guide. With a new data acquisition system (ADQ14) it was possible to make more elaborate and accurate measurements. The current best WLS-tube efficiency,[1] for large 9 cm diameter tubes, was determined to be 28.1 ± 5.4 %. Some systematic uncertainties remain. Resolving these uncertainties turned out to be difficult as many of them cannot be clearly separated from one another and are likely of similar size. The timing distributions for large tubes were measured with an approximate FWHM of 8 ns. Overall many improvements in terms of measurement setup, evaluation techniques and general understanding have been made. Yet the complexity of the systematic uncertainties precludes a reliable and conclusive result.

To improve the understanding of the physical processes in the WLS-tube, a model for the light capture and propagation in the WLS-tube was suggested and compared to measured data. The model describes the data well. The current best fit results are 3.1 ± 0.4 m loss length, 1.37 ± 0.06 ns decay time, and 73 ± 3 % capture efficiency, results that agree with literature values. The results indicate that most of the efficiency is lost due to propagation losses within the tube.

A simplified model of the WOM was incorporated into the IceCube simulation framework. With this framework, the WOM and the pDOM were compared for different IceCube-Gen2 geometries. The detector geometry had no direct influence on the investigated parameters, though the individual properties of the two OMs had a clear effect in the results. Due to the WLS decay time, the timing distributions for the pDOM were much narrower than for the WOM. Since ice absorbs UV light better than blue light, at large distances from the track more pDOMs detect photons than WOMs do. Yet in total, the WOMs detect on average 1.05 ± 0.07 times more photons than the pDOMs.[2] Furthermore, a clear difference in directional sensitivity between the modules was observed. This is to be expected due to the pDOM facing downwards and the WOM sideways. Neither OM is clearly superior to the other, this can only be determined based on a use case and its required parameters. Overall the results from the determined efficiencies were rather disappointing. However, the WOM is still competitive with the pDOM. Including the lower price point and likely further improvements gives the WOM an edge over the pDOM.

At this point, the development of the WOM has not contributed to the field of astroparticle physics. With additional development, a prototype can be deployed in ice in the near future and thus the WOM has good potential to contribute to astroparticle physics in the future. At the same time, new opportunities arise to contribute to the field of particle physics since the concept is being adapted and evaluated to be used in SHiP [124].

[1] Averaged over the entire length

[2] Considering linear scaling, the current best estimate is relative about 1.78 % lower.

8.2 Outlook

Two things can and should happen with the WOM in the future. The first is the deployment of a prototype in ice and the second is additional improvements. This last section focuses on the latter. Improvements can happen in our understanding of the properties of the WOM as well as in terms of increases in efficiency. Both of these things are strongly correlated with one another. To improve efficiency, matching the refractive index of the material that fills the space between the pressure vessel and WLS-tube is highly recommended. Good matching might increase module efficiency by more than 50 %. Beyond that, the adiabatic light guide has been shown to be problematic, both in terms of efficiency and combining it with the WLS-tube. This is further supported by the simulations performed at the University of Mainz [117]. Therefore, it is recommended to avoid using the adiabatic light guide. This could be done by increasing the PMT diameter or using multiple smaller rods or tubes and PMTs to assemble a bigger tube-like structure in the WOM. If a sufficiently pressure-resistant material with a high refractive index that can be doped with WLS is found, even a monolithic centerpiece without a pressure vessel could be used.

To understand and evaluate the systematic uncertainties it is necessary to take more measurements in a faster and more accurate manner. The availability of the ADQ14 enables higher data taking rates and better accuracy. A portal scanner will further automate data taking and thus increase accuracy and data taking rates further. The last step will be a more accurate light source. Both the portal scanner and the light source should be available by now. Besides the evaluation of many more WLS-tubes, controlling for various parameters, such as coating speed, orientation etc., the tube material needs to be evaluated as well. The modelling indicated that most of the losses occur during the photon transport in the WLS-tube. Reducing these losses must be a priority. Using the current solvent-based paint might produce a microporous surface. A possibility to avoid this could be a glossy paint, that is usually made from two components with no or less solvent. Though it might be challenging to dissolve the WLS in a non-solvent-based paint. A re-evaluation of the necessary paint viscosity and layer thickness on the tube is recommendable as well. Since the latest results with large tubes did show discrepancies to earlier results on microscope slides and small tubes. Using a substrate (tube or rod material) with better optical properties might further increase efficiency.

The current modelling approach can be useful to generate data to interpolate from in an improved simulation. Beyond that, its ability to further the understanding of the physical properties of the WLS-tubes seems exhausted. To obtain additional insights, photon scattering should be accounted for. Computationally this is beyond the current implementation. A professional ray tracing software or GPU implementation might be able to facilitate multiple computing cores to achieve this within a reasonable amount of time. A promising approach of this has meanwhile become available, with results similar to those presented in this thesis [116].

Currently, the possibility exists to fully simulate any IceCube like detector using the WOM as the main optical module. The underlying data used to model the WOM in this is partially outdated. It is recommended to create a new description based on the output of the model described in chapter six. This will remove the need to extrapolate for boundary values and allow for a better description of the timing behaviour. Currently, no reconstruction based on the WOM has been implemented. The reconstruction currently used in IceCube is based on spline tables. Generating these spline tables requires a large number of simulation datasets. With spherical modules like the DOM and the pDOM oversizing is used to reduce the necessary simulation time. Oversizing is currently not available for

the WOM. To avoid large computation times and costs it is recommended to implement this first or implement an alternative reconstruction. This could be based on convolutional neural networks (as in [125]), possibly improved by the use of Bayesian Neural Networks. Neural networks could potentially reduce the required data set but will ultimately benefit from oversizing as well. Only the possibility to reconstruct events will allow for a final evaluation of the data quality that can be achieved with the WOM.

It is the firm belief of the author of this thesis that it should be possible to further increase the efficiency of the WOM in the future. The WOM should be able to compete with the best alternative optical modules such as the IceCube mDOM and the D-Egg. To accomplish this a large and systematic effort from the institutions involved in the WOM is needed. Further, it is a great joy to the author of this thesis to see a first WOM prototype being deployed at the Cascadia Basin (in the ocean of the North-American west-coast) as shown in fig. 8.1. Further descriptions on that can be found at [126].

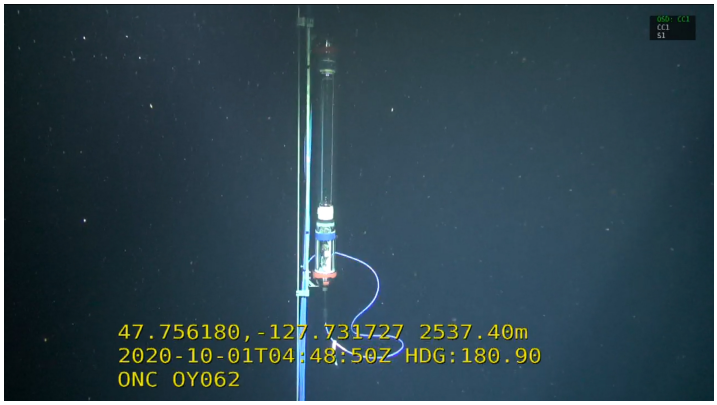

Figure 8.1: Underwater image of the first deployed WOM prototype. The image was supplied by Prof. Dr. Lutz Koepke, the creator of the video that is the source of the image is unknown.

Bibliography

[1] L. M. Brown, *The idea of the neutrino*, Physics Today **31** (1978) 23 (cit. on p. 3).

[2] C. L. Cowan et al., *Detection of the Free Neutrino: a Confirmation*, Science **124** (1956) 103, ISSN: 0036-8075,
eprint: http://science.sciencemag.org/content/124/3212/103.full.pdf,
URL: http://science.sciencemag.org/content/124/3212/103 (cit. on p. 3).

[3] Cush, *Standard Model of Elementary Particles Anti*,
https://commons.wikimedia.org/wiki/File:
Standard_Model_of_Elementary_Particles_Anti.svg,
[Online; accessed 03-December-2018], 2018 (cit. on p. 3).

[4] C. Giganti, S. Lavignac and M. Zito, *Neutrino oscillations: the rise of the PMNS paradigm*, Prog. Part. Nucl. Phys. **98** (2018) 1, arXiv: 1710.00715 [hep-ex] (cit. on p. 3).

[5] M. Tanabashi et al., *Review of Particle Physics*, Phys. Rev. D **98** (3 2018) 030001,
URL: https://link.aps.org/doi/10.1103/PhysRevD.98.030001 (cit. on p. 3).

[6] F. Couchot et al.,
Cosmological constraints on the neutrino mass including systematic uncertainties,
Astron. Astrophys. **606** (2017) A104, arXiv: 1703.10829 [astro-ph.CO] (cit. on p. 3).

[7] G. B. Franklin, "The KATRIN Neutrino Mass Measurement: Experiment, Status, and Outlook",
13th Conference on the Intersections of Particle and Nuclear Physics (CIPANP 2018) Palm Springs, California, USA, May 29-June 3, 2018, 2018,
arXiv: 1809.10603 [physics.ins-det] (cit. on p. 4).

[8] P. J. Doe et al., "Project 8: Determining neutrino mass from tritium beta decay using a frequency-based method",
Proceedings, 2013 Community Summer Study on the Future of U.S. Particle Physics: Snowmass on the Mississippi (CSS2013): Minneapolis, MN, USA, July 29-August 6, 2013, 2013, arXiv: 1309.7093 [nucl-ex], URL: http://www.slac.stanford.edu/econf/C1307292/docs/submittedArxivFiles/1309.7093.pdf (cit. on p. 4).

[9] K. Blaum et al., "The Electron Capture ^{163}Ho Experiment ECHo",
The Future of Neutrino Mass Measurements: Terrestrial, Astrophysical, and Cosmological Measurements in the Next Decade (NUMASS2013) Milano, Italy, February 4-7, 2013, 2013,
arXiv: 1306.2655 [physics.ins-det] (cit. on p. 4).

[10] M. Singh, *Prospects for the Mass Ordering (MO) and θ_{23}-Octant sensitivity in LBL experiments: UNO, DUNE & NOvA*, (2017), arXiv: 1706.06473 [hep-ph] (cit. on p. 4).

[11] K. Abe et al., *Hyper-Kamiokande Design Report*, (2018),
arXiv: 1805.04163 [physics.ins-det] (cit. on p. 4).

[12] S. Adrian-Martinez et al., *Letter of intent for KM3NeT 2.0*, J. Phys. **G43** (2016) 084001,
arXiv: 1601.07459 [astro-ph.IM] (cit. on pp. 4, 10, 18).

[13] C. W. Walter, *The Super-Kamiokande Experiment*, (2008) 19, arXiv: 0802.1041 [hep-ex] (cit. on pp. 4, 9).

[14] M. G. Aartsen et al., "The IceCube Neutrino Observatory : Instrumentation and Online Systems The IceCube Collaboration", 2017 (cit. on pp. 4, 9, 17).

[15] G. Boireau et al., *Online Monitoring of the Osiris Reactor with the Nucifer Neutrino Detector*, Phys. Rev. **D93** (2016) 112006, arXiv: 1509.05610 [physics.ins-det] (cit. on p. 4).

[16] V. Papadimitriou et al., "Design of the LBNF Beamline", *Proceedings, 7th International Particle Accelerator Conference (IPAC 2016): Busan, Korea, May 8-13, 2016*, 2016 TUPMR025, arXiv: 1704.04471 [physics.acc-ph], URL: http://lss.fnal.gov/archive/2016/conf/fermilab-conf-16-163-ad.pdf (cit. on p. 4).

[17] D. Szam, *Proton proton cycle*, https://commons.wikimedia.org/wiki/File:Proton_proton_cycle.svg, [Online; accessed 03-December-2018], 2012 (cit. on p. 5).

[18] R. M. Bionta et al., *Observation of a neutrino burst in coincidence with supernova 1987A in the Large Magellanic Cloud*, Phys. Rev. Lett. **58** (14 1987) 1494, URL: https://link.aps.org/doi/10.1103/PhysRevLett.58.1494 (cit. on p. 5).

[19] M. G. Aartsen et al., *Evidence for High-Energy Extraterrestrial Neutrinos at the IceCube Detector*, Science **342** (2013) 1242856, arXiv: 1311.5238 [astro-ph.HE] (cit. on pp. 5, 18).

[20] M. G. Aartsen et al., *Neutrino emission from the direction of the blazar TXS 0506+056 prior to the IceCube-170922A alert*, Science **361** (2018) 147, arXiv: 1807.08794 [astro-ph.HE] (cit. on pp. 5, 18).

[21] G. Duda, G. Gelmini and S. Nussinov, *Expected signals in relic neutrino detectors*, Phys. Rev. **D64** (2001) 122001, arXiv: hep-ph/0107027 [hep-ph] (cit. on p. 5).

[22] N. Aghanim et al., *Planck 2018 results. VI. Cosmological parameters*, (2018), arXiv: 1807.06209 [astro-ph.CO] (cit. on p. 5).

[23] B. Audren et al., *Robustness of cosmic neutrino background detection in the cosmic microwave background*, JCAP **1503** (2015) 036, arXiv: 1412.5948 [astro-ph.CO] (cit. on p. 5).

[24] C. Spiering, *Towards high-energy neutrino astronomy*, The European Physical Journal H **37** (2012) 515, ISSN: 2102-6467, URL: https://doi.org/10.1140/epjh/e2012-30014-2 (cit. on p. 6).

[25] A. Donini, S. Palomares-Ruiz and J. Salvado, *Neutrino tomography of the Earth*, (2018), arXiv: 1803.05901 [hep-ph] (cit. on p. 5).

[26] A. J. Macleod, A. Noble and D. A. Jaroszynski, *Cherenkov radiation from the quantum vacuum*, (2018), arXiv: 1810.05027 [hep-ph] (cit. on p. 6).

[27] P. Genevet et al., *Controlled steering of Cherenkov surface plasmon wakes with a one-dimensional metamaterial*, Nature Nanotechnology **10** (2015) 804, URL: https://doi.org/10.1038/nnano.2015.137 (cit. on p. 7).

[28] P. Vogel and J. F. Beacom, *Angular distribution of neutron inverse beta decay, $\overline{\nu}_e + \overrightarrow{p} \; e^+ + n$*, Phys. Rev. D **60** (5 1999) 053003, URL: https://link.aps.org/doi/10.1103/PhysRevD.60.053003 (cit. on p. 8).

[29] A. Faessler et al., *Beta Decay and the Cosmic Neutrino Background*, EPJ Web of Conferences **71** (2014) 00044, ed. by L. Bravina, Y. Foka and S. Kabana, URL: https://doi.org/10.1051/epjconf/20147100044 (cit. on p. 8).

[30] A. G. Cocco, *PTolemy - Towards Cosmological Relic Neutrino detection*, PoS **NOW2016** (2017) 092 (cit. on p. 9).

[31] B. T. Cleveland et al., *Measurement of the Solar Electron Neutrino Flux with the Homestake Chlorine Detector*, The Astrophysical Journal **496** (1998) 505, URL: http://stacks.iop.org/0004-637X/496/i=1/a=505 (cit. on p. 9).

[32] J. N. Abdurashitov et al., *Solar neutrino flux measurements by the Soviet-American Gallium Experiment (SAGE) for half the 22 year solar cycle*, J. Exp. Theor. Phys. **95** (2002) 181, [Zh. Eksp. Teor. Fiz.122,211(2002)], arXiv: astro-ph/0204245 [astro-ph] (cit. on p. 9).

[33] C. L. Cowan et al., *Detection of the Free Neutrino: a Confirmation*, Science **124** (1956) 103, URL: https://doi.org/10.1126/science.124.3212.103 (cit. on p. 9).

[34] G. Alimonti et al., *The Borexino detector at the Laboratori Nazionali del Gran Sasso*, Nucl. Instrum. Meth. **A600** (2009) 568, arXiv: 0806.2400 [physics.ins-det] (cit. on p. 9).

[35] A. A. Aguilar-Arevalo et al., *The MiniBooNE Detector*, Nucl. Instrum. Meth. **A599** (2009) 28, arXiv: 0806.4201 [hep-ex] (cit. on p. 9).

[36] P. Allison et al., *Performance of two Askaryan Radio Array stations and first results in the search for ultrahigh energy neutrinos*, Phys. Rev. **D93** (2016) 082003, arXiv: 1507.08991 [astro-ph.HE] (cit. on p. 10).

[37] P. W. Gorham et al., *The Antarctic Impulsive Transient Antenna Ultra-high Energy Neutrino Detector Design, Performance, and Sensitivity for 2006-2007 Balloon Flight*, Astropart. Phys. **32** (2009) 10, arXiv: 0812.1920 [astro-ph] (cit. on p. 10).

[38] C. W. James et al., *The lunar Askaryan technique with the Square Kilometre Array*, PoS **ICRC2015** (2015) 291, arXiv: 1608.02408 [astro-ph.IM] (cit. on p. 10).

[39] A. D. Avrorin et al., *Baikal-GVD: status and prospects*, EPJ Web Conf. **191** (2018) 01006, arXiv: 1808.10353 [astro-ph.IM] (cit. on pp. 10, 18).

[40] *The Detection of Neutrinos in IceCube*, [Online; accessed 05-December-2018], URL: https://masterclass.icecube.wisc.edu/en/learn/detecting-neutrinos (cit. on pp. 11, 12).

[41] J. Stachurska, *First Double Cascade Tau Neutrino Candidates in IceCube and a New Measurement of the Flavor Composition*, PoS **ICRC2019** (2020) 1015, arXiv: 1908.05506 [astro-ph.HE] (cit. on p. 11).

[42] P. Hallen, *On the Measurement of High-Energy Tau Neutrinos with IceCube*, M.Sc. Thesis, 2013, URL: https://www.institut3b.physik.rwth-aachen.de/global/show_document.asp?id=aaaaaaaaaapwhzq (cit. on p. 11).

[43] M. Aartsen et al., *The IceCube Neutrino Observatory: Instrumentation and Online Systems*, JINST **12** (2017) P03012, arXiv: 1612.05093 [astro-ph.IM] (cit. on p. 13).

[44] J. A. Aguilar Sanchez, *Search for Dark Matter and BSM Physics with the IceCube Neutrino Observatory*, PoS **NuFact2019** (2020) 110 (cit. on p. 13).

[45] T. I. collaboration, Internal documents or presentations. (cit. on pp. 13, 14, 18–20, 22, 24, 101).

[46] R. Abbasi et al., *Calibration and characterization of the IceCube photomultiplier tube*, Nuclear Instruments and Methods in Physics Research A **618** (2010) 139, arXiv: 1002.2442 [astro-ph.IM] (cit. on pp. 14–16, 51, 54).

[47] P. B. Price et al., *Temperature profile for glacial ice at the South Pole: Implications for life in a nearby subglacial lake*, Proceedings of the National Academy of Sciences **99** (2002) 7844, URL: https://doi.org/10.1073/pnas.082238999 (cit. on p. 15).

[48] M. Ackermann et al., *Optical properties of deep glacial ice at the South Pole*, Journal of Geophysical Research **111** (2006), URL: http://dx.doi.org/10.1029/2005JD006687 (cit. on pp. 15–18).

[49] *List of Historic Sites and Monuments approved by the ATCM (2012)*, [Online; accessed 10-December-2018], 2012, URL: http://www.ats.aq/documents/ATCM35/WW/atcm35_ww003_e.pdf (cit. on p. 15).

[50] P. Askebjer et al., *Optical properties of deep ice at the South Pole: Absorption*, Applied optics **36** (1997) 4168 (cit. on p. 16).

[51] P. B. Price, K. Woschnagg and D. Chirkin, *Agevsdepth of glacial ice at South Pole*, Geophysical Research Letters **27** (2000) 2129, URL: https://doi.org/10.1029/2000gl011351 (cit. on p. 16).

[52] M. Rongen, R. Bay and S. Blot, *Observation of an optical anisotropy in the deep glacial ice at the geographic South Pole using a laser dust logger*, The Cryosphere **14** (2020) 2537 (cit. on p. 17).

[53] M. R. et al., *Measuring the optical properties of IceCube drill holes*, EPJ Web of Conferences **116** (2016) 06011, ed. by A. Capone et al., URL: https://doi.org/10.1051/epjconf/201611606011 (cit. on p. 17).

[54] R. J. Wilkes, *DUMAND and AMANDA: High-energy neutrino astrophysics*, eConf **C940808** (1994) 017, [,301(1994)], arXiv: astro-ph/9412019 [astro-ph] (cit. on p. 17).

[55] I. Belolaptikov et al., *Results from the Baikal underwater telescope*, Nuclear Physics B - Proceedings Supplements **43** (1995) 241, URL: https://doi.org/10.1016/0920-5632(95)00481-n (cit. on p. 17).

[56] M. Ageron et al., *ANTARES: The first undersea neutrino telescope*, Nuclear Instruments and Methods in Physics Research A **656** (2011) 11, arXiv: 1104.1607 [astro-ph.IM] (cit. on p. 17).

[57] M. G. Aartsen et al., *Cosmic ray spectrum and composition from PeV to EeV using 3 years of data from IceTop and IceCube*, Physical Review D **100** (2019), ISSN: 2470-0029, URL: http://dx.doi.org/10.1103/PhysRevD.100.082002 (cit. on p. 18).

[58] M. G. Aartsen et al.,
Measurement of Atmospheric Neutrino Oscillations at 6–56 GeV with IceCube DeepCore,
Physical Review Letters **120** (2018), ISSN: 1079-7114,
URL: http://dx.doi.org/10.1103/PhysRevLett.120.071801 (cit. on p. 18).

[59] M. G. Aartsen et al., *Search for neutrinos from dark matter self-annihilations in the center of the Milky Way with 3 years of IceCube/DeepCore*, The European Physical Journal C **77** (2017), ISSN: 1434-6052, URL: http://dx.doi.org/10.1140/epjc/s10052-017-5213-y (cit. on p. 18).

[60] F. Lauber, *Ongoing magnetic monopole searches with IceCube*,
EPJ Web of Conferences **182** (2018) 02071, ed. by Y. Aharonov, L. Bravina and S. Kabana, ISSN: 2100-014X, URL: http://dx.doi.org/10.1051/epjconf/201818202071 (cit. on p. 18).

[61] M. G. Aartsen et al.,
IceCube-Gen2: A Vision for the Future of Neutrino Astronomy in Antarctica, (2014),
arXiv: 1412.5106 [astro-ph.HE] (cit. on p. 19).

[62] M. Aartsen et al., *Neutrino astronomy with the next generation IceCube Neutrino Observatory*, (2019), arXiv: 1911.02561 [astro-ph.HE] (cit. on p. 19).

[63] T. Bretz et al.,
A compact and light-weight refractive telescope for the observation of extensive air showers,
Journal of Instrumentation **13** (2018) P07024, arXiv: 1804.01781 [astro-ph.IM] (cit. on p. 21).

[64] Ara Collaboration et al., *Design and initial performance of the Askaryan Radio Array prototype EeV neutrino detector at the South Pole*, Astroparticle Physics **35** (2012) 457, arXiv: 1105.2854 [astro-ph.IM] (cit. on p. 21).

[65] A. Anker et al., *Targeting ultra-high energy neutrinos with the ARIANNA experiment*, Adv. Space Res. **64** (2019) 2595, arXiv: 1903.01609 [astro-ph.IM] (cit. on p. 21).

[66] A. Ishihara, *The IceCube Upgrade – Design and Science Goals*, PoS **ICRC2019** (2020) 1031, arXiv: 1908.09441 [astro-ph.HE] (cit. on pp. 21, 24, 25).

[67] M. G. Aartsen et al.,
Letter of Intent: The Precision IceCube Next Generation Upgrade (PINGU), (2014),
arXiv: 1401.2046 [physics.ins-det] (cit. on pp. 21, 23).

[68] R. Nagai and A. Ishihara, *Electronics Development for the New Photo-Detectors (PDOM and D-Egg) for IceCube-Upgrade*, PoS **ICRC2019** (2019) 966 (cit. on pp. 23, 24).

[69] A. Ishihara et al., "Overview and performance of the D-Egg optical sensor for IceCube-Gen2",
Proceedings of 35th International Cosmic Ray Conference — PoS(ICRC2017),
Sissa Medialab, 2017, URL: https://doi.org/10.22323/1.301.1051 (cit. on p. 24).

[70] A. Stoessl,
Muon track reconstruction and veto performance with D-Egg sensor for IceCube-Gen2,
PoS **ICRC2017** (2018) 1038 (cit. on p. 24).

[71] L. Classen, A. Kappes and T. Karg, *A multi-PMT Optical Module for the IceCube Upgrade*, PoS **ICRC2019** (2020) 855, arXiv: 1908.10802 [astro-ph.HE] (cit. on p. 24).

[72] E. L. and, *The Digital Optical Module of KM3NeT*,
Journal of Physics: Conference Series **1056** (2018) 012031,
URL: https://doi.org/10.1088%2F1742-6596%2F1056%2F1%2F012031 (cit. on p. 24).

[73] L. Classen,
The mDOM – a multi-PMT digital optical-module for the IceCube-Gen2 neutrino telescope,
URL: https://www.uni-muenster.de/imperia/md/content/physik_kp/agkappes/abschlussarbeiten/doktorarbeiten/1702-phd_lclassen.pdf (cit. on pp. 25, 38).

[74] T. Karg, Private communication (cit. on pp. 25, 29, 31).

[75] P. Peiffer and D. Hebecker, *Overview and Performance of the Wavelength-shifting Optical Module (WOM) for IceCube-Gen2*, PoS **ICRC2017** (2017) 1052 (cit. on p. 25).

[76] P. Peiffer, "New optical sensors for IceCube-Gen2",
Hyper-Kamiokande open meeting London, 2016 (cit. on pp. 26, 27).

[77] C. Fruck, F. Henningsen and C. Spannfellner,
The POCAM as self-calibrating light source for the IceCube Upgrade,
PoS **ICRC2019** (2019) 908 (cit. on p. 27).

[78] P. Falke, Private communication (cit. on p. 29).

[79] P. Falke, *Entwicklung eines Lichtkonzentrators basierend auf einer Hohlzylinder Geometrie*,
B.S. Thesis: Universität Bonn, 2014 (cit. on pp. 30, 37, 38).

[80] S. Böser et al., *Detecting extra-galactic supernova neutrinos in the Antarctic ice*,
Astropart. Phys. **62** (2015) 54, arXiv: 1304.2553 [astro-ph.IM] (cit. on p. 30).

[81] B. Müller, *Neutrino Emission as Diagnostics of Core-Collapse Supernovae*,
Annual Review of Nuclear and Particle Science **69** (2019) 253, ISSN: 1545-4134,
URL: http://dx.doi.org/10.1146/annurev-nucl-101918-023434 (cit. on p. 30).

[82] L. Wen et al., *A quantitative approach to select PMTs for large detectors*,
Nuclear Instruments and Methods in Physics Research Section A: Accelerators, Spectrometers, Detectors and Associated Equipment **947** (2019) 162766, ISSN: 0168-9002,
URL: http://dx.doi.org/10.1016/j.nima.2019.162766 (cit. on p. 30).

[83] M. Archinger, Private communication (cit. on p. 32).

[84] [Online; accessed January-2019], URL: https://refractiveindex.info/ (cit. on p. 32).

[85] A. Steuer, Private communication (cit. on pp. 32, 33).

[86] D. Hebecker,
Development of a single photon detector with wavelength shifting and light guiding technology,
M.Sc. Thesis, 2014 (cit. on pp. 32–37, 40, 43, 44, 60, 61, 70, 78, 88, 100, 109, 133).

[87] R. Katoh et al., *Fluorescence Quantum Yield of Aromatic Hydrocarbon Crystals*,
The Journal of Physical Chemistry C **113** (2009) 2961,
URL: https://doi.org/10.1021/jp807684m (cit. on p. 33).

[88] D. Xue-Feng et al., *Measurement of the fluorescence quantum yield of bis-MSB*,
Chinese Physics C **39** (2015) 126001,
URL: http://stacks.iop.org/1674-1137/39/i=12/a=126001 (cit. on pp. 33, 88).

[89] *ArDM meeting Apr 21 2011 - Wavelength shifter material*, [Online; accessed 28-October-2019],
URL: http://darkmatter.ethz.ch:8080/Plone/meetings/ardm-meeting-apr-21-2011/WLSM.pdf (cit. on pp. 33, 88).

[90] H.-L. Xiao et al.,
Study of absorption and re-emission processes in a ternary liquid scintillation system,
Chinese Physics C **34** (2010) 1724,
URL: https://doi.org/10.1088/1674-1137/34/11/011 (cit. on pp. 33, 88).

[91] M. S. S. O. V. Borshchev N. M. Surin and S. A. Ponomarenko,
Highly Efficient Spectral Shifters of Optical Radiation: Design, Properties, and Applications,
INEOS OPEN **2** (2019) 112, URL: https://doi.org/10.32931/io1916r (cit. on p. 33).

[92] H. Iams and B. Salzberg, *The Secondary Emission Phototube*,
Proceedings of the IRE **23** (1935) 55,
URL: https://doi.org/10.1109/jrproc.1935.227243 (cit. on p. 38).

[93] H. Kolanoski and N. Wermes, *Teilchendetektoren*, Springer, 2016,
ISBN: 9783662453490, 9783662453506 (cit. on p. 38).

[94] *Photomultiplier Tubes (PMT)*, [Online; accessed 01-March-2019],
URL: https://www.sense-pro.org/lll-sensors/pmt (cit. on p. 39).

[95] R. S. Busse, *Setup and commissioning of a test stand fordetailed investigations of quantum efficiencycharacteristics of photomultiplier tubes, andinitial studies for IceCube-Gen2*,
URL: http://www.uni-muenster.de/imperia/md/content/physik_kp/agkappes/abschlussarbeiten/masterarbeiten/1703-ma_rbusse.pdf (cit. on p. 38).

[96] *PHOTOMULTIPLIER TUBESAND ASSEMBLIES; FOR SCINTILLATION COUNTING & HIGH ENERGY PHYSICS*, [Online; accessed 01-March-2019], URL: https://www.hamamatsu.com/resources/pdf/etd/High_energy_PMT_TPMZ0003E.pdf (cit. on p. 38).

[97] *R12199*, [Online; accessed 01-March-2019],
URL: https://www.hamamatsu.com/eu/en/product/type/R12199/index.html (cit. on p. 38).

[98] M. Lukasik, Private communication, 2017 (cit. on pp. 39, 41).

[99] B. Bastian, Private communication (cit. on pp. 39, 57).

[100] S. Böser, Private communication (cit. on p. 41).

[101] *Newport/Oriel Cornerstone 260*, [Online; accessed 28-October-2019],
URL: https://www.newport.com/medias/sys_master/images/images/hae/h47/8797226926110/Oriel-Cornerstone-260-User-Manual-RevA.pdf (cit. on p. 43).

[102] *Hamamatsu Si photodiode S1227-1010BQ For UV to visible, precision photometry; suppressed IR sensitivity*, [Online; accessed 28-October-2019], URL:
https://www.hamamatsu.com/eu/en/product/type/S1227-1010BQ/index.html (cit. on p. 43).

[103] *Stanford Research Systems Lock-In Amplifier SR810 & SR830*,
[Online; accessed 09-March-2019],
URL: https://www.thinksrs.com/products/sr810830.html (cit. on p. 43).

[104] A. Looft, *Entwicklung eines Messverfahrens zur Untersuchung der Lichtdurchlässigkeit bei dem Übergang von Wasser über Glas zu Luft*,
B.S. Thesis: Humboldt-Universität zu Berlin, 2015 (cit. on p. 46).

[105] *PDL 800-B Picosecond Pulsed Diode Laser Driver*, [Online; accessed 29-October-2019], URL: https://www.picoquant.com/products/category/picosecond-pulsed-driver/pdl-800-b-picosecond-pulsed-diode-laser-driver (cit. on p. 46).

[106] *8 channel charge integrating ADC, MOD. V 265*, [Online; accessed 16-March-2019], URL: https://wwwusers.ts.infn.it/~rui/univ/Acquisizione_Dati/Manuals/CAEN%20V265%20rev1.pdf (cit. on pp. 47, 56, 124).

[107] *R11265U SERIES / H11934 SERIES*, [Online; accessed 16-March-2019], URL: https://www.hamamatsu.com/resources/pdf/etd/R11265U_H11934_TPMH1336E.pdf (cit. on pp. 48, 58).

[108] E. Bellamy et al.,
Absolute calibration and monitoring of a spectrometric channel using a photomultiplier,
Nuclear Instruments and Methods in Physics Research Section A: Accelerators, Spectrometers, Detectors and Associated Equipment **339** (1994) 468,
URL: https://doi.org/10.1016/0168-9002(94)90183-x (cit. on p. 50).

[109] R. Saldanha et al.,
Model Independent Approach to the Single Photoelectron Calibration of Photomultiplier Tubes,
Nucl. Instrum. Meth. **A863** (2017) 35, arXiv: 1602.03150 [physics.ins-det]
(cit. on pp. 55, 69, 78).

[110] *ADQ14 - multi-channel, 14-bit digitizer*, [Online; accessed 10-November-2019],
URL: https://www.spdevices.com/products/hardware/14-bit-digitizers/adq14
(cit. on pp. 56, 65, 78, 124, 125).

[111] *Cast acrylic versus extruded acrylic*, [Online; accessed 17-November-2019],
URL: https://www.pmma.dk/Acryl_stobt_kontra_ekstruderet.aspx?Lang=en-GB
(cit. on p. 62).

[112] S. Aiello et al.,
Characterisation of the Hamamatsu photomultipliers for the KM3NeT Neutrino Telescope,
Journal of Instrumentation **13** (2018) P05035,
URL: https://doi.org/10.1088%2F1748-0221%2F13%2F05%2Fp05035 (cit. on p. 65).

[113] *Hamamatsu R1924A Photomultiplier tube*, [Online; accessed 28-November-2019],
URL: https://www.hamamatsu.com/resources/pdf/etd/R1924A_TPMH1280E.pdf
(cit. on pp. 65, 124).

[114] B. Bastian, *Characterization of cylindrical wavelength shifting optical light guides. Charakterisierung von zylindrischen wellenlängenschiebenden optischen Lichtleitern.*
M.Sc. Thesis, 2019 (cit. on pp. 76, 77, 79, 132).

[115] S. Gerlach, *Charakterisierung und Bestimmung systematischer Fehler beim Photonachweis mittels wellenlängenschiebender optischer Module*, B.Sc. Thesis, 2015 (cit. on pp. 76, 129).

[116] F. Thomas,
Light propagation simulation for the Wavelength-shifting Optical Module on CUDA GPUs,
M.Sc. Thesis, 2019, URL: https://butler.physik.uni-mainz.de/icecube/thesis/master_Florian_Thomas.pdf (cit. on pp. 78, 87, 111).

[117] R. Schnur,
Optimierung des adiabatischen Lichtleiters für das Wavelength-shifting Optical Module,
Ba.Sc. Thesis, 2020, URL: https://butler.physik.uni-mainz.de/icecube/thesis/bachelor_Ronja_Schnur.pdf (cit. on pp. 78, 111).

[118] M. Bodmer et al.,
Measurement of Optical Attenuation in Acrylic Light Guides for a Dark Matter Detector,
JINST **9** (2014) P02002, arXiv: 1310.6454 [physics.ins-det] (cit. on p. 87).

[119] K. Kleinknecht, *Detectors for Particle Radiation*, 2nd ed., Cambridge University Press, 1998, ISBN: 0521648548 (cit. on p. 87).

[120] J. R. Lakowicz and I. Gryczynski, *Characterization of p-bis(O-methylstyryl) benzene as a lifetime and anisotropy decay standard for two-photon induced fluorescence*,
Biophysical Chemistry **47** (1993) 1, ISSN: 0301-4622,
URL: http://www.sciencedirect.com/science/article/pii/030146229380027G (cit. on p. 87).

[121] J. Koehne et al., *PROPOSAL: A tool for propagation of charged leptons*,
Comput. Phys. Commun. **184** (2013) 2070 (cit. on p. 93).

[122] D. Chirkin, "Evidence of optical anisotropy of the South Pole ice", *Proceedings, 33rd International Cosmic Ray Conference (ICRC2013): Rio de Janeiro, Brazil, July 2-9, 2013* 0580,
URL: http://www.cbpf.br/%7Eicrc2013/papers/icrc2013-0580.pdf (cit. on p. 94).

[123] M. Born and E. Wolf, *Principles of Optics: Electromagnetic Theory of Propagation, Interference and Diffraction of Light*, Elsevier Science, 2013, ISBN: 9781483103204,
URL: https://books.google.de/books?id=HY-GDAAAQBAJ (cit. on p. 96).

[124] M. Ehlert et al., *Proof-of-principle measurements with a liquid-scintillator detector using wavelength-shifting optical modules*, JINST **14** (2019) P03021,
arXiv: 1812.06460 [physics.ins-det] (cit. on p. 110).

[125] M. H. et al., "A Convolutional Neural Network based Cascade2Reconstruction for the IceCube Neutrino Observatory", submitted (cit. on p. 112).

[126] M. Bubeck, *Development of a Wavelength-shiftingOptical Module*, M.Sc. Thesis, 2020,
URL: https://butler.physik.uni-mainz.de/icecube/thesis/master_Maximilian_Bubeck.pdf (cit. on p. 112).

[127] *PMMA plastic cleaner*, [Online; accessed 26-September-2020],
URL: https://www.plexiglas-shop.com/en-de/products/antistatischer-kunststoff-reiniger-pfleger.html (cit. on p. 133).

[128] S. L. Glashow, *Resonant Scattering of Antineutrinos*, Physical Review **118** (1960) 316,
URL: https://doi.org/10.1103/physrev.118.316 (cit. on p. 137).

[129] I. C. Brock,
Users Guide to Writing a Thesis in a Physics/Astronomy Institute of the Universität Bonn,
URL: http://pi.physik.uni-bonn.de/pi_only/thesis.php (cit. on p. 149).

APPENDIX A

Supplementary Information

A.1 Measurement Recommendations

Since the devices available did not allow for a full characterization of the WOM, the following will provide a shortlist of recommendations on future measurements. The focus in these measurements is areas that need further investigation, especially in the context of systematic uncertainties.

1. Scan the PMT efficiency and gain as a function of position while noting the PMT orientation. Use these values to correct the following measurements with respect to tube and light source position during measurement and calibration measurement.

2. Measure WLS-paint coated PMMA tube(s) with the PMT:

   a) Find a small spot on the tube ($\approx$ 5 cm x 5 cm) and scan it with a thin optical fiber to see if small substructures are present.

   b) Mark a spot on the tube with a small piece of light-absorbing material and scan the entire tube surface with a reasonable resolution.

   c) Remove the tube, rotate it a few degrees and reattach it. Then repeat the scan. This will result in an estimate on the losses due to changes in the optical gel coupling. Repeat this a few times to get a good estimate. The light-absorbing spot will serve as a reference point to compare the scans and find any further anomalies.

   d) Repeat the same process again without optical gel e.g. no contact between tube and PMT, to estimate the influence of the coupling.

   e) Now attach the other end of the tube to the PMT and scan the tube again. You can use the light-absorbing spot again as a reference and see if previously seen structures stay intact or if there is a directional dependence, as indicated with measurements in this thesis. This should be repeated for several tubes to see different dependencies. Dependencies could be different manufacturing batches or orientation during coating.

   f) Coat a large tube on the inside and see if higher efficiencies can be produced. This might be the reason for the difference in efficiency in comparison to the small tubes since this is still undetermined.

A.2 Supplementary Figures and Descriptions

This section contains figures, images and other elements that would otherwise disrupt the reading flow of this thesis but are essential to the integrity of the argumentation or may help to underline certain points.

A.2.1 Model-Based Error Estimation for the Cut Based PMT-Data Evaluation Method

The error of the cut method[1] has been chosen empirically. To estimate the accuracy of this choice the real error, based on the model of the NGauss method, is evaluated in this section. To obtain realistic SPE distributions, representative measurements from the old (ADC [106]) and new (ADQ14 [110]) setup are chosen. To obtain modifiable distributions, the fit described for the NGauss method is applied on both distributions. The fitted functions, denoted "Base", for the old- and new setup shown in fig. A.1 and A.2 respectively. In each case, the fit parameters were modified to obtain functions for low and high SPE detection rates, as well as a lower gain. To increase/lower the SPE rates, the pedestal size (A_{pedestal}) is decreased/increased. To emulate a lower gain the distance between pedestal and SPE peak is reduced by reducing the value for the SPE peak position (μ_{SPE}). This approach supplies several SPE distributions, for the setups used in this thesis, that are representative for the most common measurements.

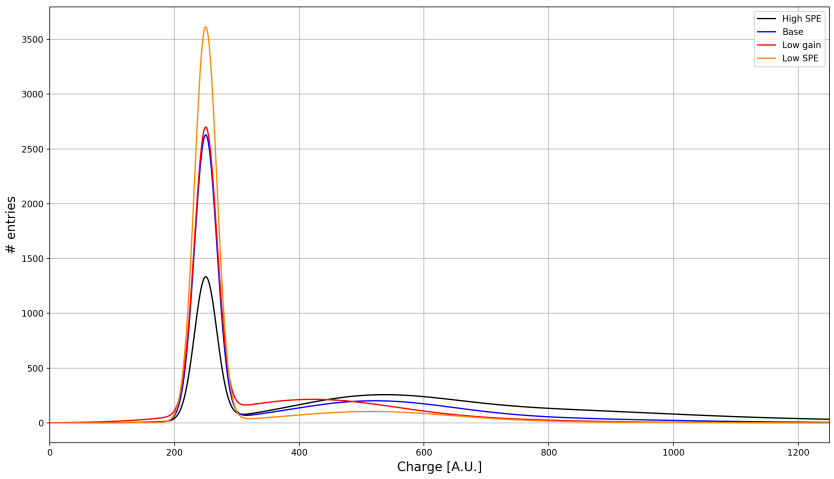

Figure A.1: Representation of different SPE distributions for the old setup, based on the NGauss method. "Base" is the resulting function of a multi Gauss fit, as described for the NGauss method, to an SPE distribution measured with the old setup [106] using the R1924A PMT from Hamamatsu [113] without pre-amplification. Low- and high SPE are the same distribution with modified parameters (larger or smaller pedestal A_{pedestal}) to represent lower or higher SPE detection rates. The low gain curve is also based on the same distribution with a reduced SPE peak to pedestal distance μ_{SPE} to imitate a lower gain.

Based on the produced distributions it is easy to calculate the real $\langle n \rangle$ with the methods described in chapter 5. It should be noted that neither noise nor under-amplified photons or other systematic effects are considered in this model. To determine the accuracy of the used error estimation with the cut method, the functions are transformed into binned representation and the cut method is applied and $\langle n \rangle$

[1] For the context and understanding of this section it is recommended to read chapter 5 first.

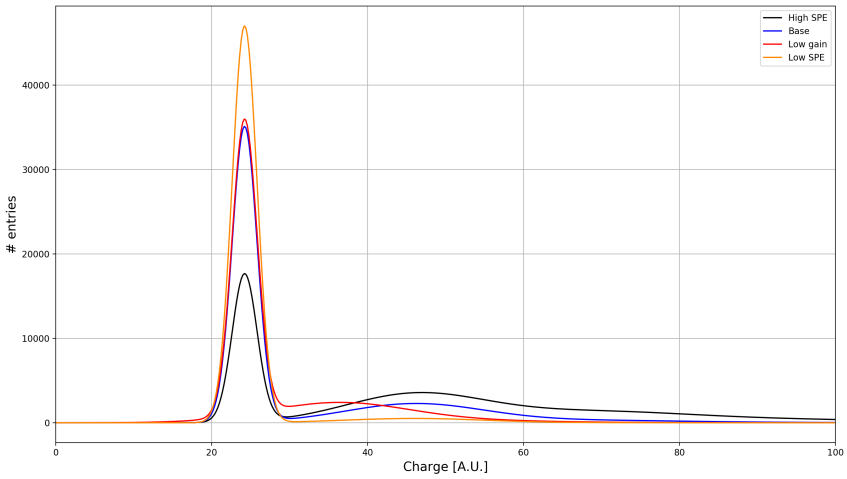

Figure A.2: Representation of different SPE distributions for the new setup, based on the NGauss method. "Base" is the resulting function of a multi Gauss fit, as described for the NGauss method, to an SPE distribution measured with the new setup [110] using the Hamamatsu R12199-02 without pre-amplification. Low- and high SPE are the same distribution with modified parameters (larger or smaller pedestal A_{pedestal}) to represent lower or higher SPE detection rates. The low gain curve is also based on the same distribution with a reduced SPE peak to pedestal distance μ_{SPE} to imitate a lower gain.

calculated for all possible cuts. The result is plotted in fig. A.3 for the old setup and fig. A.4 for the new setup. The solid vertical lines indicate the cut location for the lowest point between pedestal and SPE peak. The horizontal dashed lines indicate the theoretical real value for $\langle n \rangle$. As it can be seen in the plot the distance, used to estimate the error of 10 bins for the old setup, is in all cases too small. The Value of 3 bins used for the new setup matches in all cases. The effect on higher or lower SPE rate on the resulting error is small. For the old setup, it can be seen that low gains increase the difference between obtained value and real value, significantly.

In conclusion, the errors for the cut method with the old setup were likely underestimated since noise and under-amplified photons have to be taken into account as well. However, the fact that for the determination of efficiency the pair of $\langle n \rangle$ from calibration and sample measurement with the largest difference has been used to estimate the error, might compensate this to an unknown degree. Also since both measurements are affected in a similar way, given the gain stays constant, might compensate for this in the final efficiency. This has not been investigated any further. The error estimation for the new setup which in general recorded less noise and had a better separation between both peaks has been estimated correctly, while the clear systematics of this method becomes evident as well. The real value for a cut always appears closer to the pedestal than to the SPE peak, viewed from the lowest point between both.

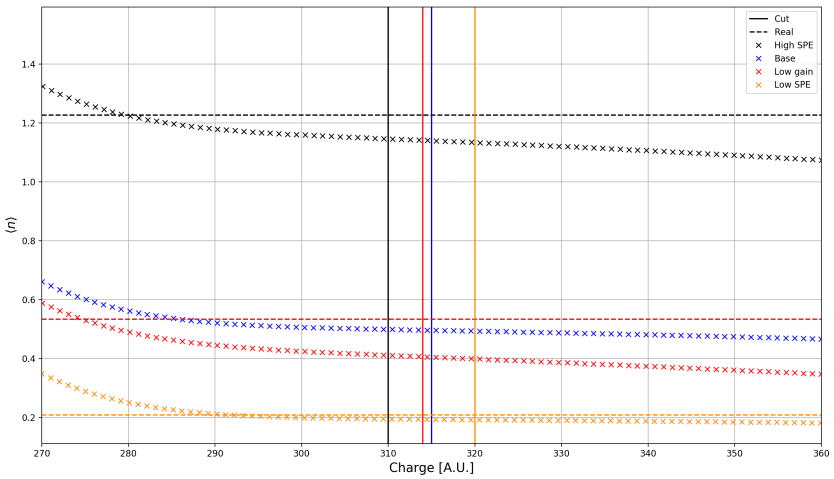

Figure A.3: The resulting $\langle n \rangle$ for different cut positions (crosses) based on the distributions shown in fig. A.1 for the old setup. The horizontal dashed lines indicate the correct value based on direct calculation. The solid vertical lines indicate the cut position based on the minimum value between pedestal and SPE peak. The horizontal lines for red and blue overlap due to the way their parameters were chosen.

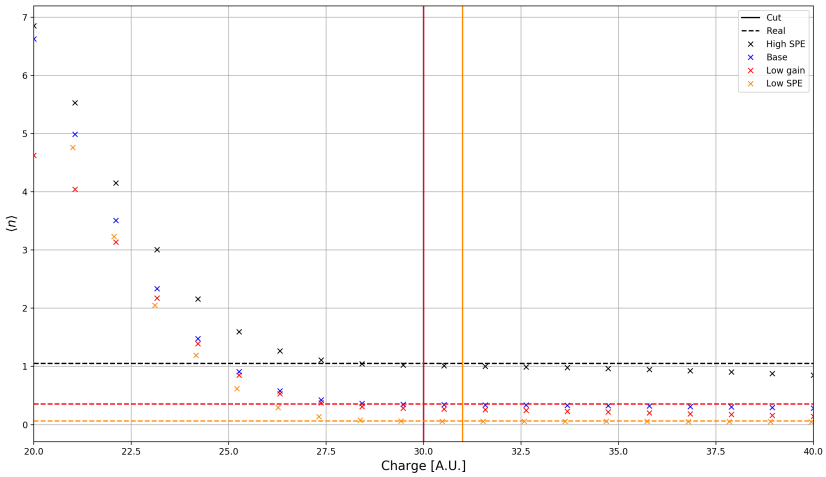

Figure A.4: The resulting $\langle n \rangle$ for different cut positions (crosses) based on the distributions shown in fig. A.2 for the new setup. The horizontal dashed lines indicate the correct value based on direct calculation. The solid vertical lines indicate the cut position based on the minimum value between pedestal and SPE peak. The vertical black, blue and yellow lines overlap. The horizontal lines for red and blue overlap due to the way their parameters were chosen.

A.2.2 Modelling

This section contains additional figures for chapter 6.

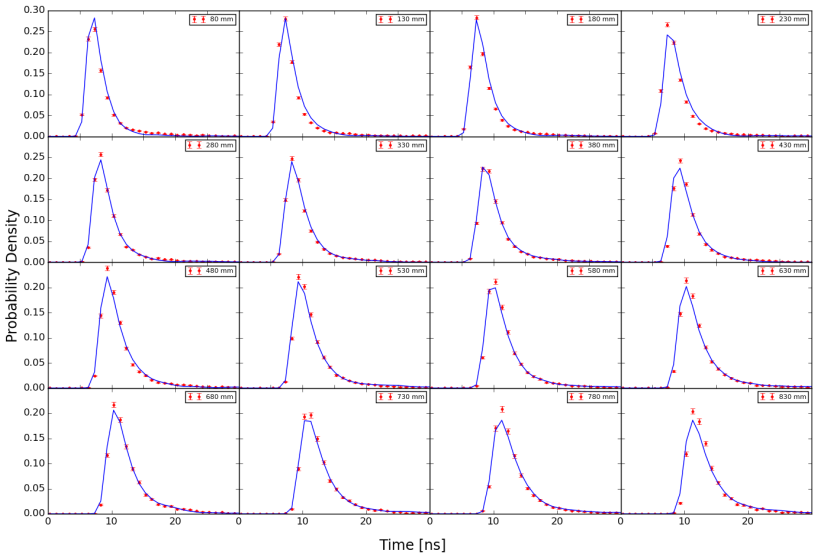

Figure A.5: Normalized timing distributions for PMT 1. Error bars indicate data, lines indicate the model fit.

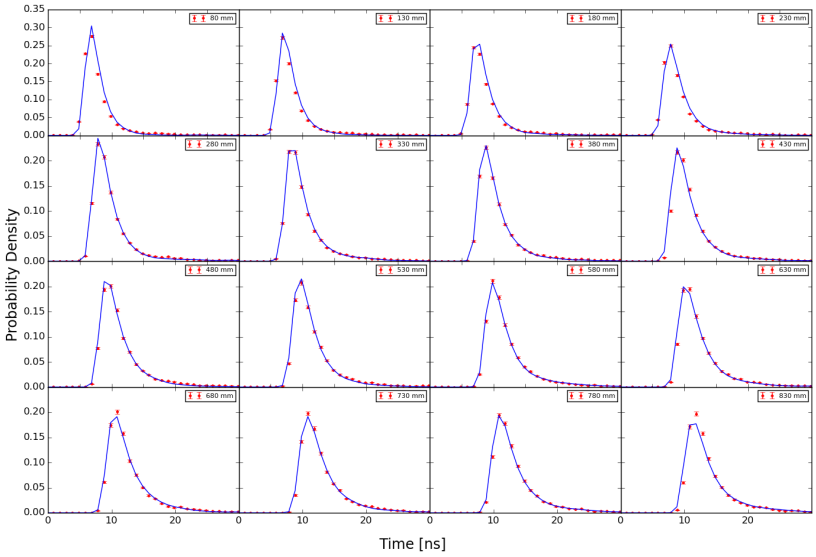

Figure A.6: Normalized timing distributions for PMT 2. Error bars indicate data, lines indicate the model fit.

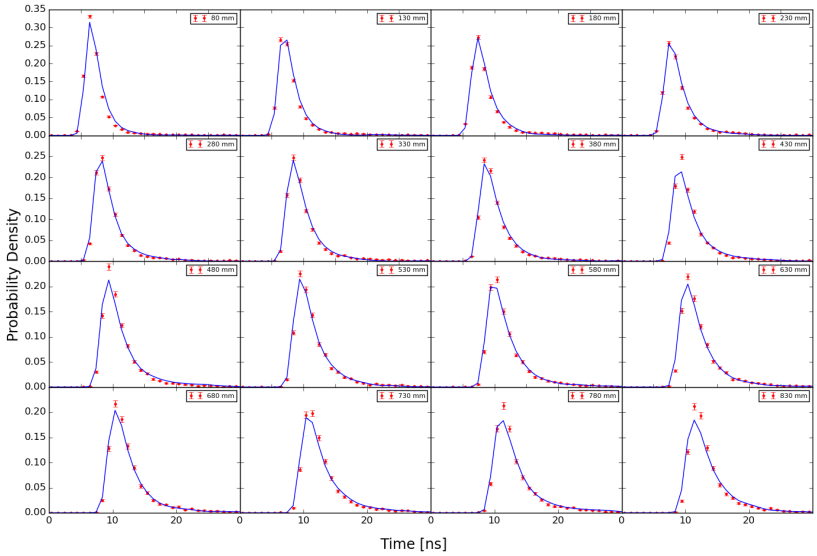

Figure A.7: Normalized timing distributions for PMT 4. Error bars indicate data, lines indicate the model fit.

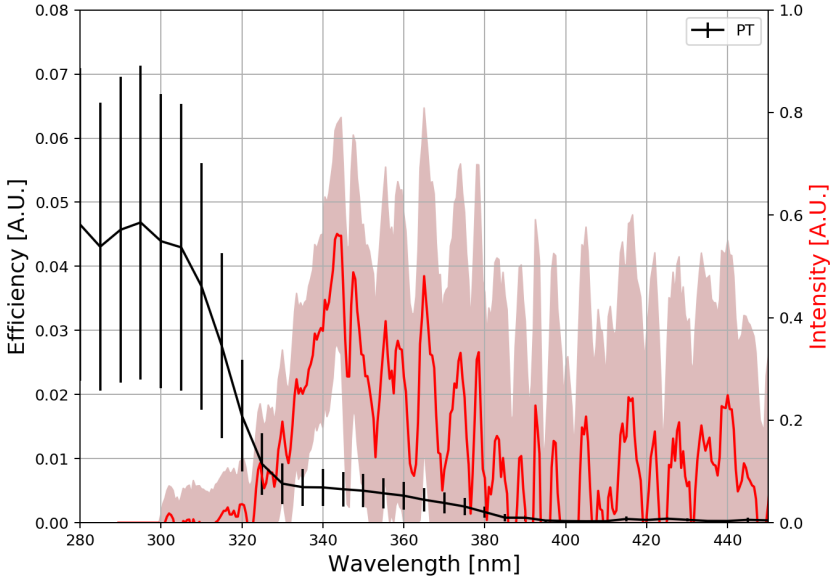

Figure A.8: p-Terphenyl efficiency and emission spectrum.

A.2.3 Light Distribution in the WOM

Measuring the light distribution at the end of a thin-walled tube is rather difficult with the equipment at hand. To obtain a general impression a position-dependent measurement was done with a mask and a PD on a PMMA rod. As displayed in fig. A.9 the intensity tends to rise with distance to the center but is rather homogeneous otherwise. The angular distribution of the light in the tube was measured as well. For that the setup is shown in fig. A.10 (left) was used. The resulting angular distribution was only obtained for angles perpendicular to the wall surface as shown in fig. A.10 (right). In the figure, the total internal reflection cutoff at $\approx 34^{\circ}$ can be seen as well as a double peak structure. For measurement of angles parallel to the wall, the angles are expected to be wider since the cut-off should have a smaller effect.

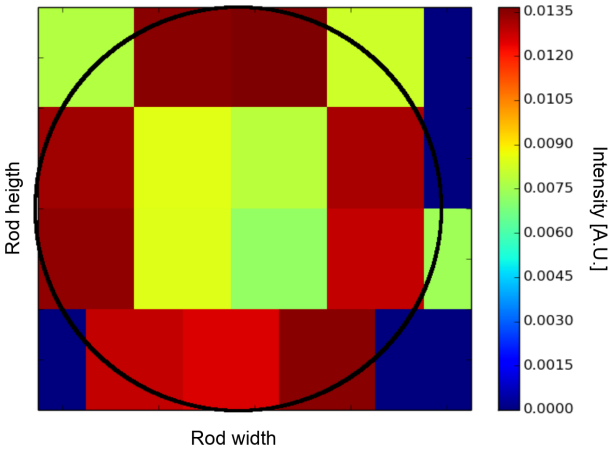

Figure A.9: Intensity distribution at one side of a 2 cm diameter WLS paint coated PMMA rod. The black line represents the edge of the rod. Pixel size is 0.47 mm times 0.50 mm. Source [115].

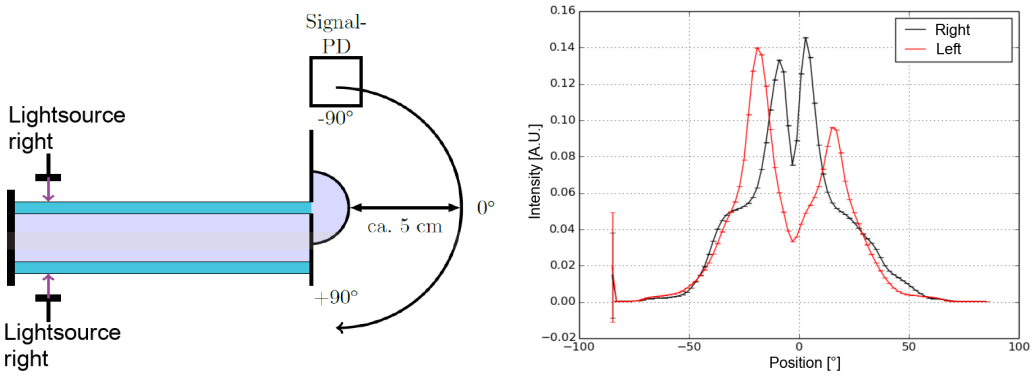

Figure A.10: (left) Sketch of the setup used to determine the angular distribution of the light in the tube. A cylinder-lens is used to get the whole distribution without cut-offs from total internal reflection. This figure was taken from [115], a more detailed description of the measurement can be found there as well. (right) Angular distribution of the light in the tube. Displayed is the relative intensity corrected by a reference PD with statistical errors. Source [115].

A.3 Details on the Modelling of the Photon-Detection Time

To roughly describe the histograms a log-normal distribution, as in eq. A.1 with the constant $T = 1$ ns, is fitted to them. An example is shown in fig. A.11. It can bee seen that the tail of the distribution is not well represented in the fitted function. However, as an approximation, this does suffice since detailed timing information is not required for the first tests.

$$L(x) = \frac{A \cdot T}{x} \cdot \frac{1}{\sigma\sqrt{2\pi}} \exp\left(-\frac{(\ln\frac{x}{T} - \mu)^2}{2\sigma^2}\right) \tag{A.1}$$

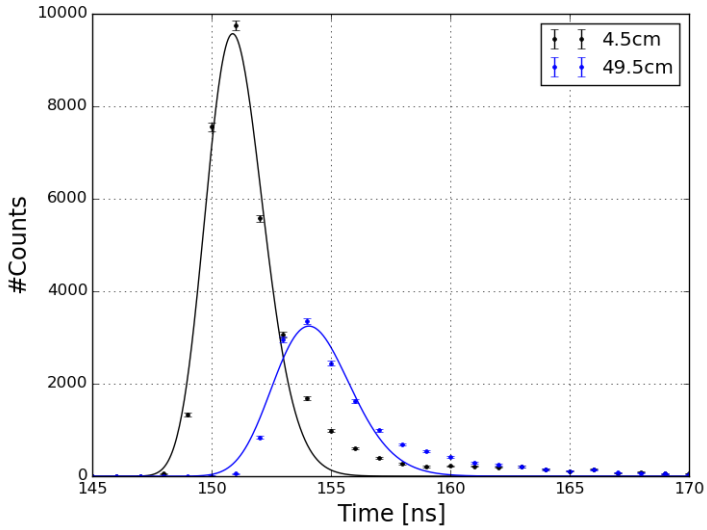

Figure A.11: Photon arrival time distribution for two different positions along the tube. Points are the real data and lines are the fitted log-normal distributions.

To derive an empirical model, the histograms for the different PMTs are merged and fitted for the parameters A, σ and μ. The resulting fit parameters are plotted as a function of position as shown in fig. A.12. In these plots fits that did not converge and large outliers have been removed. To reduce the number of parameters needed to replicate the distribution, the resulting distributions have again been approximated by appropriate functions. Functions have been chosen that resemble the distributions empirically so that a fit could be performed. For the scaling factor A, an exponential function as in eq. A.2 is used. For the width σ a linear function as in eq. A.3 and for the offset μ, a scaled square root as in eq. A.4 is used. The now obtained function parameters from tab. A.1 are used in the simulation to generate photon arrival times with a log-normal distribution based on the arrival position.

$$A(x) = A_0 \cdot \exp^{\frac{-x}{l}+b} \tag{A.2}$$
$$\sigma(x) = f + g \cdot x \tag{A.3}$$
$$\mu(x) = c + d \cdot \sqrt{x+e} \tag{A.4}$$

To show that the now continuously available timing distributions approximate the measured distributions, a comparison is shown in fig. 7.9. It can still be seen that the tail is not well matched as to

$A_0 = 27.41 \cdot 10^4$	$l = 47.52$	$b = 1.32$
$c = 2.31$	$d = 0.0636$	$e = 14.76$
$f = 0.0941$	$g = 1.5035 \cdot 10^{-4}$	

Table A.1: Results of the fits from eq. A.2-A.4 as shown in fig. A.12.

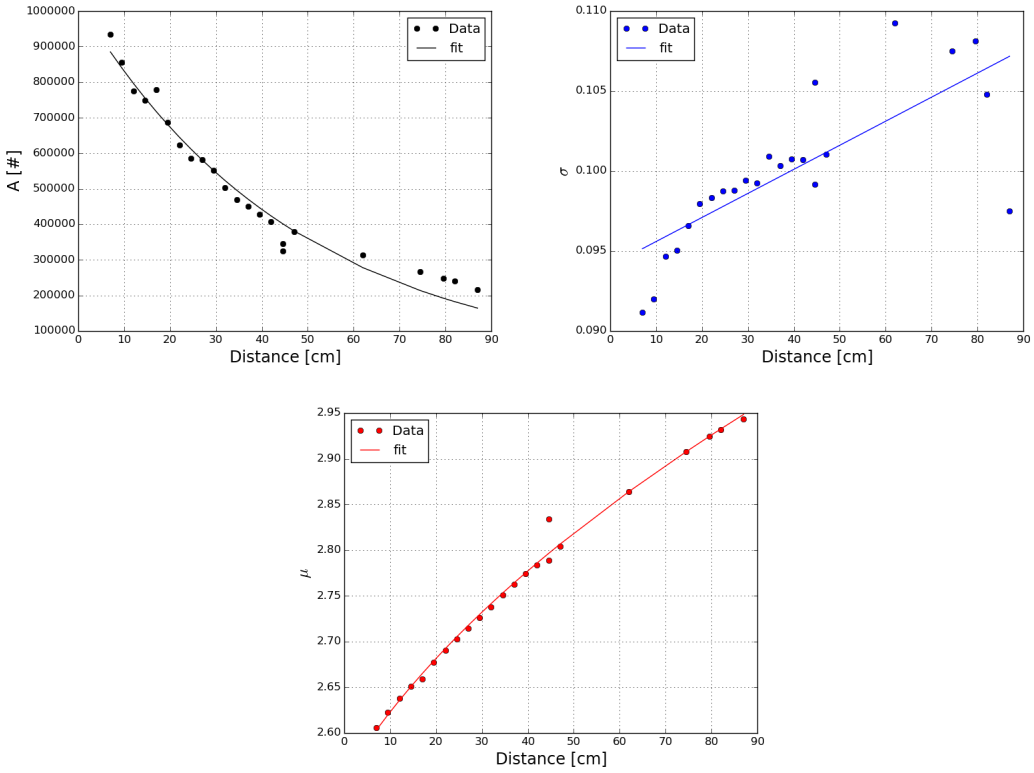

Figure A.12: Fit to previous fit parameters from log-normal distributions. (left) A the scaling factor. (right) σ the width. (bottom) μ the offset.

be expected, however, the rest of the distribution is well described considering a hight offset from the missing tail in the normalized distributions.

A.4 Documentation

This section contains useful information for someone willing to pick up and continue this work.

A.4.1 How to make WLS Paint

The paint composition was determined by trial and error. Therefore the paint recipe is based on the ingredients, not the final composition. The approximate composition has been determined in [114].[2] The ingredients are 25.0 g Paraloid B72, 0.15 g Bis-MSB and 0.3 g PT per 100 ml Toluene, scalable to the required quantities.

- Step 1: Fill the toluene in an appropriately sized beaker, add a magnet mixing fish and place on a hotplate stirrer.
- Step 2: Set the temperature to $\approx 150\,^{\circ}\mathrm{C}$ and the stirrer to $\approx 300\,\mathrm{rpm}$. The temperature should not be reached since the boiling point of toluene is $110.6\,^{\circ}\mathrm{C}$. In case the liquid does start to boil, immediately reduce the temperature.
- Step 3: Start adding the Paraloid in $2-3$ batches. To avoid clogging wait each time until the previous batch is dissolved. The refractive index of the solution will approach the one of the plastic, therefore a spade or similar is needed to determine whether or not the previous batch is dissolved. Increase the rotation speed as the viscosity increases. A small vortex should always be on the surface of the mixture.
- Step 4: Add the PT and Bis-MSB to the mixture.
- Step 5: Switch off the heating and leave the solution to cool. Continue stirring for about 5 minutes.

Appropriated safety measures need to be observed. When using a scale under the fume hood be aware of the Bernoulli effect. According to [114] $\approx 5-9\,\%$ of the toluene evaporates during this process. Generally, this can be used to produce paint with higher or lower viscosity and thus optical density. Decreasing the solvent content too far my cause crystallisation of the WLS within hours or days. Especially PT is prone to crystallisation.

A.4.2 Dip-Coater Manual

The dip-coater is currently based at DESY (Zeuthen) and belongs to the Humboldt University of Berlin. The Hardware used is an Arduino Uno with a Motor Shield, connected to a stepper motor. The stepper motor drives a threaded rod that allows a carriage to move along the rod. The carriage can travel within a range of a little more than a meter. For exact specifications please refer to the actual device. To operate the device firmware is needed. The firmware can be found at `https://github.com/hebecked/DipCoater_Firmware`. The Version "Curent_Microstepping" is the one described in the following. After uploading the firmware,[3] the primary mode of operation is via serial interface[4] using the USB connector. The following instructions are possible:

[2] Do not use the paint production method described in this source, it contains faulty instructions.
[3] Refer to the Arduino instructions manual.
[4] 9600 bps.

- Send any value (e.g. "h"), except the ones defined below, to receive a short manual.
- Send "S#####" to initialise the number of steps to #####. This will be the number of steps the carriage performs for any command that involves movement. The recommended value is 30000 to cover just about 3/4 of the height of the devices.
- Send "D#" to initialise the delay between micro-steps to # in milliseconds. Useful values are between 2 and 5.
- Send "t" to return the current settings.
- Send "u" to move the carriage up. The button on the device labelled "Up" performs the same command. Before initialisation of a step number, the button operates as a dead man switch.
- Send "d" to move the carriage down. The button on the device labelled "Down" performs the same command. Before initialisation of a step number, the button operates as a dead man switch.
- Send "r" to move the carriage slowly up with a well-defined speed using micro-stepping. The button on the device labelled "Run" performs the same command.
- Send "s" to overwrite and previous movement commands and halt the device. The button on the device labelled "Stop" performs the same command.

This version of the firmware supports speed control, micro-stepping and limits the range of movements. Further improvements are possible. The current version calculates the values for the micro-stepping on the fly. Any future user might want to create a look-up table for this to increase performance and the range of coating speeds. The type of "steps" should be changed from unsigned integer to unsigned long to avoid overflows. The delay should call delayMicroseconds(us) not delay(ms) to allow for more accurate speed control. Reasonable safety precautions should be taken. Do not leave the step number initialized at values > 1 when the device is unattended. Make sure the end switches are installed properly and are functional. Overall it is recommended to upgrade to a newer coater since the current one is built from spare parts including a damaged threaded rod. A device to spray the paint onto the tubes might be an option as well.

A.4.3 How to Coat and Clean a Sample

Before a paint coating is applied to any substrate it is to be cleaned. For glass substrates, a range of different cleaning methods and materials was investigated in [86]. For PMMA a combination of different cleaners was recommended. Further testing has shown that only the use of commercially available anti-static plastic cleaner [127] is sufficient. For cleaning the cleaner is applied to a lint-free paper cloth is then used to gently wipe the surface of the substrate. After a short drying period, the substrate can be coated.

To coat the substrate it needs to be attached to the dip-coater. Depending on the shape of the substrate a holding structure needs to be fabricated. For tubes, a vice-like device as shown in fig. 5.16 can be used. An appropriate paint container needs to be used. When using a paint container and measuring the amount of paint needed, always account for displacement. The dip-coater needs to be used to immerse the sample in the paint. After immersion, it can be helpful to let the substrate sit in the paint for some time before drawing it out. For most samples in this thesis, a waiting time of 1 minute was used. However, in some cases, this caused tension cracks in the PMMA. A shorter time reduces the

probability for cracks but increases the probability for uneven surface structures in the paint. The exact mechanism behind the latter effect is unknown but suspected to be due to residue on the substrate surface. Paint thickness increases with coating speed. While the paint surface is usually dry within $1-2$ hours, for the fastest coating speed the paint only becomes resistant to touch after about 24 hours.

A.4.4 How to Glue PMMA Suitable for Light Transmission

In order to attach the adiabatic light guide to the WLS-tube, three different type of glue have been evaluated: A solvent-based glue ACRIFIX 1R 0192 produced by Evonik Performance Materials GmbH, a UV-curing glue BEST-PL 5373 from BEST-Klebstoffe GmbH & Co. KG and dichloromethane a solvent with good creeping properties. When a thin layer is applied, ACRIFIX hardens very quickly. Therefore it is very difficult to distribute it evenly and produce good optical contact between the surfaces. The UV-curing glue showed the best optical connection with little to no gaps between the surfaces. Though the tubes usually showed micro-fractures around the connection a day after curing. Dichloromethane produced good connections but required extremely even surfaces that were not always available. Spills could corrupt the surface of the tubes and larger cracks appeared most of the time within hours. None of the glues produced the desired results, yet the best results were obtained by the UV-curing glue. Optical measurements were also performed at Mainz University. Yet the results were unusable due to technical difficulties with the setup.

Remark: To determine the fraction of losses caused by the glue connections, glue test measurements were performed in the laboratory of Prof. Dr. S. Böser in Mainz. This laboratory provides PMTs large enough to measure both tube ends without an adiabatic light-guide. After taking several measurements with the setup there, it was discovered that there is a significant noise contribution from parts of the setup that could not be resolved in time to finish the measurements. The efforts were followed up by the local collaborators independent from this thesis.

A.4.5 How to use the Measurement Setup at Adlershof

During the work on this thesis, a multi-purpose measurement setup was built up at the Humboldt University of Berlin. The setup contains among others the following devices:

- 2x Lock-in amplifier. Stanford Research Systems SR830.
- 1x Portal scanner with x-,y- and z-axis.
- 2x Rotational stage. With up to 3 possible if needed.
- 1x Optical chopper.
- 1x CornerStone260 monochromator.
- 1x High-pressure Xenon lamp.
- 1x Picoampere meter.

In order to facilitate fast and easy measurements for future users a multi-purpose DAQ and control software was written. The source code can be found at `https://github.com/hebecked/PyDAQ`. The code contains modules to control each of the devices via CLI and API. Furthermore a comprehensive module was written. Based on an instruction file, that is executed in steps, all devices can be controlled

and output can be written to a .csv file. When the program is started the instruction file is read and all necessary devices are initialised. The process is then forged into two sub-processes. One process executes the instruction file, step by step, with a strong focus on reproducible execution time,[5] while the other process handles asynchronous file writes from the data acquisition. It is also possible to allow the second process to dynamically plot the acquired data on the screen. The ordinary user now only needs to create an instruction file. In order to write the instruction file, the module "mkinst.py" can be used. "mkinst.py" supplies an API, so instruction files can be created easily. After initialisation, the function "add_instruction()" allows adding a single instruction set to a given instruction file. An instruction set allows a single change for each connected device. If a device does not get a specific instruction the default value is used. In all cases, the default value does not change the state of the device. In case the setup of the computer changes, the config file needs to be modified to account for the ports of the different devices. In many cases, the ports can be detected automatically, while some devices can not be detected reliably yet. Therefore it is recommended to write the config file by hand. For the exact execution please consult the codebase. It should be sufficiently easy to read.

Some improvements can be recommended for the future. The instruction files currently need to contain the default value for each device if it is not supposed to operate since the instruction set structure is fixed. It is recommended to create a second version of the instruction file format that resembles the pickle file format. This way default values do not need to be written to file and the readability for humans improves. The versioning of instruction files is already foreseen in the codebase and should be easy to implement. This will also facilitate the generalisation of the code to arbitrary devices and instructions. For even easier usage it might be of interest to write GUIs for the DAQ and different device controls. The portal scanner currently just moves to the position it is given. Mistakes in the creation of instruction sets might move the device to or through undesired locations that could break other setups. Therefore it might be desirable to implement safety zones that can not be touched independent of the given instructions. The would either cause a halt or make the device move around it.

A.4.6 How to use the Setup at Zeuthen

At DESY (Zeuthen) a secondary smaller setup was build up with a monochromator and a HF2LI lock-in amplifier from Zurich Instruments. For data taking a LabVIEW DAQ was written that can be found at `https://github.com/hebecked/LabVIEW_DAQ`. A screenshot can be seen in fig. A.13. Modules to control the devices individually can be found in the source code as well. Most devices are also compatible with the Python-based DAQ described above. Since it is more modular, the Python-based DAQ is recommended to be used going forward.

[5] As good as possible with a non-real-time OS. It is therefore recommended to not run any other computationally expensive tasks on the machine.

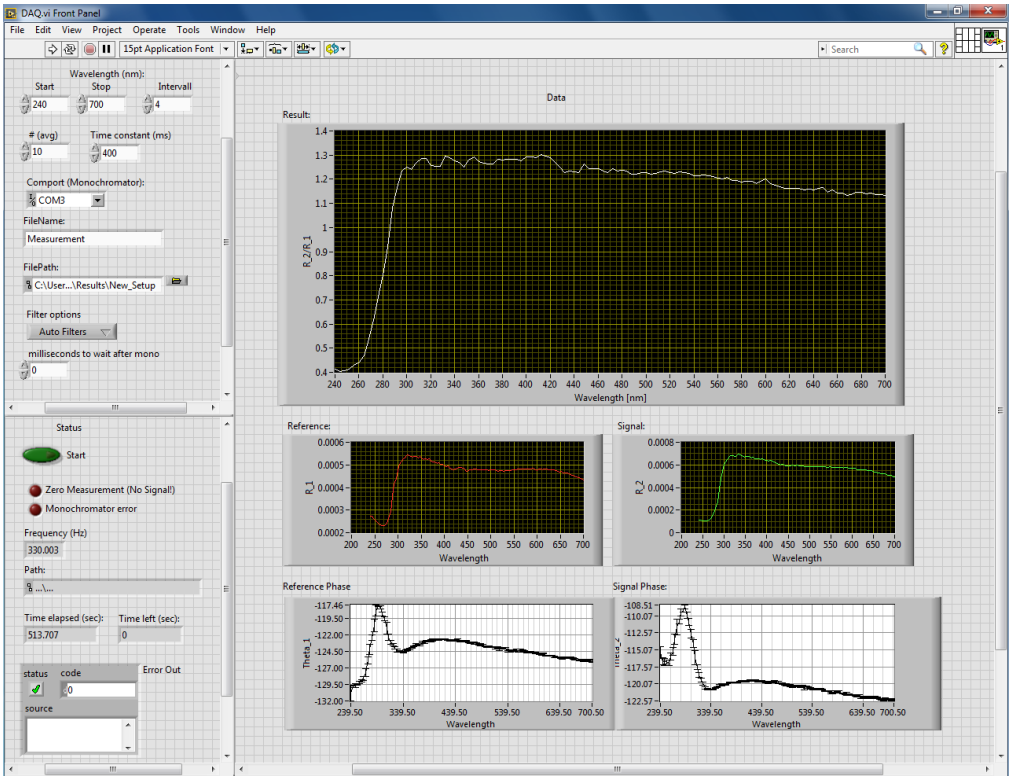

Figure A.13: Screenshot of the LabVIEW DAQ system.

A.5 Acronyms

- ADC - Analog-to-digital converter, a device or chip that converts analog signals to a digital representation.
- API - Application programming interface. An interface that allows computer programs to be included/controlled by other programs.
- ARM - Advanced RISC Machines are a type of CPU/processor based on the RISC (reduced instruction set computer) architecture.
- Bis-MSB - 1,4-Bis(2-methylstyryl)benzol a wavelength shifter that absorbs UV-light and re-emits it at $\approx 420\,\mathrm{nm}$.
- BSM - Physics beyond the Standard Model.
- CC - Charged current (interaction) or core-collapse (SN) depending on the context.
- CLI - Command-line interface. An interface that allows a program to be controlled from the command line.
- CMB - Cosmic microwave background.
- CNB - Cosmic neutrino background. Like the CMB but earlier. Based on the freeze-out of neutrinos instead of photons.
- CPU - Central processing unit, the logic circuitry within a computer that executes binary instructions.
- D-Egg - Dual Optical Sensors in an Ellipsoid Glass for Gen2. Another optical module designed for IceCube-Gen2.
- DAQ - Data acquisition or data acquisition system. Generally the process of data acquisition or a device that acquires data electronically.
- DC - Direct current. One directional electric current.
- DOM - Digital optical module. The detection units used in IceCube.
- EM - Electro-magnetic
- FOM - Fiber optical module. Another optical module designed for IceCube-Gen2.
- FPGA - Field Programmable Gate Arrays. Chips that can be electronically configured after production and deployment.
- FWHM - Full width at half maximum.
- GPU - Graphics processing unit. Like a CPU but dedicated and optimized for the processing of tasks needed to calculate graphical representations.
- GR - Glasshow resonance [128].
- GUI - Graphical user interface.

- GZK - Greisen–Zatsepin–Kuzmin limit is the theoretical upper limit for the energy of cosmic ray protons due to interaction with the CMB.
- HV - High Voltage.
- LHC - Large Hadron Collider.
- LOM - Long optical module. Yet another optical module designed for IceCube-Gen2. Also known as a Brussel sprouts optical module. The actual name of this has been changed several times in the past.
- IR - Infrared.
- mDOM - Multi-PMT digital optical module. Yet another optical module designed for IceCube-Gen2.
- NC - Neutral current (interaction).
- ND - Neutral density or neutral density filter. An optical attenuator with consistent absorption or reflection over a broad wavelength range.
- OS - Operating system. The core system/program that manages all other programs and their execution on a computer.
- PD - Photodiode.
- pDOM - PINGU digital optical module. Another optical module designed for IceCube-Gen2.
- PMT - Photomultiplier tube. A very sensitive light detection device.
- PT - p-Terphenyl. A wavelength-shifter that absorbs deep UV-light and re-emits it at $\approx 275\,\text{nm}$.
- PTFE - Polytetrafluoroethylene. Also known as Teflon, a plastic with a very low friction coefficient.
- PVC - Polyvinyl chloride.
- QE - Quantum efficiency.
- RPM - Rotations per minute.
- SHiP - Search for hidden particles. A new general-purpose experiment to be installed at the LHC.
- SN - Supernova.
- TIR - Total internal reflection.
- UV - Ultraviolet. A range in the EM-spectrum with higher energies than visible light.
- WLS - Wavelength-shifter.
- WOM - Wavelength-shifting optical module. The optical module discussed and developed in this thesis.

List of Figures

[6] Double precision.

List of Tables

Acknowledgements

It was a long way finishing this thesis. To my surprise the difficulties were less of a scientific nature but rather a collection of challenges surrounding it. Now this journey is over, and I am looking forward to new challenges and adventures. I am grateful for the experiences and connections I made along the way and will cherish them. There are many people who shaped my way in the last few years. While I cannot thank everybody there are a few people that stand out.

First of all, I would like to thank my colleagues, my office and lab mates for the constructive but also joyful and entertaining time we had together. Special thank goes to everyone who gave me smaller and larger but always valuable feedback on my thesis. Namely, they are Daniel Küsters, Beniamin Bastian-Querner, Jannes Brostean Kaiser, Jakob van Santen, Tuur Mertens, Grace Shih, Samridha Kunwar, Juliana Stachurska, Federica Bradascio, Isabella Rahel Boventer, Merlin Hebecker and Summer Blot. There are several more people among my family and friends who supported me emotionally over the last years, who I would also like to thank. Furthermore, I would like to thank Prof. Dr. Marek Kowalski, the Humboldt University of Berlin and DESY Zeuthen for making my thesis possible.

My Gratitude also goes towards Prof. Dr. Sebastion Böser and PD Dr. Ira Jung-Richardt for being the second and third referee. I am also very grateful for Prof. Dr. Thorsten Kamps and Prof. Dr. Heiko Lacker who agreed to be the fourth and fifth members in my committee. Additional thanks goes to Prof. Dr. Anna Friederike Nelles and Prof. Dr. Michael Wurm for their willingness to be my third referee even though they were ultimately not accepted as such.

Then there are those hidden people who I would also like to thank. One of these People is Ian C. Brock who developed the thesis template/guide [129] that this thesis is based on, as well as the people of the mechanical and electrical workshops at the institute of physics at the Humboldt University and DESY, who made many of the technical aspects during the measurements possible.

In the end I am just insanely curious what the future will bring to me and all of you. Exciting times are ahead and I hope our paths will cross again.

Selbständigkeitserklärung

Ich erkläre, dass ich die Dissertation selbständig und nur unter Verwendung der von mir gemäß §7 Abs. 3 der Promotionsordnung der Mathematisch-Naturwissenschaftlichen Fakultät, veröffentlicht im Amtlichen Mitteilungsblatt der Humboldt-Universität zu Berlin Nr. 42/2018 am 11.07.2018 angegebenen Hilfsmittel angefertigt habe.

Dustin Hebecker
Dezember 2020